Universität Ulm
Institut für Elektrochemie

Properties and Structure of the Electrified Gold/Ionic Liquid Interface

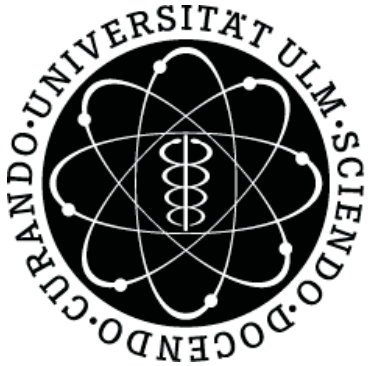

Dissertation
zur Erlangung des Doktorgrades Dr. rer. nat.
der Fakultät für Naturwissenschaften
der Universität Ulm

vorgelegt von
Markus Gnahm
aus Ulm

2012

Universität Ulm
Institut für Elektrochemie

Properties and Structure of the Electrified Gold/Ionic Liquid Interface

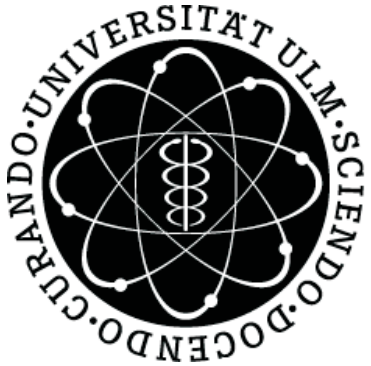

Dissertation
zur Erlangung des Doktorgrades Dr. rer. nat.
der Fakultät für Naturwissenschaften
der Universität Ulm

vorgelegt von
Markus Gnahm
aus Ulm

2012

Der experimentelle Teil dieser Arbeit wurde in der Zeit von Januar 2008 bis Mai 2011 am Institut für Elektrochemie der Universität Ulm angefertigt.

Amtierender Dekan: Prof. Dr. A. Groß

Erstgutachter: Prof. Dr. T. Jacob
Zweitgutachter: Prof. Dr. Werner Tillmetz

Tag der Promotion: 05.11.2012

Table of Contents

1 Introduction **VII**

I Fundamentals 1

2 The Electrified Interface **1**
2.1 The Electric Double Layer 1
2.2 Potential of Zero Charge 3
2.3 Surface Reconstruction 4

3 Ionic Liquids in Electrochemistry **6**
3.1 Synthesis 7
3.2 Physicochemical Properties 8
3.3 Electrodeposition of Metals 12

4 Methods **14**
4.1 Cyclic Voltammetry 14
4.2 Electrochemical Impedance Spectroscopy 15
4.3 Scanning Tunneling Microscopy 21

II Experimental 27

5 Electrochemical Cells **27**
5.1 STM Cell 27
5.2 Impedance Cell 28

6 *In-situ* STM Experiments **30**
6.1 Experimental Setup 30
6.2 Tip Preparation 30

7 Electrode and Electrolyte Preparation **32**
7.1 Annealing of Single Crystals . . . 32
7.2 Electropolishing . . . 32
7.3 Ionic Liquid Purification . . . 33
7.4 Reference Electrodes in Ionic Liquids . . . 33

8 Materials and Chemicals **34**

III Results **39**

9 Au(111) in $BMIPF_6$ **39**
9.1 Discussion . . . 44

10 Purification of Ionic Liquids **49**

11 Au(100) in $BMIPF_6$ **54**
11.1 Cyclic Voltammetry . . . 54
11.2 Determination of the pztc . . . 55
11.3 Impedance Studies . . . 57
11.4 Synopsis of the CV, pztc and Impedance Measurements . . . 59
11.5 *In-situ* STM Studies . . . 60

12 The Gold Surface in $BMITf_2N$ **65**
12.1 Cyclic Voltammetry and Impedance Spectroscopy . . . 65
12.2 *In-situ* STM Studies . . . 67

13 The Gold Surface in $Bu_2Et_2Me_2GuanTf_2N$ **70**
13.1 Cyclic Voltammetry and Impedance Spectroscopy . . . 71
13.2 *In-situ* STM Studies . . . 73

14 Metal Deposition from Ionic Liquids **78**
14.1 Deposition of Pd onto Au(111) from $BMIPF_6$ . . . 78
14.2 Deposition of Pd onto Au(100) from $BMIPF_6$ . . . 82

15 Summary **89**

Bibliography **93**

List of Abbreviations **105**

List of Symbols **107**

Publication List **109**

Acknowledgement **111**

Curriculum Vitae **113**

in memoriam

Dieter Kolb

1 Introduction

Ionic liquids (ILs) are salts which are molten at room temperature and composed of organic cations and organic or inorganic anions [1]. The most prominent interest in ionic liquids as solvents in electrochemistry comes from their wide electrochemical windows (potential range of ideal electrode polarizability), which provide possibilities for investigating electrode processes which would be impossible in aqueous electrolytes (hydrogen, oxygen evolution) [2–4].

Paul Walden discovered the liquid salt ethylammonium nitrate in 1914 [5]; the first experiments with ionic liquids based on $AlCl_3$ were made during the 1950s: ILs of two components such as $AlCl_3$ and alkylpyridinium or alkylimidazolium were used as electrolytes for electrodeposition of metals [6]. These „first generation“ ILs have the big disadvantage of being hygroscopic, liberating HCl upon exposure to moisture. Thus these liquids were considered to be difficult to work with; hence being of little practical importance. On the other hand, these ILs possess remarkable broad electrochemical windows, allowing the deposition of less noble metals, e.g. aluminium. Therefore, great efforts were devoted during the 1980s to search for ionic liquids with increased electrochemical windows and enhanced stability against air and water. In the early 1990s John Wilkes' group could synthesize air- and water-stable ionic liquids containing the $[BF_4]^-$ and the $[PF_6]^-$ anions [7]. The electrochemical window of these liquids turned out to be as wide as 4 V.

Despite their great potential for new electrochemical processes, the electrochemical interface between a metal electrode and an IL, that is, the double layer structure, is far from being well understood. This might be partly attributed to the fact that electrochemical studies have rarely been done on truly clean and structurally well-defined surfaces; this – together with the often questionable purity of ILs – accounts for the widely differing quality of the reports and conclusions. As for double layer studies in aqueous solutions, where single crystal surfaces with well-defined structures as well as ultrapure water and chemicals laid the basis for a detailed understanding of the interfacial region, well prepared surfaces and clean ILs are still key issues in this emerging field [8].

This thesis attempts to explore key points of the double layer structure on well-defined single crystalline gold electrode surfaces in contact with those ionic liquids which are

available in high purity. Emphasis is laid on high-resolution and molecular-level characterization of the electric double layer. The main tool for determining double layer properties is the capacitance measurement through impedance spectroscopy. *In-situ* STM measurements were performed in order to characterize structural changes within the interfacial region.

An overview of fundamental aspects of this work is given in part I (chapters 2-4), followed by the discussion of experimental details in part II (chapters 5-8).

- Essential studies of the electrochemical interface between Au(111) and 1-butyl-3-methyl-imidazolium hexafluoro-phosphate ($BMIPF_6$) are discussed in chapter 9. Interfacial parameters such as double layer capacitance and the *potential of zero total charge* (*pztc*), could be determined. *In-situ* STM measurements reveal marked structural differences positive and negative of the pztc.

- Since ILs have practically no vapour pressure at room temperature, purification of the liquids after synthesis is still a serious issue. In chapter 10 a purification method for commercially available $BMIPF_6$ is presented.

- The electrochemical interface between a Au(100) single electrode surface and $BMIPF_6$ is discussed in chapter 11. Impedance spectra could be well fitted using an appropriate equivalent circuit. In the negative potential region an ordered adlayer of $[BMI]^+$ cations has been observed by STM.

- Influence of the anion on double layer properties is discussed in chapter 12. The interfacial properties of $BMITf_2N$ have been compared with those of $BMIPF_6$ on Au(100) and Au(111) surfaces.

- Changing the aromatic imidazolium cation against a non-aromatic guanidinium cation has consequences on interfacial properties, e.g. the double layer capacitance (chapter 13). The interaction of a hexaalkyl-substituted guanidinium ionic liquid (N,N-dibutyl-N',N'-diethyl-N",N"-dimethylguanidinium-bis(trifluoromethylsulfonyl) imide) with single crystalline gold surfaces (here Au(100) and Au(111)) has been investigated.

- Chapter 14 finally reviews initial stages of metal deposition from ionic liquids. The deposition of palladium onto Au(111) and Au(100) single crystal surfaces from $BMIPF_6$ was investigated. Morphological differences of the deposited layers could be observed compared to deposition in aqueous electrolytes.

Part I

Fundamentals

2 The Electrified Interface

2.1 The Electric Double Layer

The electrode is an electronic conductor – typically a metal – in contact with an ionic conductor — commonly an aqueous electrolyte solution. In the case of the present studies the electrolyte is an ionic liquid. At the junction a specific interfacial region is formed, the so-called double layer. The interfacial region differs in properties such as chemical and electric potentials from the adjacent phases. There exist many theories on the properties of the double layers, but none of them is adequate for all situations, since the double layer structure and properties depend on the chemical nature and physical properties of both the electrode and the electrolyte, not to mention general physico-chemical conditions such as temperature. In general, the interfacial region's structure is characterized by the interfacial excesses of the chemical species therein. Measurement of excesses is difficult, however, measurement of the sum of the excesses of ionic species is possible through the measurement of the electronic charge of the metal, q^{M}. Unfortunately, charge cannot be determined directly, only its changes as currents $i = dq^{\mathrm{M}}/dt$ or as differential capacitances $C = dq^{\mathrm{M}}/dE$, that is as time (t) or potential (E) derivatives. This is why the differential capacitance plays a central role in double layer studies.

The first model to characterize the electrical properties of the double layer was proposed by Helmholtz as a simple parallel-plate condenser [9, 10]. One plate is the metal surface carrying an excess charge Q, which attracts an equivalent amount of counter ions to the interface. The double layer capacitance is defined as:

$$C_{\mathrm{dl}} = \frac{dQ}{dE} \tag{2.1}$$

Helmholtz's model became the core of all double layer models. For aqueous systems, it was proven appropriate to consider the electrolyte side comprising inner and outer layers: The inner layer contains adsorbed ions and solvent species being in direct contact with the electrode; these are bound to the surface mostly by chemical forces. In contrast, the charges of the outer layer – typically solvated ions – are not in direct contact with the electrode and are bound to the surface with elelectrostatic forces only. Hence a certain

amount of counter-charge is necessary for charge compensation. As a result the specific adsorption of ions causes a different potential profile compared to a purely electrostatic interaction between solvated ions and the metal surface (Fig. 2.1a).

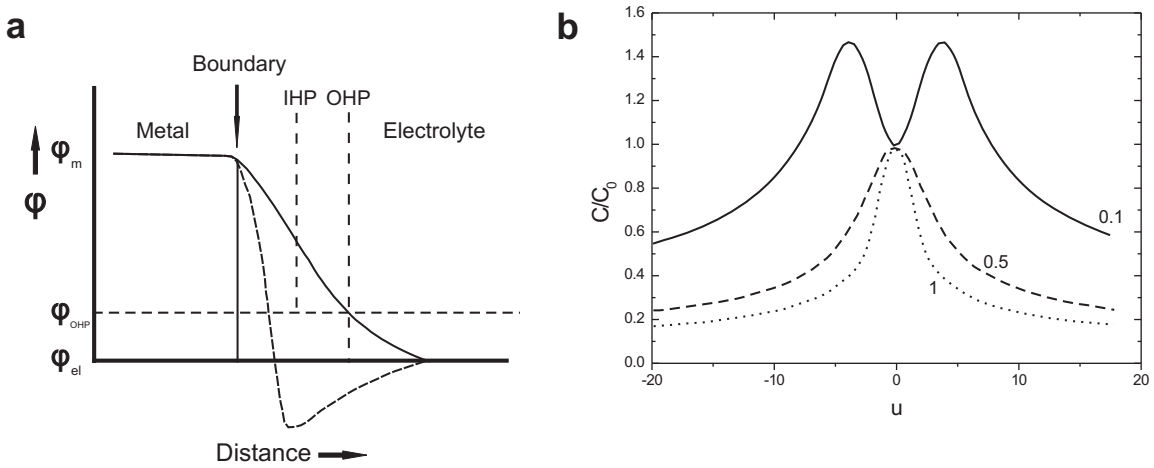

Figure 2.1: (a) Potential distribution across the electrochemical interface for purely electrostatic interactions (nonspecific adsorption) (solid line) and for specific adsorption, causing an „overshoot“ of the potential (dashed line). φ denotes the potential of the outer Helmholtz plane (OHP), of the metal and of the electrolyte, respectively [11]. (b) Double layer capacitance in ionic liquids as a function of the electrode potential u for different values of the lattice-saturation parameter γ. C is the differential capacitance, C_0 is the so-called „Debye“ capacitance [12]).

This model of the double layer has proven good for electrolytes of aqueous salt solutions; however, for ionic liquids – being in the focus of this study – it needs revisions. The strong interaction between the highly concentrated ionic species in ionic liquids leads to an interface which cannot be adequately described by classical models for traditional aqueous electrolytes. Additionally, the adsorption of solvent ions at the electrode/ionic liquid interface makes the interfacial structure much more complex than in aqueous solutions. New theoretical models based on molecular dynamic simulations were developed by Kornyshev [12]. Bell-shaped and camel-shaped potential dependencies of the differential capacitance, exhibiting a maximum and a local minimum close to the potential of zero charge (see next section), is predicted in these models (Fig. 2.1b). The shape of the capacitance curves depends on the so-called γ factor, which denotes the degree of lattice saturation of ions. Later, Oldham predicted also a capacitance curve associated with a maximum at the potential of zero charge [13]. Although significant progress in theoretical calculations and computer simulations were achieved, we are still far away from a comprehensive understanding of the electric double layer in ionic liquids.

2.2 Potential of Zero Charge

One fundamental property of the electrode is its charge. It can be calculated by integrating capacitance with respect to potential; however, for integration the *potential of zero charge* (*pzc*) must be known [14]. The pzc affects the interfacial structure, that is adsorption of ions and molecules, as well as photoemission and electron transfer.

The pzc describes the condition when the electrode carries no excess charge and the charge density of the surface is zero. According to the double layer model established by Helmholtz, the pzc corresponds to the potential where the plate condenser is uncharged. One expects anions in front of the electrode surface at potentials positive of the pzc whereas at potentials negative of the pzc the cations are accumulated at the surface. Neutral (organic) molecules adsorb preferentially at the potential of zero charge in aqueous electrolytes.

In general, the pzc can be determined through the measurement of charge needed while creating (e.g. by immersing the electrode in the electrolyte [15]) or annihilating the interface. Since such measurements involve all charges at the interface, irrespectively of how they are bound to the surface, the zero point of this charge scale is often referred to as *potential of zero total charge* (*pztc*). In contrast, there exists a special case when the double layer charge on the electrolyte side is composed of „free“ charges which are bound to the surface by electrostatic forces only. For this case theories predict specific $C(E)$ functions whose characteristic point mark the pzc. This is the case for the semiconductor/metal or semiconductor/electrolyte junctions for which the pzc (the flatband potential) can be extrapolated from the $1/C^2$ vs. E plot. Another example is the case of metals in dilute electrolyte solutions for which the referring Gouy-Chapman theory [16] predicts a characteristic minimum on the $C(E)$ plot. For these latter cases one often uses the term *potential of zero free charge* (*pzfc*) for distinguishing the two pzcs.

In the absence of specific adsorption the difference in pzfc of two metals can be reasonably compared with the difference in metal/vacuum work functions [17, 18]. In the case of ionic liquids, the relevant pzc is the pztc, mainly because the appearance of chemical interactions between the ions and the electrode surface cannot be excluded. The work function depends on the crystallographic orientation of the surface. The more open the surface the higher the smoothing effect of the electron density distribution on the surface. The kinetic energy of the electrons is reduced, resulting in an electrostatic surface potential. This leads to a decrease of the work function of the different low index surfaces according to the following row: (111) > (100) > (110).

2.3 Surface Reconstruction

Surface reconstruction is a phenomenon by which atoms at the surface of a single crystal assume a different structure than that after bulk truncation in order to minimize the overall surface energy. If a reconstructed phase is energetically more favourable a rearrangement of atoms can occur. Local bond breaking and change of the surface symmetry results in an activation barrier for the reconstruction [19]. A more densely packed structure is formed with an increase of electron density between the surface atom cores. The low-index surfaces of gold, for instance, all reconstruct in order to minimize the surface energy. Au(111) reconstructs into a $(\sqrt{3} \times 22)$ structure consisting of double-rows where zones of (fcc) and (hcp) stacking alternate (Fig. 2.2a and b). Thereby the surface atoms are 4% more densely packed in [110] direction compared to the unreconstructed (1×1) phase. The distance of the double-rows is 4.4 nm with a vertical modulation of 0.15 Å [20].

Au(100) reconstructs into a hexagonal close-packed surface (Fig. 2.2c and d). The (hex)-reconstruction shows a striped pattern with a lateral period of 1.45 nm and a vertical corrugation of 0.5 Å [20].

The same reconstruction phenomena for gold surfaces in aqueous electrolytes were also observed in UHV. The unreconstucted gold surfaces are metastable under UHV conditions, that is, an activation barrier inhibits reconstruction of the uncharged surfaces at room temperature. In aqueous electrolytes, however, if one applies a negative potential (with respect to the pzc) to the unreconstructed gold surface, the reconstructed surface phase is re-formed [22]. This potential-induced reconstruction has been observed for all three low-index gold faces in aqueous electrolytes [23]. Since specific adsorption of anions lifts the reconstuction, it is necessary to immerse the reconstructed electrode under potential control, clearly negative of the pzc. Lifting of the reconstructed gold surfaces leads to an expel of gold atoms due to a lower packing density of the (1×1) structure. The atoms coalesce and form gold islands monoatomic in height. A question of general concern is whether such potential-induced surface reconstruction still prevails in ionic liquids.

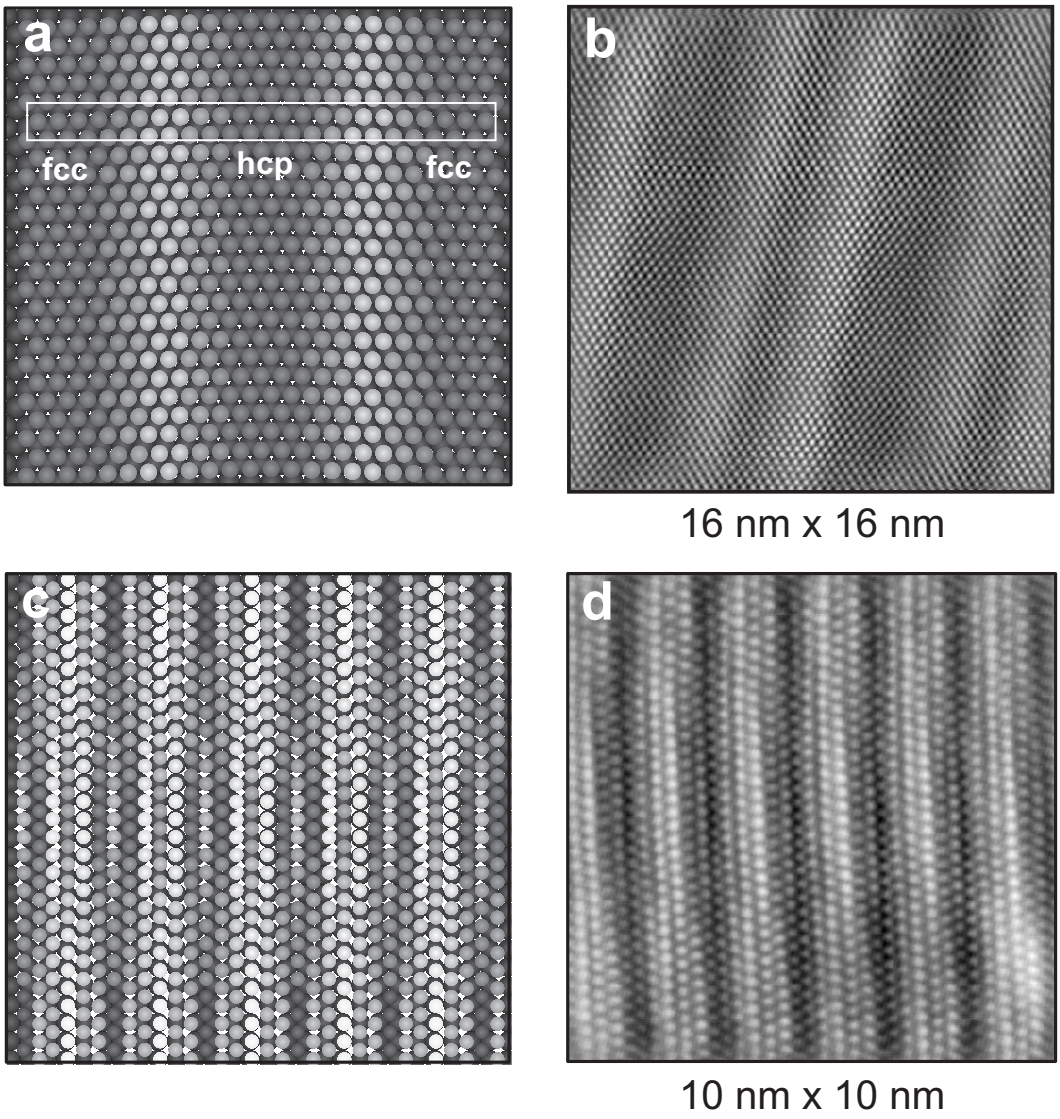

Figure 2.2: (a) Model of the Au(111) reconstruction with ($\sqrt{3} \times 22$) unit cell, (b) high resolution STM image of a reconstructed Au(111) surface in 0.1 M H_2SO_4 at -0.2 V vs. saturated calomel electrode (SCE). (c) Model of the Au(100) (hex)-reconstruction; small spheres represent first layer atoms, big spheres the underlying bulk atoms. (d) High resolution STM image of a reconstructed Au(100) surface in 0.1 M H_2SO_4 at -0.2 V vs. saturated calomel electrode (SCE) [21].

3 Ionic Liquids in Electrochemistry

For industrial applications of electrochemical processes, e.g. electroplating, aqueous electrolytes play a decisive role. The advantages are obvious: High conductivities, good solubilities for metal salts, low viscosities, nonflammability and low costs. Thus the question arises, why should other, non-aqueous electrolytes be used in practical electrochemistry? A big disadvantage of aqueous electrolytes is the limited potential window of about 1.3 V; hydrogen evolution often hampers the deposition of less noble metals at negative potentials. An alternative to aqueous electrolytes are the so-called molten salts. Due to their big lattice energy, however, these compounds exhibit high melting points, mostly around 1000 °C. The high energy costs involved and the fact that only few materials as substrates and structural materials are available set limits to possible applications.

A decrease of the melting point by lowering the Coulomb interaction of the ions can be achieved using appropriate organic ions with sterically hindered substituents. This results in molten salts which are liquid even at room temperature. The so-called room temperature molten salts or ionic liquids are by definition substances which have melting points below 100 °C [24, 25]. The increased electrochemical stability of ionic liquids compared to aqueous electrolytes allows the deposition of reactive and less noble metals like lithium or magnesium which are higly demanded for battery research and production. Other examples are refractory metals like titanium or tantalum used for corrosion protection.

Historically, the first ionic liquids fulfilling the above definition were chloroaluminate melts, based on mixtures of $AlCl_3$ with different organic salts like N-butyl-pyridinium chloride or 1,3-dialkylimidazolium salts [26, 27]. Depending on the mixing ratio potential windows up to 4 V could be realized. The big disadvantage of this system is an extreme hygroscopic behaviour which necessitates handling under inert-gas atmosphere. To avoid these difficulties the synthesis of air- and water-stable ionic liquids began in the early 1990s. These kinds of ILs are composed of organic cations such as 1,3-dialkylimidazolium cation and perfluorinated anions, e.g. $[BF_4]^-$ or $[PF_6]^-$ [7, 28, 29]. However, experiments revealed a more or less rapid water uptake of the ILs under ambient conditions resulting in an hydrolysis of the anions causing the release of HF [30, 31]. For electrochemical studies these liquids still have to be handled under inert-gas conditions. There-

fore, in the latest generation of ionic liquids, ions resistant towards moisture like the bis(trifluoromethylsulfonyl)imide and others are employed [28, 32]. A summary of different cations and anions is given in Fig. 3.1. Despite the still elevated production costs ionic liquids feature as „green electrolytes“ an alternative to toxic and highly volatile organic electrolytes. Because of nearly unlimited combinations of cations with anions ILs can be tailored for specific applications. The BASIL process is an example how the yield in the production of alkoxyphenylphosphine could be increased significantly by the use of ILs [33]. Furthermore, due to their extremely low vapour pressure ionic liquids can be used at temperatures above 100 °C, where conductivity and viscosity is decreased.

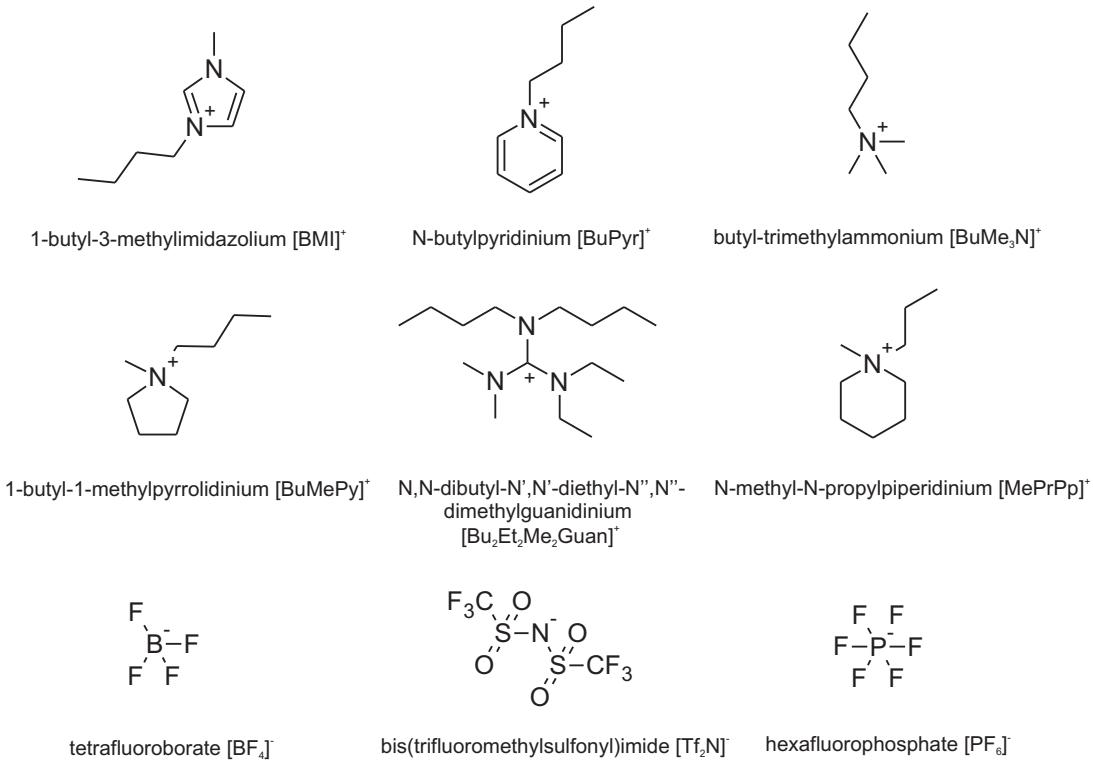

Figure 3.1: Structures of cations and anions with systematic name and abbreviation.

3.1 Synthesis

The synthesis of air- and water-stable ionic liquids on imidazolium-basis is performed in two steps according to the methathesis reaction established by Wilkes *et al.* [7]: Firstly the organic base is alkylated with an appropriate haloalkane. This so-called quaternization reaction is followed by the anion exchange: The halide ion from the alkylation reaction is exchanged against a perfluorinated anion, thereby an inorganic salt precipitates (Fig. 3.2). Thus it is possible to introduce different types of anions such as $[BF_4]^-$, $[PF_6]^-$ or

$[Tf_2N]^-$. Subsequently the halide residuum can be removed by extraction into an organic phase and repeated washing with water.

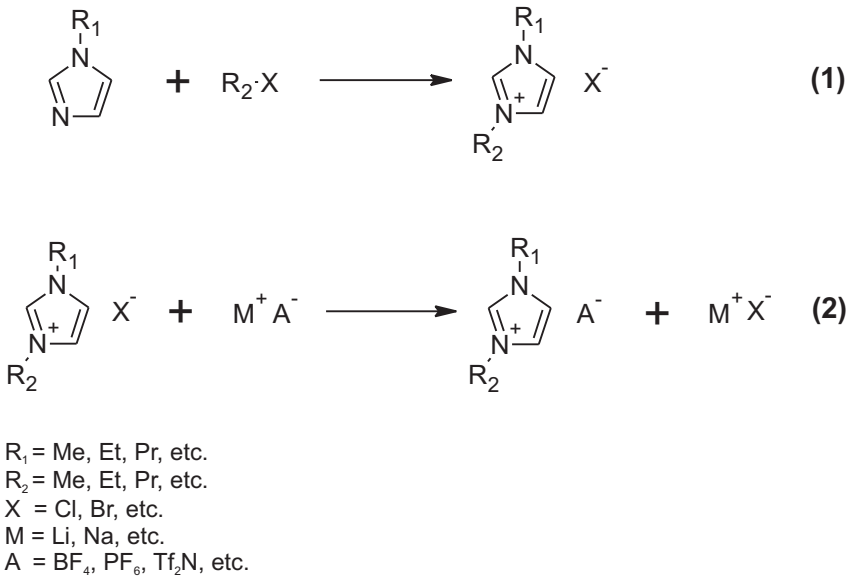

Figure 3.2: Synthesis of imidazolium-based ionic liquids: (1) Alkylation of the organic base, (2) anion exchange.

The electrochemical behaviour of ionic liquids based on hexaalkyl-substituted guanidinium cations have also been studied in this work (chapter 13). A short introduction to the synthesis of guanidinium-based ILs should be given here [35]:

A possible synthesis starts with tetraalkylurea **1** (Fig. 3.3). The reaction with phosgene, phosphoryl chloride or oxalyl chloride leads to chloroformamidinium chlorides **2**. The following reaction with a primary amine yields pentaalkylguanidinium **3**, which can be alkylated with various alkyl halides to hexaalkylguanidinium **4**. Variation of the anion is possible with a subsequent anion exchange [34].

3.2 Physicochemical Properties

Ionic liquids differ in many ways from aqueous electrolytes. Properties like melting point, viscosity, polarity etc. can be controlled by means of selective syntheses. In particular, the electrochemical properties like potential windows, conductivities etc. are of great interest. Despite the vast number of publications the amount of physicochemical data of hitherto synthesized ionic liquids is still low. The following paragraph gives an overview about the essential physicochemical properties (Table 3.1).

Since ionic liquids are organic compounds, their melting points are mainly influenced by van der Waals interactions, hydrogen bonding as well as π–π interactions. Not only the

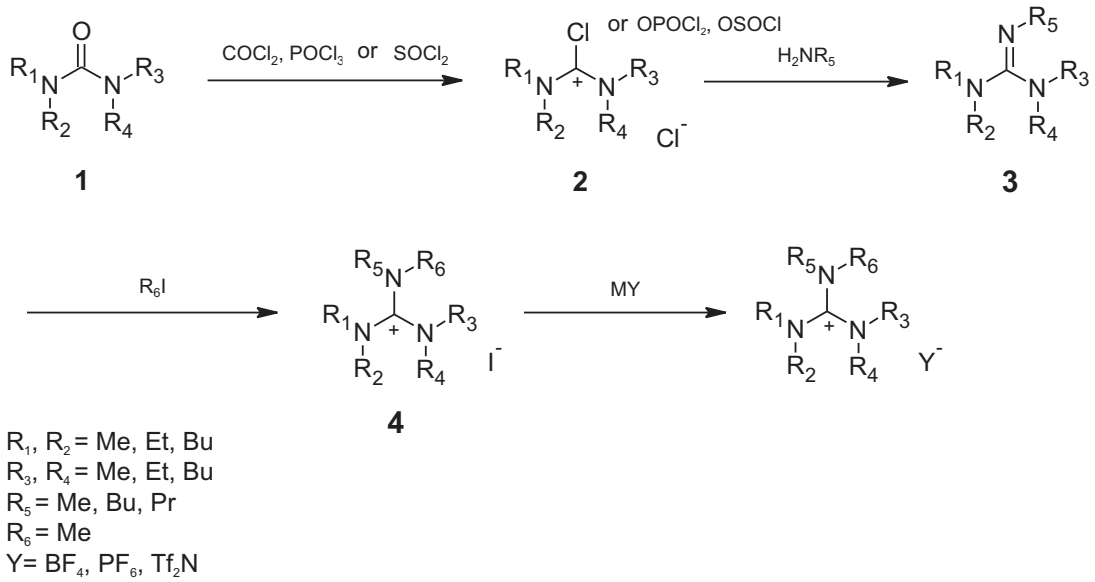

Figure 3.3: Synthesis of guanidinium-based ionic liquids.

size of the ion itself, but also the delocalisation of charge contributes to a decrease of the melting point and to weaken electrostatic interactions between ions. Therefore ILs with aromatic cations generally have a lower melting point than those with aliphatic cations. The length of the alkyl chains also influences the melting point: The longer the alkyl chain of the cation the lower the melting point [36]. Moreover, keeping the same cation the melting point decreases in the same way the size of the anion grows.

Ionic liquids can be utilized also at high temperatures (up to 400 °C). However, thorough investigations show that the thermal disintegration is highly dependent on the water content and the impurities [37]. Usually imidazolium-based ILs, for instance, have a higher thermal stability than ammonium-based Ils. Ionic liquids with halide anions show low thermal stabilities.

Many ILs exhibit vapour pressures at room temperature as low as 10^{-10} mbar. Depending on the liquid the vapour pressure can reach 10^{-3} mbar at 200 °C. The low vapour pressures permit experiments in ultra-high vacuum [38, 39]. It was believed for a long time that ILs do not have any vapour pressure, since even in UHV no apparent distillation rates could be achieved. Therefore the impossibility of purifying ILs via distillation was an accepted opinion. Though, Seddon *et al.* had reported the successful distillation of several ionic liquids at 300 °C under high vacuum, whereas it is still not clear which species predominates in the gas phase [40, 41].

The viscosities of ionic liquids are typically 10 to 100 times larger than that of water [2]. The reasons are mainly due to strong electrostatic interactions as well as hydrogen bonding. Generally ILs composed of big ions show lower viscosities. With keeping the same

cation, for instance, varying the anion leads to an increase of the viscosity according to following row: $[Tf_2N]^- < [BF_4]^- < [PF_6]^-$. Viscosity of ionic liquids is strongly dependent on temperature.

The solubility of metal salts in ionic liquids is smaller than in aqueous electrolytes. The ions coordinate weakly, thus the solvation energy is not sufficient enough to break the ionic bonds in the metal salt. Measuring relative permittivities in ILs yielded values between 10-15 [42]. Experiments concerning solubilities of various metal salts such as LiCl or $HgCl_2$ showed that the solubility for ILs containing the $[BF_4]^-$ anion is better than for the $[PF_6]^-$ ions. Only small solubilities of 10^{-4} wt% could be determined [43]. In order to increase the solubility ILs with functional groups (task-specific ILs) are synthesized. Another approach is an enhancement of the interaction between IL and metal salt using complexing agents, e.g. crown ethers. By means of these agents the metal salt is transferred from an aqueous phase into the IL phase [44].

Of particular interest to electrochemisty is the stability range of the electrolyte, the so-called potential window which is normally determined by means of cyclic voltammetry. Typically current densities of 1 $mAcm^{-2}$ can be achieved in ionic liquids at the anodic and cathodic limit of the potential window applying a sweep rate of 50 mV/s [45]. It is assumed that the potential limits are caused by the oxidative and reductive decomposition of the anion and cation, respectively. Imidazolium-based Ils feature potential windows of about 4 V. Piperidinium-based ILs are more stable against oxidation and reduction having potential windows of 5 V and more. The range of the potential window depends on the electrode material, sweep rates, temperature, impurities, etc. [46]. Especially impurities such as water or halides narrow the potential window significantly. Commonly silver and platinum wires are used as pseudo-reference electrodes. The development of stable reference electrodes on an IL-basis is still at the beginning. Katayama *et al.* reports the successful application of an Ag/Ag^+(IL) reference electrode [47].

In accord with their high viscosity, conductivities of ionic liquids are rather low. Several imidazolium-based ILs can reach values up to 10 mS/cm. Piperidinium-based ILs show smaller conductivities of 0.1-5 mS/cm [46]. For comparison, a 1 molar aqueous sulphuric acid electrolyte has a conductivity of 366 mS/cm [48].

Strong electrostatic interactions between the ions and concomitantly an increased viscosity is associated with hindered diffusion. At room temperature the self-diffusion coefficient of water is 10^{-9} m^2s^{-1} [49]. In contrast, the diffusion coefficients of the ions in imidazolium-based ILs are around 10^{-11} m^2s^{-1} [50]. Usually cations have larger diffusion coefficients than anions.

	ρ (g/cm^3)	c (mol/dm^3)	T_m (°C)	η (cP)	D^+/D^- (10^{-11}m^{2}s^{-1})	σ (mS/cm)	PW(V)
$BMIPF_6$	1.36 (20 °C) [51]	4.8 [51]	10 [51]	312 (20 °C) [51]	0.89/0.71 (30 °C) [52]	1.4 (20 °C) [51]	3.2 (Pt) [53]
$BMIBF_4$	1.17 (20 °C) [51]	5.2 [51]	-81 [55]	233 (20 °C) [51]	1.8/1.8 (30 °C) [52]	1.73 (20 °C) [51]	4.2 (GC) [54]
$BMITf_2N$	1.43 (19 °C) [28]	3.4 [28]	-4 [51]	52 (20 °C) [28]	3.4/2.6 (30 °C) [52]	3.9 (20 °C) [28]	4.6 (Pt) [56]
$BuMePyTf_2N$	1.41 (20 °C) [64]	3.3 [64]	-10.8 [65]	85 (25 °C) [64]	2.51/1.97 (32 °C) [66]	2.2 (25 °C) [64]	5.5 (GC) [57]
$MePrPpTf_2N$	1.32 [58]	?	8.7 [59]	117 (25 °C) [60]	?	1.51 (25 °C) [60]	5.6 (GC) [61]
$BuPyrBF_4$	1.22 (25 °C) [62]	5.5 [62]	15 [61]	?	0.91/1.0 (25 °C) [63]	1.9 (25 °C) [62]	3.4 (Pt) [61]
$BuMe_3NTf_2N$	1.41 (20 °C) [64]	3.7 [64]	7 [64]	116 (25 °C) [64]	1.7/1.4 (30 °C) [52]	1.4 (25 °C) [64]	4 (Gr) [64]

Table 3.1: Physicochemical properties of ionic liquids. ρ: Density, c: Concentration, T_m: Melting point, η: Viscosity, σ: Conductivity, D^+ and D^- denotes the diffusion coefficient of the cation and the anion, PW: Potential window (working electrodes in parentheses, GC: Glassy carbon electrode, Gr: Graphite).

3.3 Electrodeposition of Metals

The outstanding electrochemical property of ionic liquids is the broad potential window. Thus, it is possible to deposit less noble metals which cannot be deposited from aqueous electrolytes. Due to the high viscosity, diffusion coefficients are lower compared to aqueous electrolytes resulting in a slow deposition process. However, ILs can be used in a wide temperature range and kinetic barriers can be overcome. Hence a better control of the metal deposition is possible. The solvation of metal ions differs strongly from aqueous electrolytes. Owing to weakly coordinating anions for example $[BF_4]^-$ or $[PF_6]^-$ the metal ions do not longer exhibit solvation shells, they rather exist in a „naked“ state. On the other hand the formation of solvation shells on transition metals, e.g. manganese, cobalt or zinc, with strongly coordinating anions such as $[Tf_2N]^-$ have been observed [67].

The first experiments for metal deposition were successfully performed in chloroaluminate melts. From these melts, mainly aluminium as well as less noble metals like copper could be deposited [68]. The cathodic limit of the potential window, however, is determined by the reduction potential of aluminium. Therefore, deposition of less noble metals than aluminium is difficult due to an undesired codeposition and alloy formation with Al [69]. A major disadvantage of chloroaluminate melts is their corrosiveness and sensitivity against moisture which necessitates handling under inert-gas atmosphere. The synthesis of air- and water-stable ionic liquids with broad potential windows opened up new possibilities for the deposition of highly reactive metals, for instance Mg or Li.

Mg and Li are important metals for battery applications. Although studies for Mg deposition from aprotic solvents already exist, investigations in ionic liquids are still at the beginning [70, 71]. Experiments clearly showed that the cathodic limit of the potential window in imidazolium-based ILs is not sufficient enough for the deposition of magnesium. Instead, electrolytes with an extended cathodic stability range, e.g. pyrrolidinium-based ILs, have to be used [72].

Titanium and tantalum deposited as thin films are highly demanded for corrosion protection. Endres *et al.* demonstrated the feasibility of tantalum deposition at elevated temperatures: A fine grained, porous Ta coating could be obtained from TaF_5 solutions. More uniform tantalum coatings were received adding LiF [73, 74]. The first experiments in titanium deposition proved to be particularly difficult. Instead of elemental titanium non-stoichiometric titanium halide compounds were detected on the substrate [75]. Employment of adequate Ti-precursors like $Ti(Tf_2N)_4$ or Ti-alcoholates in association with ionic liquids with broad potential windows could facilitate the titanium deposition. It is well known that all refractory metals tend to form subvalent, non-stoichiometric me-

tal halide compounds [76]. For this reason the metal deposition from appropriate halide precursors might be difficult.

Good mechanical properties, low electric resistance as well as a high corrosion resistance make copper an important material for nanoelectronics. The deposition of copper from aqueous electrolytes has been thoroughly studied [77,78]. A dense, microcrystalline copper deposit without using additives could be obtained from $BMITf_2N$ [79].

Due to its high catalytic activities for many chemical reactions Pd is not only interesting for basic research. Experiments exploring the Pd deposition in aqueous electrolytes have already been performed [80, 81]. However, little is known about Pd deposition from ionic liquids. Sun *et al.* demonstrated the deposition of Pd/Ag- and Pd/Au-alloys from chloride containing ionic liquids [82, 83].

The morphologies of the deposits of ferromagnetic elements like iron or cobalt are closely related with their magnetic properties. An ordered growth can be observed in case of iron deposition from $BMIBF_4$. The growth is explained with a local influence of magnetostatic interactions during the deposition process [84]. Nano-structuring of surfaces via controlled deposition of Fe-clusters was realized by means of the scanning tunneling microscope [85]. The cobalt deposition on Au(111) begins with the formation of clusters monoatomic in height, finally developing into islands [86].

Semiconductors such as silicon and germanium, which are important for optoelectronic applications, could also be successfully deposited from ionic liquids. A two-dimensional growth of germanium islands onto Au(111) was observed in case of deposition from $BMIPF_6$ [87]. Deposition of silicon from $BuMePyTf_2N$ also showed an island growth [88, 89]. Subject of current research is the creation of functionalized, nano-structured wires made up of germanium and silicon [90, 91].

4 Methods

4.1 Cyclic Voltammetry

Cyclic voltammetry (CV) is a commonly employed technique in electrochemistry where the current response of an electrochemical system is recorded while imposing a periodic, triangular potential wave. This method is often used to survey the reactivity of new materials and compounds. A CV measurement yields a plot of the current density versus potential. Because of the constant sweep rate the potential axis is also an energy axis, therefore CV is sometimes named electrochemical spectroscopy [92, 93]. The resulting CV curve gives an overview of electrochemical processes taking place within the selected potential range. Electron transfer reactions as well as adsorption processes can be related with current peaks in the CV. Determination of thermodynamic parameters like redox potentials and of kinetic parameters, e.g. the rate coefficients of electrode reactions is possible. Integration of the current peaks yields charge densities which may be indicative for the amount of electrochemically active species present at the interface as well as for surface coverages.

For electrochemical interface studies normally three-electrode cells are employed with working, reference and counter electrodes (WE, RE and CE, respectively); the electrode potential, that is, the voltage between WE and RE is controlled by the operational amplifier (OPA), which constitutes the most important part of a potentiostat (Fig. 4.1a). The potentiostat's operation principle is based on that the potential of the two inputs (+ and –) of the OPA must always be practically the same, consequently the electrode potential is the negative of the program voltage U. Voltammetry is a collective term for methods in which the potential as a function of time, $E(t)$ is set (and re-measured) and current-time function, $I(t)$, is measured (or, for the so-called galvanostatic techniques, $I(t)$ is set and $E(t)$ is measured). For CV, the program voltage comprises linearly changing sections between limits, as illustrated in Fig. 4.1b. Depending on the system and on the purpose of study, sweep rates between 10^{-4} to 10^{3} V/s are used; in the present work 50 mV/s was mostly applied.

To illustrate the CV plot features, a measurement on a typical Au single crystal ionic

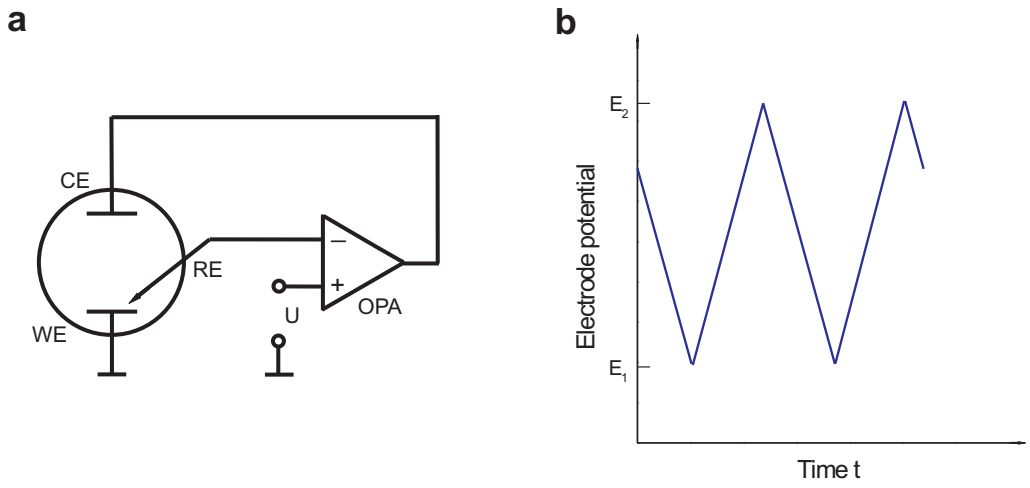

Figure 4.1: (a) Three-electrode system: WE = working electrode, RE = reference electrode, CE = counter electrode, OPA = operational amplifier, U = program voltage. Current is usually measured at the WE (not shown). (b) Triangular potential-time behaviour between the potential limits E_1 and E_2, sweep rate is defined as $\nu = |(dE/dt)|$.

liquid system is shown in Fig. 4.2. In the CV one observes so-called faradaic currents (cathodic current at -2 V and anodic hump at -0.4 V) as well as charging currents or non-faradaic currents (double layer region between -0.7 V and -2 V). Faradaic currents can be related with a charge transfer accross the interface whereas charging currents are due to the double layer charging. From an electrical point of view the circuit element associated to faradaic currents is a nonlinear resistor while non-faradaic currents are associated with capacitors (see section Electrochemical Impedance Spectroscopy). The large cathodic currents occuring at -2 V can be attributed to a reductive decomposition of the ionic liquid. The anodic hump at -0.4 V marks the reoxidation of the reduced species.

4.2 Electrochemical Impedance Spectroscopy

Electrochemical impedance spectroscopy (EIS) is another method used in order to characterize electrode processes and complex interfaces. It can be used for the determination of kinetic parameters (e.g. charge transfer across the interface, mass transport) as well as interfacial parameters (double layer capacitances) [94,95]. A prerequisite, however, for the determination of parameters is an established model. Therefore, studying new systems, e.g. ionic liquids, interpretations have to be done very carefully. In general, EIS experi-

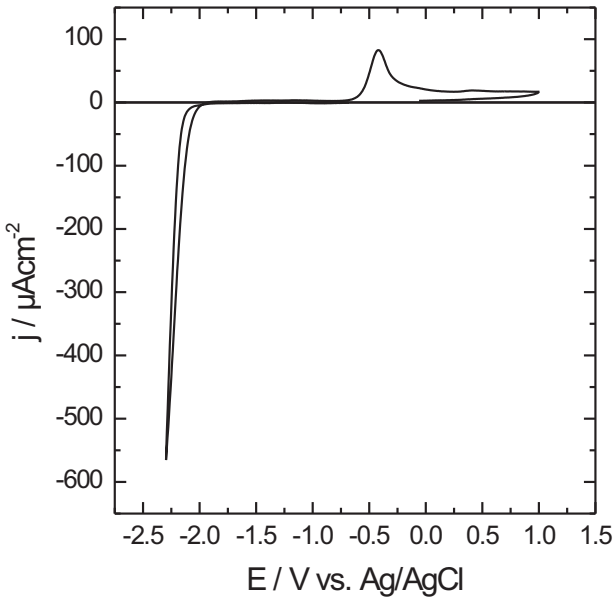

Figure 4.2: CV of Au(100) in $BMIPF_6$, $\nu = 50$ mV/s.

ments are carried out in such a way that the interface is perturbed from its steady state by means of a small additional voltage or current.

Consider an electrical system in steady state, e.g. an electrode whose potential is sinusoidally perturbed with frequency f, that is,

$$E(t) = E_{dc} + E_0 \sin(\omega t) \tag{4.1}$$

where the angular frequency is $\omega = 2\pi f$. Accordingly, the current will also change sinusoidally, however, there will be a phase difference, φ, between potential and current perturbations (Fig. 4.3a):

$$I(t) = I_{dc} + I_0 \sin(\omega t + \varphi) \tag{4.2}$$

Assume that the system is linear, that is, the perturbation amplitudes E_0 and I_0 are proportional to each other (in the electrochemical practice this condition is ensured by applying small ($E_0 < 5$ mV) perturbation amplitudes). Then the system's dynamic behaviour can be represented by the E_0/I_0 amplitude ratio and φ phase shift pair (both of which depend on ω). Such a number-pair can be regarded as a complex number and thus the complex quantity Z (impedance) is defined as

$$Z(\omega) = \frac{E_0}{I_0}\, e^{i\varphi} = Z_{abs}\, e^{i\varphi} \tag{4.3}$$

where Z_{abs} is the absolute value or magnitude of the impedance and φ is its phase angle. Z can be resolved into two components, the impedance component in phase with the cell voltage (Z_{real}) and the impedance component at 90° to it (Z_{imag}), which is called the imaginary part of the impedance (Fig. 4.3b). The reciprocal of the impedance, $Y = 1/Z$,

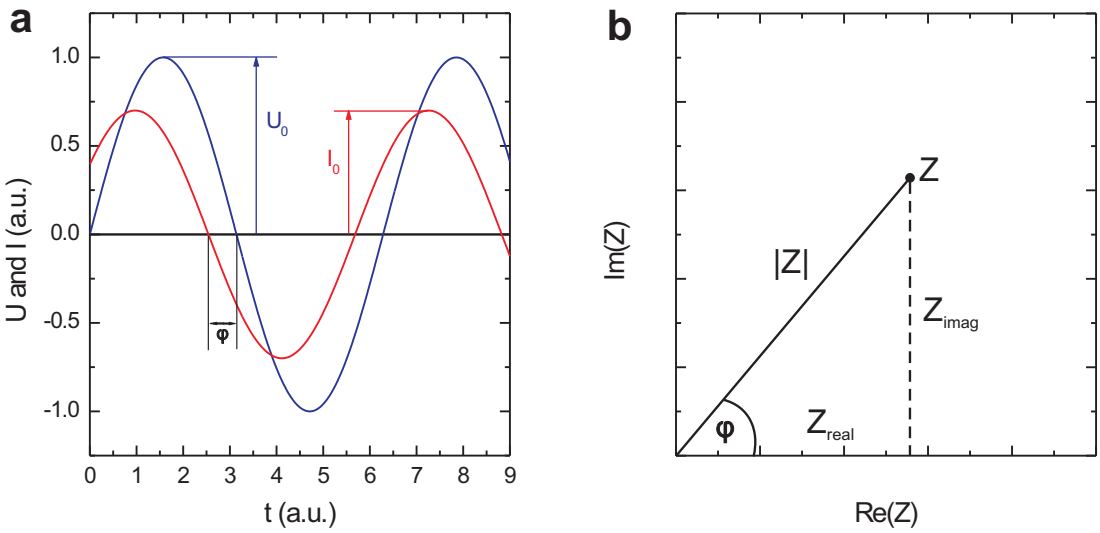

Figure 4.3: (a) Sinusoidal voltage stimulus and current response, (b) impedance on the complex plane.

is named admittance. Since Z is a frequency function, the impedance measurement method can be regarded as a spectroscopy, hence it is often referred to as electrochemical impedance spectroscopy, EIS. The usual frequency range of the method is 1mHz $< f <$ 1 MHz. The impedance spectra – and its descendants, e.g. the $C(\omega) = 1/(i\omega Z(\omega))$ complex capacitance spectra – are usually plotted in two formats: First – as being complex numbers, functions – they can be plotted on the complex plane. These plots are called by mathematicians Argand-diagrams, however, in the context of electricity, their name is Nyquist plot. For a resistive-capacitive system, which is quite typical in electrochemistry, -Im$Z(\omega)$ is plotted vs. Re$Z(\omega)$, as exemplified in Fig. 4.4a. Second, it is a frequent practice to plot $\log(Z(\omega))$ =$\log(Z_{abs}(\omega) \cdot exp(i\varphi(\omega)))$ =$\log(Z_{abs}(\omega)) + i\varphi(\omega)$ as a function of $\log(f)$, in the form as shown in Fig. 4.4b. This is the so-called Bode plot which has the advantage over the Nyquist plot that also the frequency information is included.

The impedance function of the electrochemical system is usually visualized as – and interpreted in terms of – equivalent circuits, which are electrical networks of the same or similar impedance functions as that of the system under study. Equivalent circuits consist of resistors, capacitors and other elements. The most common elements are the

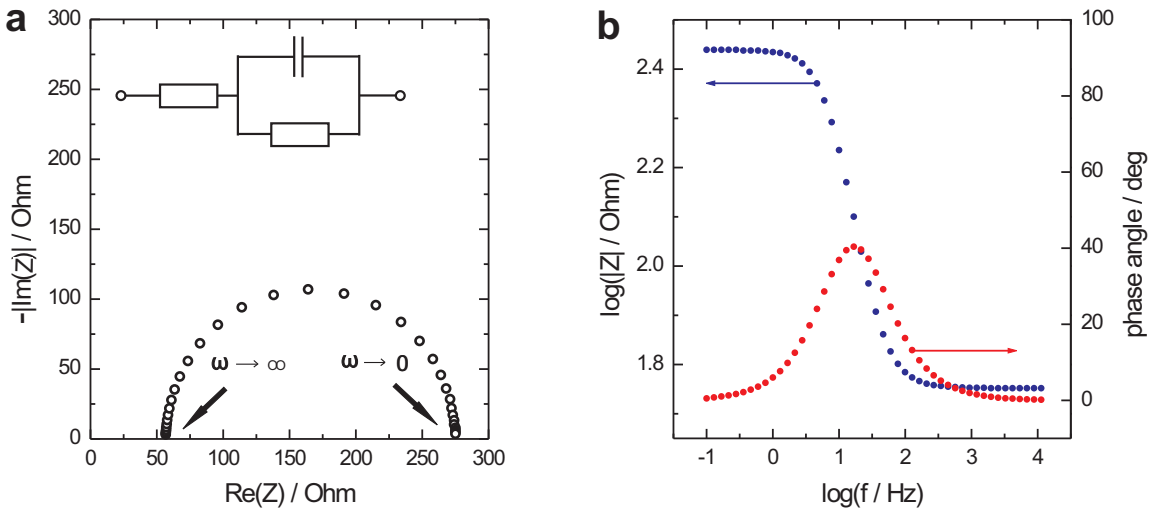

Figure 4.4: (a) Nyquist plot of a resistor in parallel to a capacitance, (b) corresponding Bode plot.

resistance of a bulk phase, the double layer capacitance, the charge transfer resistance, the diffusional (Warburg) impedance, the adsorption impedance and the constant phase element (CPE). Their roles are as follows:

- The bulk resistance – often named as serial or solution resistance – represents the resistance of the electrolyte between the working electrode outside and the reference electrode. It holds information of little (if any) value in interfacial studies, thus its value is usually discarded.

- Charge transfer resistance is (inversely) related to the rate of charge transfer across the interface; thus its value is the main result of EIS measurements of studies on electrode kinetics, e.g. of characterizing corrosion (metal dissolution). In our studies plays no role.

- Double layer capacitance is related to the ions bound electrostatically to the electrode surface – it is the quantity which is interpreted by the double layer models.

- Diffusional impedance: It appears typically when a species involved in an interfacial process (charge transfer or adsorption) is a minor component of the electrolyte and moves to and from the surface by diffusion rather than migration. For planar electrodes, its form is $Z(\omega) = \text{const.}/\sqrt{i\omega}$. Impedance elements with such a reciprocal square-root frequency dependence are often called as Warburg-impedances, even

if they have nothing to do with diffusion. Its effect may be pronounced at low frequencies.

- Adsorption impedance: The adsorption of an electrolyte species may appear as a serial combination of a capacitance, a resistance and a diffusion impedance; as a thumb's rule, the resistance appears when the adsorption is slow; the last term appears when the adsorbate concentration is low.

- Constant phase element (CPE) is an empirical impedance element defined by its impedance as $Z_{\mathrm{CPE}}(\omega) = Q/(i\omega)^n$ where Q and n are the CPE coefficient and exponent, respectively. Note that for $n = 0, 1/2$, and 1 the CPE becomes a resistor, Warburg impedance, and capacitance, respectively (Fig. 4.5a). The most frequent reason for the appearance of a CPE in the equivalent circuit rather than of an „ordinary element" like a capacitance is that some process is not uniform along the interface, e.g. due to some surface inhomogeneities [96, 97]. For example inhomogeneous reaction rates on the surface might occur on polycrystalline metal surfaces or carbon electrodes with a distribution of active sites (variations in activation energies) on the surface [98]. Different thickness or composition of an electrode coating as well as non-uniform current distributions can also be approximated using CPEs [99–101].

One of the most frequent equivalent circuit to be found in the electrochemistry literature is the Randles-circuit (Fig. 4.5b, inset), which applies if there is a charge transfer (faradaic) process across the interface; the interfacial reaction is represented by the R_{ct}-W (charge transfer resistance – Warburg impedance) branch. A corresponding impedance spectrum is shown in Fig. 4.5b.

In those cases, when no faradaic process proceeds on the surface, but some species is adsorbed on the surface, then the interfacial reaction branch is an adsorption impedance (Fig. 4.6a inset); the low frequency part of the impedance on the complex plane plot tends to be vertical at low frequencies (Fig. 4.6b). In these cases it is instructive to transform the $Z(\omega)$ spectra to interfacial capacitance spectra by calculating the $C(\omega) = 1/(i\omega(Z(\omega) - R_s))$ complex function. Classical adsorption theories [102–104] predict a capacitance spectrum $C(\omega)$ of the form

$$C(\omega) = C_{dl} + \frac{C_{ad}}{1 + \sigma_{ad} C_{ad} \sqrt{i\omega} + R_{ad} C_{ad} i\omega} \tag{4.4}$$

where σ_{ad} is the coefficient of diffusional (Warburg) impedance. R_{ad} and σ_{ad} represent the kinetics of the adsorption. Because of its physical meaning $C(\omega)$ is termed the „interfacial capacitance" and, being a complex quantity, can be plotted in complex representation

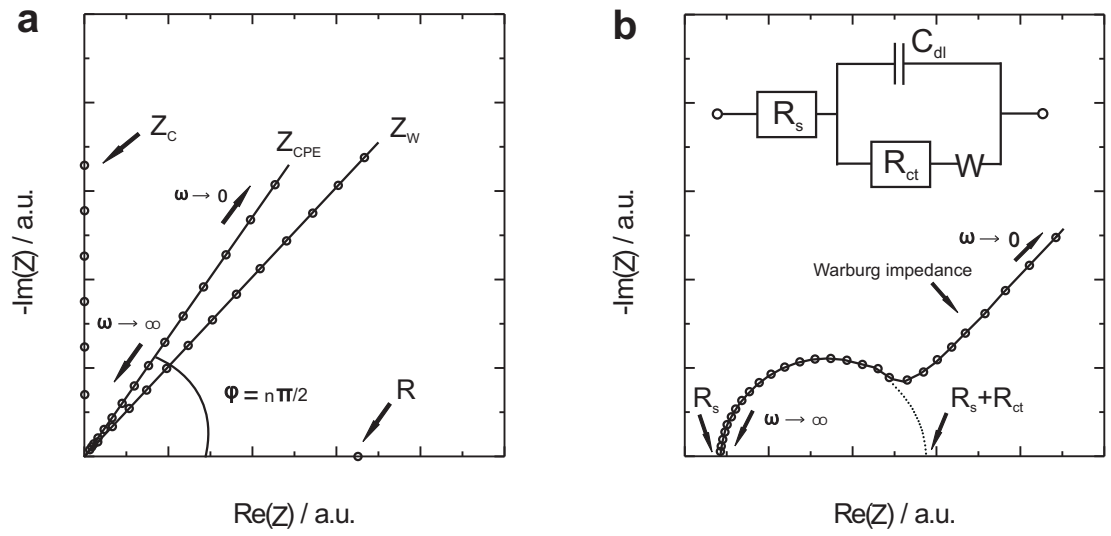

Figure 4.5: (a) The impedance of a resistor R, a capacitor C, a Warburg element W, and a CPE. (b) Impedance spectrum of the Randles-circuit (shown in the inset). Note that the high and low frequency limits correspond to R_s and to the W element, respectively.

(C-Nyquist plot, see Fig. 4.6a). In case of adsorption processes the arcs in the spectra become obvious in the C-Nyquist representation, rather than in an ordinary Z-Nyquist plot (compare Fig. 4.6b), with C_{dl} and C_{ad} easy to determine. Throughout this work the measured spectra are presented graphically by calculating and plotting the $C(\omega)$ complex function.

The result of the impedance measurement is the $Z(\omega)$ spectrum. In most of the cases spectrum evaluation is done in two steps: First the parameters of an appropriate equivalent circuit is determined by curve fitting; the quantities of physico-chemical significance are calculated from those (e.g. rate coefficients from resistances) afterwards [105]. Curve fitting is done by minimizing the $\sum_i (Z_{i,m} - Z_{i,c})^2 / w_i^2$ sum, where the m and c sub-scripts refer to the measured and calculated impedance data and w_i is the weight factor of the ith data point. Since the relative accuracy of the data points is approximately constant along the spectrum, usually $w_i = Z_{i,c}$ is chosen („modulus weighting“) hence the $\sum_i (Z_{i,m} - Z_{i,c})^2 / Z_{i,c}^2 = \sum_i (1 - Z_{i,m}/Z_{i,c})^2$ sum is minimized, employing some minimization algorithm. A frequent practice is to fit the high frequency part of the spectra only, for the determination of R_s. This way the interfacial and the electrolyte bulk parts of the spectra can be separated, and the interfacial capacitance function can be calculated and displayed e.g. on the complex plane.

The steady state of the system is an essential condition of impedance measurements.

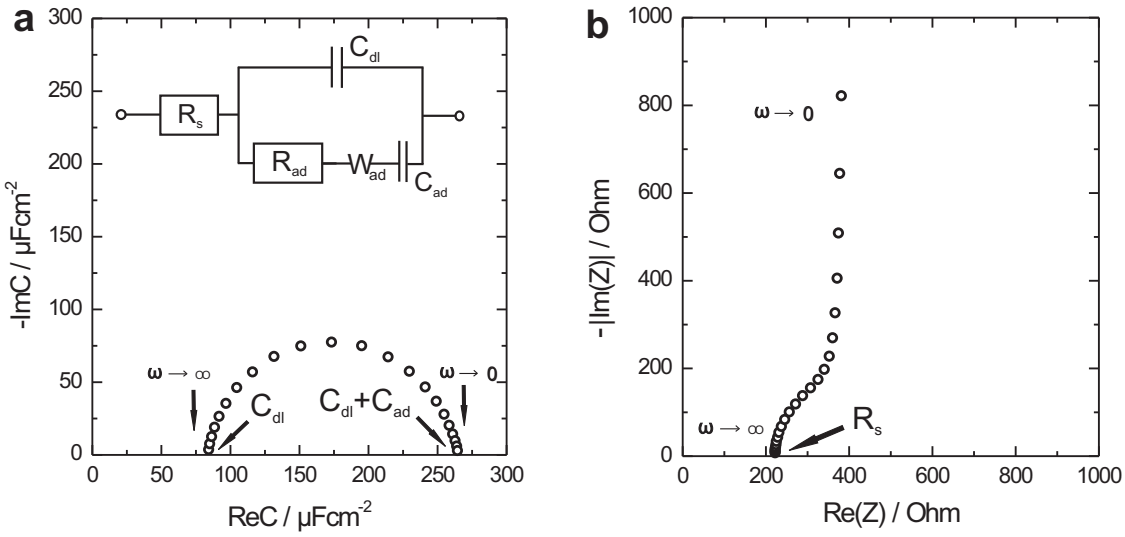

Figure 4.6: (a) Equivalent circuit and C-Nyquist plot in case of adsorption, (b) corresponding Z-Nyquist plot.

After setting or changing potential one has to wait until the system settles; the impedance measurement can be started only then. However, after the measurement, the steady state condition can be – and in fact was regularly – checked using the Kramers-Kronig transformation [106] by which the distortions in the low frequency part can be identified.

Impedance measurement programs are nowadays standard accessories of potentiostats and are routinely used for the characterization of many and diverse electrochemical systems. However, this is a method which is to be used for a well-known system only, for the precise determination of parameters (rate constants, capacitances, etc). Accordingly, the measurements discussed in the next chapters are aimed at the determination of interfacial capacitances of the Au/ionic liquid interfaces.

4.3 Scanning Tunneling Microscopy

In 1982 the scanning tunneling microscope (STM) was developed by G. Binnig and H. Rohrer as a technique for imaging surfaces on an atomic level [107–109]. Unlike other surface analytical methods (e.g. low energy electron diffraction, LEED), the STM is able to image surface structures in real space. Among other imaging techniques like the atomic force microscope (AFM) or the magnetic force microscope (MFM) the STM belongs to the so-called scanning probe microscopes (SPM) [110]. In 1986, only five years after the first successful operation of a STM, Binnig and Rohrer received the Nobel Prize in physics [111].

The conceptual simplicity of the STM is stunning: By means of a metallic tip the surface

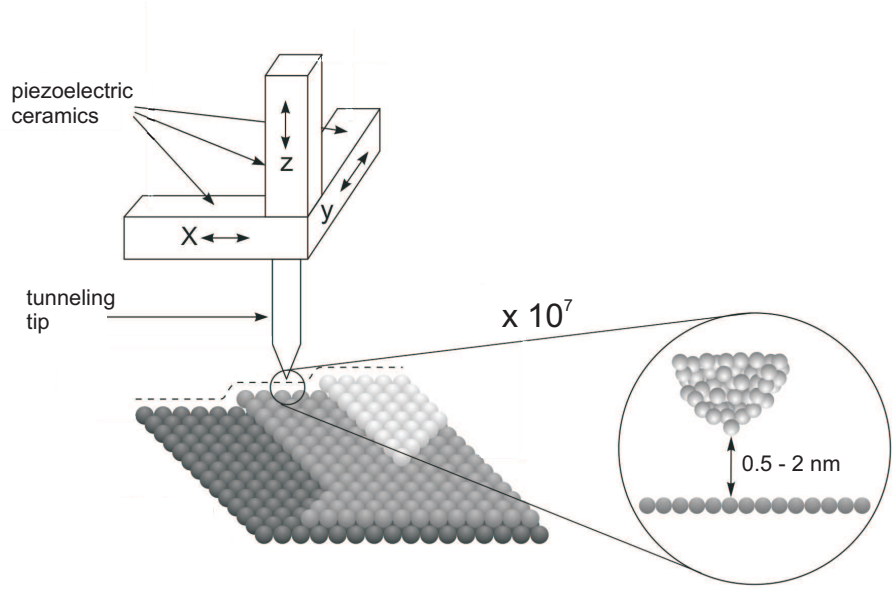

Figure 4.7: Schematic diagram showing the principle of STM [112].

topography of a conducting or semiconducting material is scanned revealing its surface structure with atomic resolution. The STM tip is kept at a certain distance to the surface without mechanical contact (Fig. 4.7); positioning of the tip in all three spatial directions can be accomplished by means of piezoelectric ceramics. As the STM tip approaches the surface the wave functions of tip and sample overlap. Electrons are able to pass the barrier which results in a tunneling current. Electrons penetrating a barrier is a well known phenomena in quantum mechanics and can be understood via quantum tunneling [113]. Applying a potential difference between tip and sample the resulting tunneling current, I_t depends exponentially on the sample-tip distance [114, 115]:

$$I_t \propto U_t \; e^{-A\sqrt{\Phi_t}s} \tag{4.5}$$

where A is a constant, depending on the work funktions of tip and sample, U_t the tunneling voltage, Φ_t the tunneling barrier and s the tip-sample distance, respectively. Hence small changes in tip distance results in large variations of the tunneling current. For example, distance variations of 1 Ångström with a supposed tunneling barrier of 2-4 eV leads to variations in the tunneling current of one order of magnitude [116]. The tunneling current is directly associated with the electronic properties of the surface. Thus the STM image represents contours of constant local density of states (LDOS) at the Fermi level [117,118]. Fig. 4.8 shows a schematic energy diagram of the tunnel junction between a metal surface

and a metallic tip. Electrons tunnel from occupied states of the tip into empty states of the sample. Typical values for the tunneling barrier Φ_t are 3-4 eV for tunneling in UHV and 1-2 eV for tunneling in aqueous electrolytes [119, 120]. In case of metals the positions of the nuclei coincide with the topography. Differences, however, can be expected in case of semiconductors or modified surfaces (e.g. ion adsorption). The resulting variations in the LDOS make interpretations difficult.

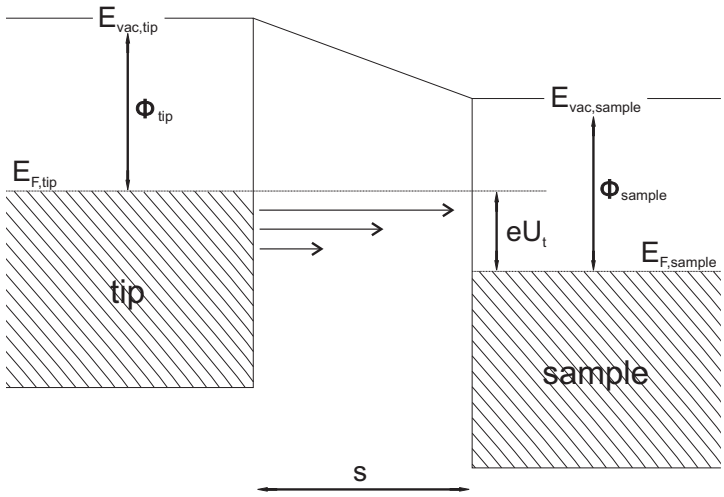

Figure 4.8: Tunnel contact between two metals. E_{vac} is the vacuum level, E_F the Fermi level and Φ the work function of tip and sample, respectively. S denotes the tip-sample distance.

The STM is constructed to operate in two different modes (Fig. 4.9). The most commonly used mode of operation is the constant current mode: Piezoelectric drivers force the tip to be always at a certain distance to the sample surface; thus the tunneling current flowing between these two electrodes remains constant. A topographical image can be obtained recording the voltage applied to the piezoelectric driver. The constant current mode is used for atomically rough surfaces, e.g. stepped surfaces. A disadvantage of this mode is the finite response time of the feedback loop, resulting in relatively low scan speeds. In order to increase the scan speed considerably, the constant height mode has been introduced [121]. In this mode, the tip is rapidly scanned over the sample surface at constant height while the feedback loop is switched off completely. The variations in the tunneling current, which are recorded as a function of location, contain the topographic information. The constant height mode is primarily employed to atomically flat surfaces.

In its early days, STM experiments were only used in UHV but further development allowed applications in the gas phase as well as in the electrolyte [122, 123]. From then on the STM was also used for the study of reactions at the electrode/electrolyte interface; and it has become an invaluable tool for electrochemistry. An *in-situ* application of the STM

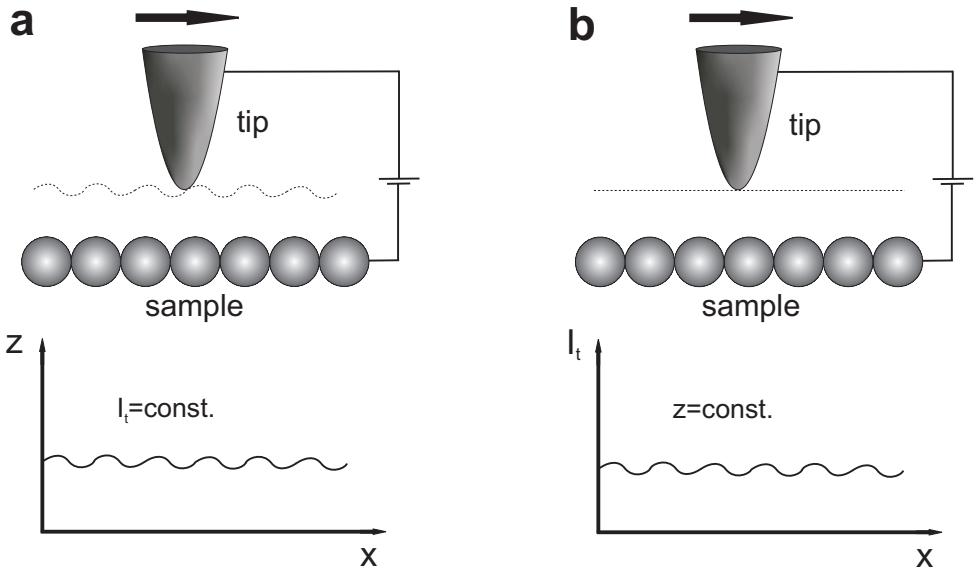

Figure 4.9: (a) Constant current mode, (b) constant height mode.

in electrolytes, though, requires some modifications. For potential control at the working electrode (sample) a reference as well as a counter electrode is necessary. The STM tip constitutes a fourth electrode since it is also immersed into the electrolyte. Independent potential control of the sample and of the tunneling tip against the reference electrode is achieved with bipotentiostatic circuits: The potential difference of tip and sample defines the tunneling voltage: $U_\mathrm{t} = U_\mathrm{tip} - U_\mathrm{sample}$. The electrochemical reactions which occur at the complete surface of the tip cause faradaic currents superimposed the tunneling current. For this reason an insulation of the tip is necessary in which only the very end of the tip remains uncovered [124]. By means of the insulation it is possible to reduce the faradaic current from 1 μA to about 50 pA. Moreover, the proximity of tip and sample causes an overlap of the double layers interacting with each other. This results in inhomogeneous field distributions underneath the tip generating shifts in the potential. Furthermore, mass transport below the tip is hindered which influences the observed reaction kinetics making experiments with high overpotentials necessary [125].

Part II

Experimental

5 Electrochemical Cells

Two types of electrochemical cells were employed. One type was used for *in-situ* STM measurements and cyclic voltammetry. Since it is an open cell, it was also used for determining the potential of zero total charge. A closed cell comprising a heating unit was used for impedance measurements.

5.1 STM Cell

The electrochemical cell was made of polytrifluoroethylene (Kel-F), which is a chemically inert and temperature-resistant material (Fig. 5.1). Before each measurement the cell as well as the O-rings (Kalrez) were thoroughly cleaned from remaining ionic liquid with aceton (Merck, p.A.). Assembling of the cell was performed according to the following

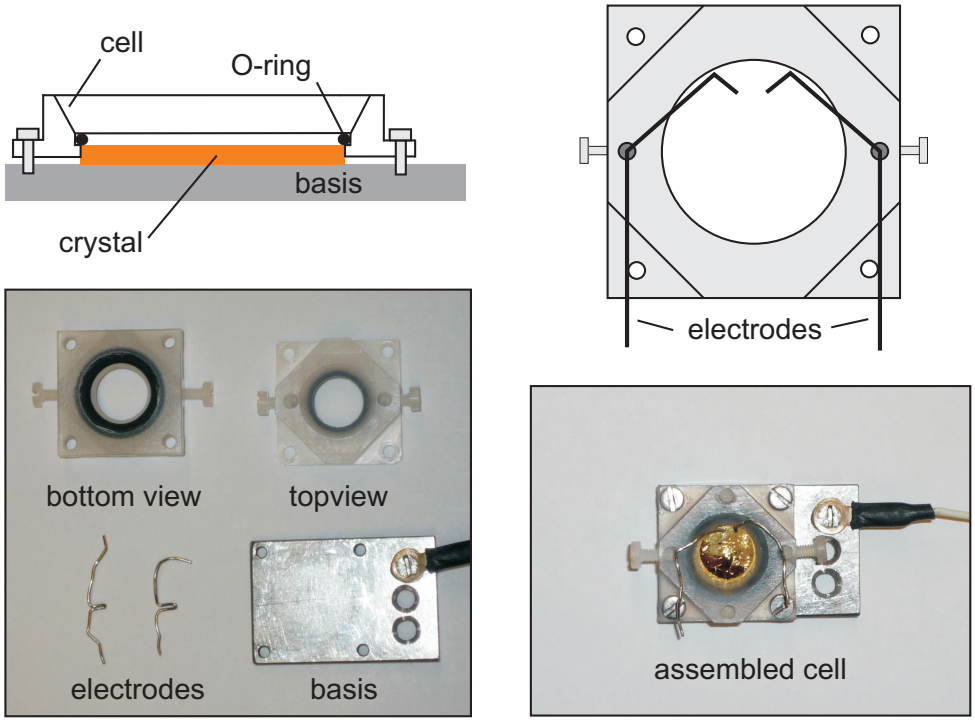

Figure 5.1: Electrochemical cell used for cyclic voltammetry, *in-situ* STM and immersion experiments.

procedure: First of all the freshly prepared single crystal was placed onto the metallic basis plate. Afterwards the cell with the O-ring was fixed on top of the crystal by means of four screws and carefully checked for leaks. A platinum wire and a Ag/AgCl wire (Ø 0.5 mm) which served as counter and reference electrodes were mounted on the cell and fixed with Kel-F screws. The reference electrode was prepared by oxidizing a silver wire inside a 0.1 M aqueous HCl solution for approx. 3 minutes. 10 V were applied while graphite served as counter electrode. After assembling the cell the ionic liquid was filled into by means of an Eppendorf pipette inside a glove box (Plas Labs Inc.), flushed with nitrogen. For CV measurements typically 80 μL of the ionic liquid was injected. The electrochemical cell was put inside a plastic box which was flushed continuously with nitrogen during the CV measurements. Since it is an open cell, it was also used for *in-situ* STM studies and for immersion experiments. The CVs were recorded with a Zahner IM 6 from Zahner Elektrik controlled by the Thales Z 1.20 USB software and a Heka potentiostat-galvanostat PG 310 USB controlled by the Heka Potmaster software.

5.2 Impedance Cell

The impedance cell, also used for cyclic voltammetry, was a cylindrical cell of 0.3 cm^3 volume. The ends consisted of the Au(111) working and the gold sheet counter electrodes; the reference electrode, a straight wire, was placed halfway between the working and counter electrodes, parallel to them, across the cell (Fig. 5.2). This construction ensured the strictly homogeneous current density distribution along the working electrode surface which is an important condition for having reliable high-frequency impedance data with highly resistive electrolytes. A heating unit attached to the cell was continuously adjustable from room temperature up to 120 °C. All impedance experiments were performed under nitrogen atmosphere. The CV and the impedance measurements were recorded using a Zahner IM 6 from Zahner Elektrik controlled by the Thales Z 1.20 USB software and a home-made set-up based on an SR830 lock-in amplifier, a potentiostat and an AD/DA board with dedicated software for data acquisition and instrument control [126]. This set-up enabled impedance measurements between 100 kHz and 1 Hz. Accuracy of the impedance measurement has been tested by dummy cells having impedance spectra very similar to the studied electrodes.

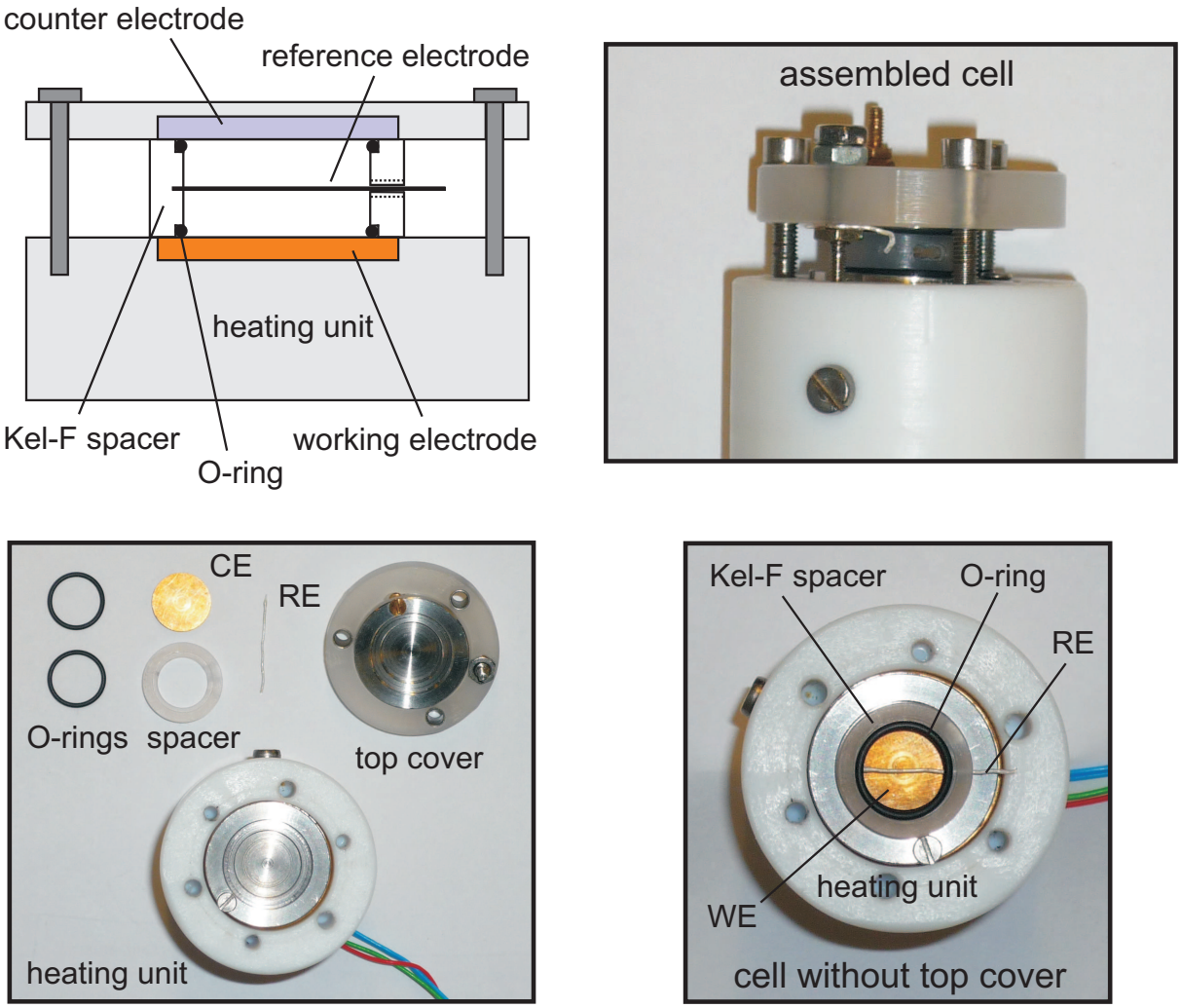

Figure 5.2: Cell used for electrochemical impedance spectroscopy.

6 *In-situ* STM Experiments

6.1 Experimental Setup

All STM experiments were performed wit a TMX 2010 from TopoMetrix. Control of the measurements was achieved by means of a personal computer connected to the STM base via the electronic controll unit (ECU). For the electrochemical measurements a bipotentiostat was used in order to control the potentials of tip and sample independently. Data analysis was carried out with the software Thermo Microscopes TopoMetrix SPMLab NT Ver.5.0. The scanner was a 1 μm tube scanner with a lateral scan range of 3 μm and a maximum Z-range of 1 μm. In all experiments the scanner was operated in the constant-current mode with 1 nA tip current. For vibration isolation the STM was mounted onto a heavy granite plate suspended from four steel springs [127–129]. The STM images in this work are all shown in grey scale. Thereby topographically higher areas are brighter than lower areas.

The STM cells were made of polytrifluoroethylene (Kel-F) which is a chemically inert and temperature-resistant material (Fig. 5.1). Assembling occured in the same way as for the electrochemical cell (see above). For STM measurements typically 80 μL of the ionic liquid were injected. During measurements the STM was flushed with nitrogen.

6.2 Tip Preparation

The quality of STM images is mainly influenced by the tip. Ideal STM tips have small tip radii, a good conductivity and mechanical stability. For electrochemical measurements the potential range in which the tip can be operated is an important criterion. In this work $Pt_{80}Ir_{20}$ tips were used which are known to have a fairly broad stability range in aqueous electrolytes (E_{SCE}= -0.2 V to 0.8 V in 0.1 M H_2SO_4). The $Pt_{80}Ir_{20}$ wire had a diameter of 0.25 mm. Preparation of STM tips occured in two steps: The etching and the insulation which are both described more detailed in the next two passages.

Small tip radii can be achieved by an electrochemical etching [130, 131]. For tip etching the experimental setup is shown in Fig. 6.1. The $Pt_{80}Ir_{20}$ wire was hold by means of an

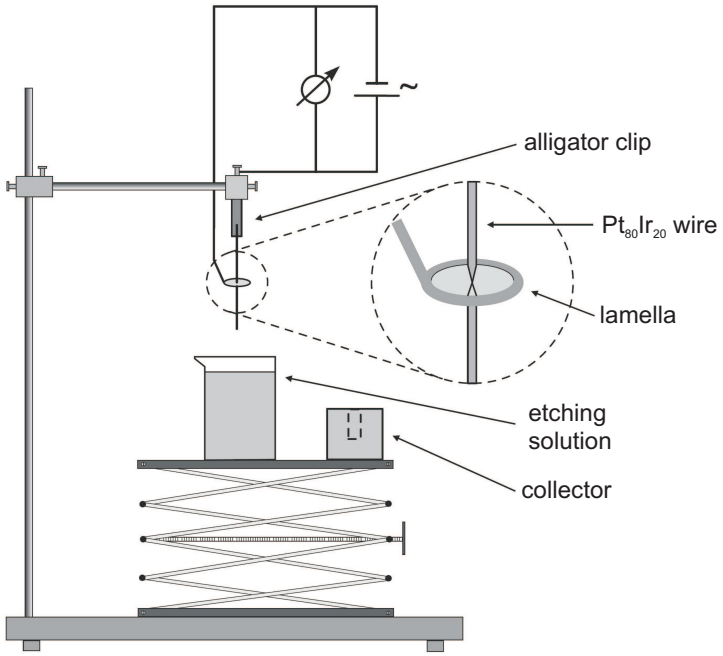

Figure 6.1: Experimental setup for tip etching [21].

alligator clip in the center of a platinum wire loop (Ø 10 mm). A lamella was formed inside the loop by dipping it into an etching solution (3.5 M aqueous NaCN solution). Applying an alternating current of 4.5 V electrochemical oxidation of the $Pt_{80}Ir_{20}$ wire occured within the contact region of the lamella. The lamella has to be renewed every two minutes in order to maintain a uniform etching and due to an enrichment of the platinum-cyanide complex within the electrolyte solution. After about 15 minutes the wire was etched and the tip was carefully collected with tweezers. Subsequently the tip was thoroughly rinsed with Milli Q-water in order to remove remaining cyanide solution. Before using them the tips were checked for possible damage with a light-optical microscope.

To avoid faradaic currents during measurements the tip was insulated by means of an electrophoretic paint from BASF (ZQ84-3225). The STM tips were dipped to circa 5 mm into the electrophoretic paint for approximately 3 minutes. Thereby a voltage (80 V, DC) was applied, a Pt sheet served as counter electrode. Afterwards the tip was placed into an oven for 10 minutes in order to polymerize the paint at 200 °C. By this procedure the paint shrank and broke up at the very end of the tip. During measurements a tunneling current was able to flow with leakage currents below 0.1 nA.

7 Electrode and Electrolyte Preparation

7.1 Annealing of Single Crystals

For all experiments Au(111) and Au(100) single crystals (MaTecK GmbH, Jülich, Germany) with a diameter of 12 mm and a height of 2 mm were used. Before each measurement the single crystals were placed onto a ceramic plate and flame annealed in an hydrogen flame for about 5 minutes [132, 133]. To avoid a melting the crystals had to be annealed with caution until a dark red glow was visible indicating a temperature just below the melting point of gold (1065 °C). In order to prevent a premature melting of the crystals the ceramic plate was shifted several times underneath the hydrogen flame. The flame annealing removed impurities on the surfaces and induced the $(\sqrt{3} \times 22)$ gold reconstruction on Au(111) and the (hex)-reconstruction on Au(100). After the annealing the crystals were allowed to cool down to room temperature in a nitrogen flow. Applying this procedure crystals with a very good surface quality were obtained. The surfaces showed wide terraces up to 500 nm.

Inductive heating was used in order to prepare single crystals under inert gas atmosphere. The gold crystals were annealed for 5 min with the inductive heating under nitrogen atmosphere according to the procedure described in literature [132, 134, 135].

7.2 Electropolishing

After each measurement the gold crystals were electropolished to make sure that all adsorbed species on the surface were removed. This procedure was particularly necessary after metal deposition to avoid surface alloying. Firstly, oxidation of the gold occured by dipping the crystal into an aqueous 0.1 M H_2SO_4 solution and applying a direct current of 10 V for about 5-10 s. Thereby, the gold crystal was connected to the anode whereas the counter electrode consisted of graphite. Subsequently, the reddish brown gold

oxide was removed by dipping the crystal into an aqueous 0.1 M HCl solution for about 5 minutes. Finally the crystal was thoroughly rinsed with Milli-Q water to remove remaining electrolyte solution. After electropolishing the crystals were stored overnight in an oven at 960 °C.

7.3 Ionic Liquid Purification

Commercial ionic liquids were purchased in the highest available (high purity) quality (water $\leq$ 100 ppm, halides $\leq$ 100 ppm) from Merck KGaA. Before use, the ionic liquid was vacuum-dried for 24 h at elevated temperatures (typically 80 °C) by means of a vacuum pump (Vacuubrand, 2×10^{-4} mbar) with a liquid nitrogen cooling trap. Afterwards molecular sieve was added to the liquid in order to remove impurities from the synthesis as well as residual water. The molecular sieve, bead-type and without moisture indicator, was also purchased from Merck KGaA. The commonly available pore size of 0.3 nm (order nr. 1.05704.0250) was used. The molecular sieve was boiled in ultra pure water for 3 h in order to clean it from fine grained dust; water exchange was carried out every 30 minutes. Subsequently the molecular sieve was dried in an oven at 200 °C for 7 days before use. After adding it to the ionic liquid (typically 15 beads to 1 ml, IL), vacuum was applied for 24 h at 80 °C. Afterwards the liquid together with the molecular sieve was kept under nitrogen atmosphere at room temperature. Before using the liquid, vacuum was again applied for 24 h at 80 °C, to the stock solution. Detailed studies concerning purification of ILs are given in chapter 10.

7.4 Reference Electrodes in Ionic Liquids

Most of the conventional reference electrodes used in aqueous solutions cannot be directly used in ionic liquids and there is no universal rule either about using reference electrodes. Pt and Ag wires are commonly used metal quasi-reference electrodes in ionic liquids. In the absence of redox couples in the solution, the potential of such a type of quasi-reference electrode is determined by the interfacial potential between metal and electrolyte, which may be easily affected by the changes of the composition of electrolyte. In practice, however, the metal quasi-reference electrode is found to be stable enough in a given experiment in the neat ionic liquid under inert gas protection, but may vary from experiment to experiment by up to a couple of hundred millivolts.

8 Materials and Chemicals

The water used for the experiments (tip preparation, electropolishing) was high purity water which was additionally purified with a water purification system (Sartorius arium 611). The specific resistance was 18.2 MΩcm and the amount of organic impurities (total organic carbon) was below 3 ppm. Only chemicals with the highest purity available were used in this work.

Formula	Company	Purity
$PdCl_2$	Sigma-Aldrich	99.999%
NaCN	Fluka	puriss. p.a., >97%
H_2SO_4	Merck KGaA, Darmstadt, Germany	96% suprapur
HCl	Merck KGaA, Darmstadt, Germany	30% suprapur

Table 8.1: Chemicals for electrolyte solutions

Molecular Formula	Company	Purity
H_2	MTI IndustrieGase AG, Neu-Ulm, Germany	5.0
N_2	MTI IndustrieGase AG, Neu-Ulm, Germany	5.0
Ar	MTI IndustrieGase AG, Neu-Ulm, Germany	5.0

Table 8.2: Gases

Ionic Liquid	Company	Purity
$BMIPF_6$	Merck KGaA, Darmstadt, Germany	high purity (water $\leq$ 100 ppm, halides $\leq$ 100 ppm)
$BMITf_2N$	Merck KGaA, Darmstadt, Germany	high purity (water $\leq$ 100 ppm, halides $\leq$ 100 ppm)

Table 8.3: Commercially available ionic liquids

Material	Company	Usage
Kel-F	Heute & Comp, Radevormwald	cell material
Kalrez	DuPont Dow Elastomeres, USA	O-rings
Gold single crystals, purity: 99.999%	MaTecK GmbH, Jülich, Germany	working electrodes
$Pt_{80}Ir_{20}$, purity: 99.99%	MaTecK GmbH, Jülich, Germany	STM tips
Platinum wire, purity: 99.995%	Götze, Berlin	counter and reference electrodes
Silver wire, purity: 99.99%	MaTecK GmbH, Jülich, Germany	reference electrodes
Gold sheet, purity: 99.9%	MaTecK GmbH, Jülich, Germany	counter electrodes
Electrophoretic paint ZQ84-3225	BASF AG, Ludwigshafen	STM tip coating
Molecular sieve, bead type, pore size: 0.3 nm	Merck KGaA, Darmstadt, Germany	ionic liquid purification

Table 8.4: Materials

Part III

Results

9 Au(111) in $BMIPF_6$

[1]In many instances of ILs cyclic voltammograms (CV) on various electrodes are presented that show a flat, „double layer"-type behaviour over a range of 4 V and more. These were recorded at a rather insensitive current scale with the aim of demonstrating the broad potential range without faradaic reactions. Employing conditions normally used for studies in aqueous solutions, the CVs of ILs are anything but flat. This is demonstrated in Fig. 9.1: Fig. 9.1a shows a 10 mV/s CV for Au(111) in $BMIPF_6$ at a usual, insensitive current scale, and also the middle part with higher resolution. This middle part of about 1.5 V represents a potential window within which the current seems to be non-faradaic in nature, hence might be considered as double layer charging/adsorption region. This part of the voltammogram is reproducible (at least for an hour or so) provided the potential was kept within this range: If these limits are passed, irreproducible additional humps appear in the CVs (Fig. 9.1b). Accordingly, the impedance studies were done within the above limits. Peak P (Fig. 9.1a) is a well-defined feature of the voltammogram; taking into account that this peak shifts with scan rate, even at values as low as 2 mV/s (cf. inset of Fig. 9.1b), voltammograms measured with different reference (or quasi-reference) electrodes could be compared based on P's location, E_P, at identical scan rates, e.g. at 50 mV/s. With this scan rate, $E_{P,50}$= -0.3V vs. Ag/AgCl.

Impedance spectra in the full -0.9 to +0.7 V range can be well modelled by the equivalent circuit shown as inset of Fig. 9.2a. At the high frequency end of the spectrum the dominant elements are the series resistance, R_s and the capacitance, C_{hf}, whereas at lower frequencies the contribution of the constant phase element (CPE) is dominant. This latter element is defined by its admittance as $Y_{\mathrm{CPE}}(\omega) = Q(i\omega)^n$ where Q and $0 < n < 1$ are the CPE coefficient and CPE exponent, respectively. The spectra, plotted in the capacitance representation, are shown in Fig. 9.2b, whereas the potential dependence of C_{hf} and the CPE parameters are shown in Fig. 9.3 (the series resistance, trivially having no potential dependence, corresponds to the literature value of $BMIPF_6$ conductivity (0.13 S/m [136], 0.146 S/m [55]). On one hand, the capacitance C_{hf} shows little if any potential dependence

[1] Reprinted from „The interface between Au(111) and an ionic liquid", M. Gnahm, T. Pajkossy, D. M. Kolb, *Electrochim. Acta* **55** 6212–6217, Copyright (2010), with permission from Elsevier.

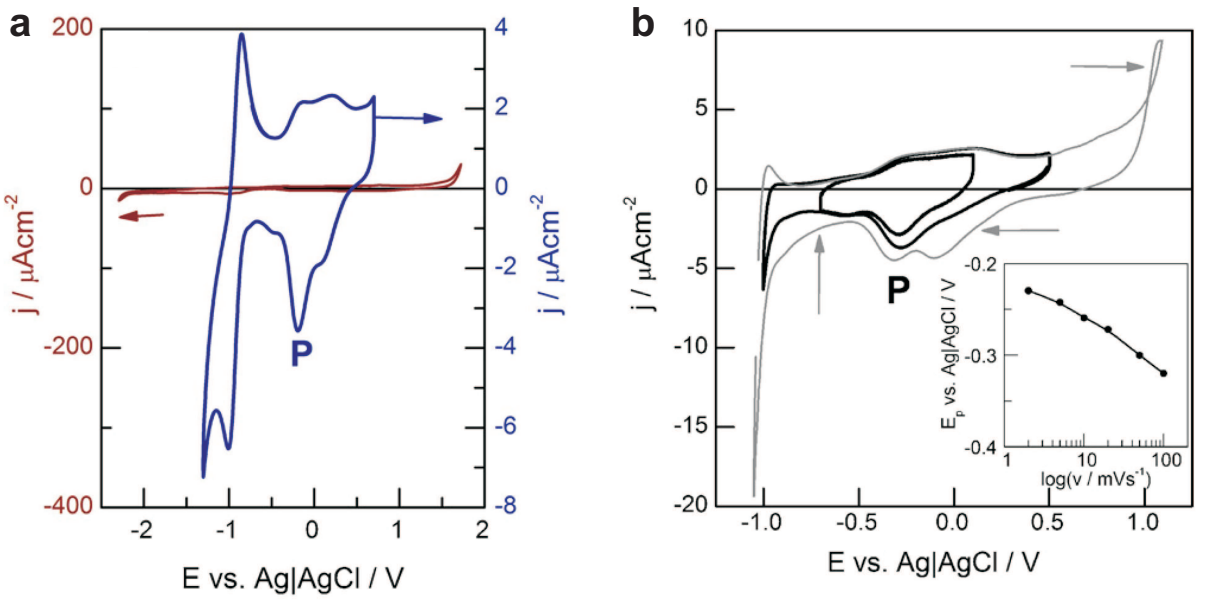

Figure 9.1: (a) CV of Au(111) in $BMIPF_6$ recorded at 10 mV/s with two current scales. The „flat“ CV within the ±2 V polarization range of the $BMIPF_6$ appears structured when the ≈ ±1 V region is measured at higher current sensitivity. (b) CVs at 50 mV/s scan rate for various potential limits. Arrows indicate the irreproducible additional humps when the positive limit exceeds +1 V. Inset: Scan rate dependence of the potential of peak P, E_P.

(Fig. 9.3, crosses), its value is about 6-7 $\mu F/cm^2$; on the other hand, the CPE coefficient exhibits a peak around -0.3 V; whereas the CPE exponent shows some – although rather scattered – potential dependence.

A quantity of fundamental importance certainly is the potential of zero charge, pzc, for Au(111) in contact with the IL. Its determination is by no means trivial, as the common approach for determining pzc's (pzfc, potential of zero free charge, to be precise) in aqueous solutions, i.e., the search for a Gouy-Chapman minimum in the capacitance, is not applicable to room temperature melts. In addition, as the above impedance measurements reveal, there is no potential-dependent capacitance present; thus the related theories [12, 13] have no relevance here. The so-called immersion technique was chosen to get an idea about the pztc, the potential of zero *total* charge. By this method, a freshly prepared electrode is quickly immersed into the solution at a pre-set potential and the charge flow for establishing the double layer is measured [137]. The pztc is then spotted by the sign change of the charging current. In the present case the Au(111) crystal after flame annealing was mounted in the Kel-F cell, connected to an operating potentiostat; then the IL was injected with the help of an Eppendorf pipette to quickly cover the whole electrode surface, making sure that the liquid first established contact with the

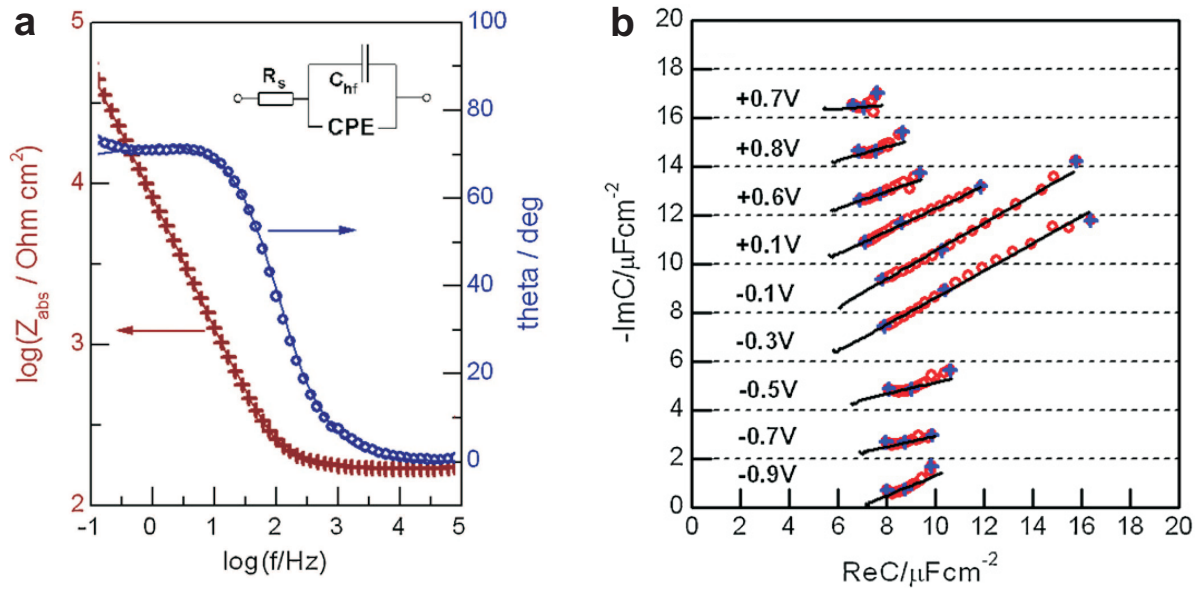

Figure 9.2: (a) Impedance spectrum, $Z(\omega)$, measured at E = -0.2 V vs. Ag/AgCl. Solid lines are the fitted spectrum, calculated by the equivalent circuit of the inset. For the meaning of its elements, see text. (b) Impedance spectra at potentials (vs. Ag/AgCl) indicated, in capacitance representation, i.e. by plotting $C(\omega) = 1/i\omega(Z(\omega) - R_s)$, where R_s is the series resistance determined by fitting. On the capacitance plots the 100 Hz, 10 Hz, and 1 Hz points are indicated by crosses; solid lines are the fitted curves using the equivalent circuit of (a) inset. The spectra are shifted along the ordinate for visibility reasons.

reference and counter electrodes before hitting the working electrode. The wetting procedure required roughly 5 s, the current transient being recorded over several minutes. The charge is obtained by integration (Fig. 9.4a). Note that in contrast to measurements in aqueous solutions when the current decays exponentially to zero, here the transients are power-law-like rather than exponential with time and consequently, the charge, i.e. the integrated current depends on the duration of the experiment. Charges calculated with 100 s integration time are seen as function of immersion potential in Fig. 9.4b. The zero-crossing is around -0.1 V vs. Ag/AgCl; the slope of the tilted line is around 130 μF/cm^2; which is in a reasonably good agreement with the figure obtained if a CPE charging is considered[2].

Now the question arises, whether the complicated CV can be attributed solely to the IL, or does the Au surface property also change with potential. *In-situ* STM images suggest the latter to be the case. The freshly prepared Au(111) – i.e. with a reconstructed

[2] If the charging of a CPE by voltage u is started at time zero, its charge, q, varies in time as $q(t) = uQt^{1-n}/\Gamma(2-n)$ where Γ is the gamma-function. Taking the CPE values at its peak (see Fig. 9.3), that is, $Q = 25\ \mu F s^{0.7-1}$ and $n = 0.7$, we obtain $q/u = 25\ \mu F \times 100^{0.3}/\Gamma(1.3) = 111\ \mu F$.

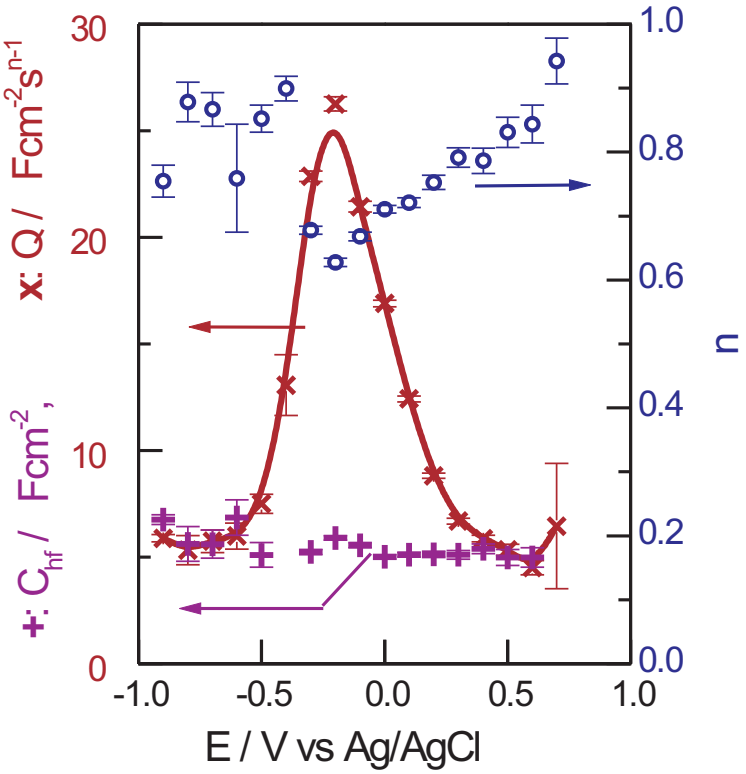

Figure 9.3: The fitted equivalent circuit parameters, as function of potential. C_{hf} (+), Q (×), and n (∘) data obtained from fitting of the spectra of Fig. 9.2. Note that C_{hf} and Q are of different dimensions.

surface due to flame annealing [138] – was usually immersed at +0.2 V vs. Ag/AgCl, the corresponding STM image being given in Fig. 9.5a. No sign of the gold surface property is seen such as monoatomic high steps or islands (the blurred image of a surface littered by holes suggests a layered structure of the IL). Stepping the potential to values considerably negative (-0.5 V, Fig. 9.5b) makes the holes to disappear and monoatomic high islands appear, very much like those islands caused by lifting of the reconstruction. The overall impression of the STM image is greatly enhanced in clarity. In addition, the structure change between -0.5 and +0.2 V vs. Ag/AgCl is instantaneous (at least on the time-scale of the STMs line scan, Fig. 9.5b) and reversible.

At more negative potentials high resolution STM images could be obtained showing a worm-like structure (Fig. 9.6a) [139]. This structure is probably caused by an adsorption of the $[BMI]^+$ cations. The STM image suggests a stacking of numerous layers which can

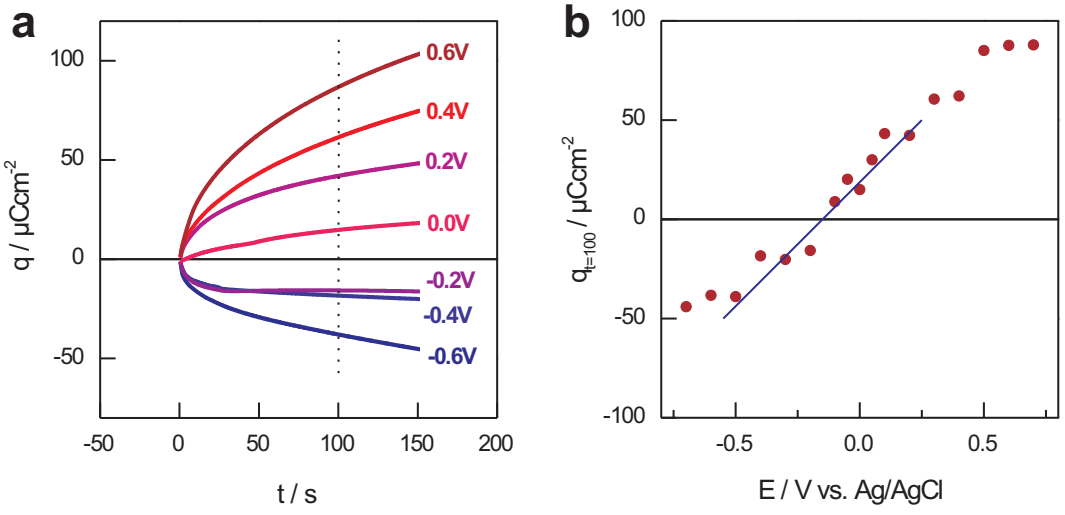

Figure 9.4: (a) Integrated immersion transients at potentials indicated and (b) the charge calculated for 100 s as function of potential.

be explained by π–π interactions between the aromatic ring systems of the imidazolium cation. Recent AFM investigations also demonstrated multilayer formation in front of the electrode surface [140,141]. A smaller scan range reveals the fine structure with a random arrangement of molecules (bright spots), which do not follow the hexagonal symmetry of the underlying substrate (Fig. 9.6b). The structure reflects a certain mismatch between surface and adsorbed molecules. Obviously the Au(111) substrate is unsuitable for the formation of an ordered adlayer, in contradiction to Au(100) in $BMIPF_6$ (see below). Decreasing the potential to values beyond the stability range of the ionic liquid the worm-like structure disappears and a smooth surface can be seen covered with holes of 0.3 nm $\pm$ 0.05 nm depth (Fig. 9.6c). The disappearance of the ad-structure might be interpreted with a reductive desorption of the cations at negative potentials. The well-known herringbone reconstruction rows are faintly visible between the holes (Fig. 9.6d). It seems that a reconstructed Au(111) surface is lying underneath the adsorbed layers, although its formation is still debatable. The worm-like structure also disappears returning to more positive potentials (Fig. 9.7a). The dissolution occurs due to electrostatic forces repelling the cations from the electrode surface upon anodic excursion. This process is rather slow compared to the reductive desorption. The image becomes blurred after about 30 minutes (Fig. 9.7b).

9.1 Discussion

The main findings in the potential range of -0.9 V to +0.7 V vs. Ag/AgCl, that is, -0.6 V to +1 V vs. $E_{P,50}$ are as follows:

- The impedance spectra can be well-modelled by an equivalent circuit where the elements due to the interface are the parallely connected C_{hf} and a CPE.
- C_{hf} and the CPE exponent show little if any potential dependence, the CPE coefficient shows a marked peak at $E \approx E_{P,50} + 0.1$ V.
- Immersion experiments show that the pztc is also somewhere at $E \approx E_{P,50} + 0.2$ V.
- STM images show structure changes to occur around $E_{P,50}$.

It is very difficult to compare these results with the ones of the literature. Two theoretical [12, 13] and four experimental [143–146] articles were found dealing with double layer capacitance – impedance – pztc issues which are relevant for electrodes in ILs. However, the theoretical papers derive capacitance–potential curves without the mentioning of the dynamics of the double layer rearrangements expressed by the existence of the CPE. The subject of the experimental articles differ from the present study in three respects:

(a) Apart from Hg used in studies of Refs. [143, 145, 147] – having a well-defined clean surface, the electrode materials (carbon [143], glassy carbon [143,147], gold [143] and platinum [147]) are polycrystalline. On the basis of aqueous electrochemistry experience, interfacial studies with single crystals of well-defined surfaces yield better-defined results than polycrystalline ones.

(b) The high frequency end of the impedance spectra is always very sensitive to cell geometry. If the solution resistance is smaller for the electrode edge than for the middle, then the high-frequency behaviour, for example, of a capacitive electrode is not that of a series RC, but an ill-defined mixture of the middle part's RC and of the edges' RC. As a rule of thumb, the AC-Wagner number [148] can be applied for calculating the critical frequency: The $l\rho\varepsilon\omega \ll 1$ condition (where the symbols stand for the size of the electrode, specific resistivity of the electrolyte, specific capacitance of the surface and angular frequency, in sequence) should hold if the edge effects are negligibly small. For the typical case of an disk electrode of radius 10^{-1} cm, with $\varepsilon = 10^{-5}$ F/cm^2, $\rho = 10^3$ Ωcm, $\omega = 10^3$ s^{-1}; that is, above 100 Hz the impedance spectra are distorted. For a detailed analysis of this situation, see [149]. This is why

the cell was constructed with a strictly homogeneous current density distribution; and it is suspected that for this reason the C_{hf} element is missing in the equivalent circuits of the above articles.

(c) In principle, calculating capacitances from CPEs is impossible, because the two quantities have different dimensions. Still, this is a widely used practice on the expense of introducing an arbitrary factor of the capacitance (for ways of doing the dimension-adjustment see section 2.1 of Ref. [146]). However, due to the ill-defined nature of the capacitance measured at a single frequency – or calculated from impedance spectra based on CPE-containing models – any comparison is questionable, perhaps even the locations of the extrema.

The measurements are interpreted as follows: First, the three potentials – the potential of peak P, of the CPE coefficient maximum, and of the zero-crossing of the immersion charge – are the same; the apparent differences being due to different „effective scan rates“. The close potential values for P and the $Q(E)$ maximum is not surprising: If the impedance response of a system is that of a capacitance or a CPE with a peaky potential dependence, then the CV will also contain a peak. The main question is, where is the CPE peak coming from. This peak is rationalized due to the complete reorientation of the double layer: This is the potential, where the innermost ion layer changes its polarity. Negative and positive to the peak the $[BMI]^+$ cations and the $[PF_6]^-$ anions dominate the Helmholtz-layer, respectively; concommitantly the pztc is at the peak.

Secondly, the CPE plays the role of the double layer capacitance, however, the rearrangement of the double layer is much slower than in the case of aqueous electrolytes. This is again not surprising: The IL is not a simple molecular liquid; charges are linked to each other, complete domains are reorganized for any electric field change. Sluggish processes manifest themselves also in high viscosity and low ionic mobilities.

Third, C_{hf} is 6–7 $\mu F/cm^2$, independent of the potential, on both sides of the pztc. This is rather surprising, and from theorizing this finding is refrained. All what can be said is that the average location of the anions and cations do not differ much at the two sides of the pztc.

Fourth, the STM images negative and positive of $E_{P,50}$ are vastly different. Only at negative potentials the gold surface seems to be imaged, as the monoatomic high gold islands are clearly visible, which are characteristic of unreconstructed Au(111). At positive potentials the electrode surface appears to be covered by a thick layer of IL, leading to a blurred image, often found with organic surfaces.

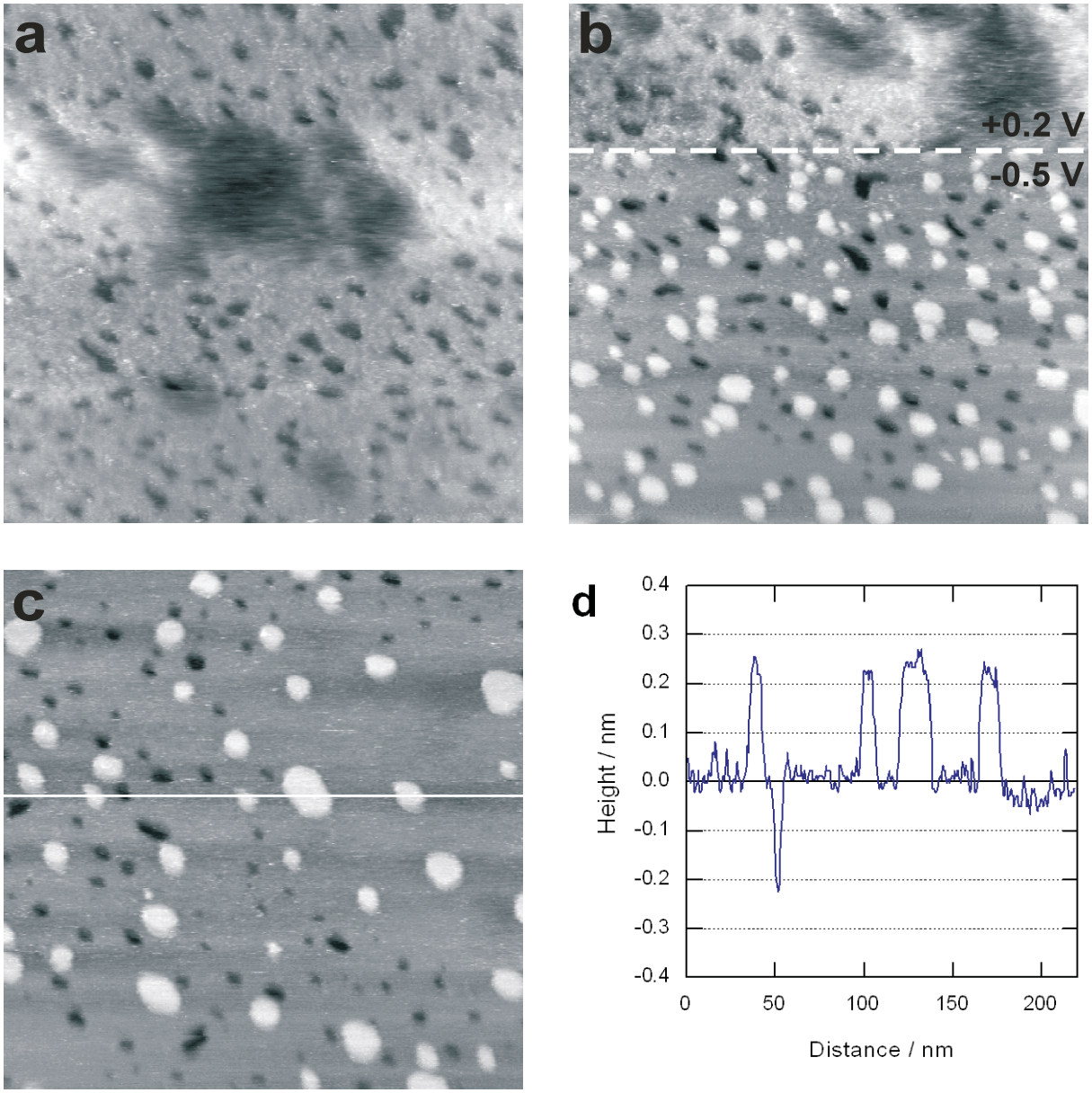

Figure 9.5: STM images (230 nm × 230 nm) of the Au(111) surface recorded at +0.2 V (a) and -0.5 V (c). In image (b) the potential was stepped from +0.2 V to -0.5 V. (d) Height profile along the line in image (c).

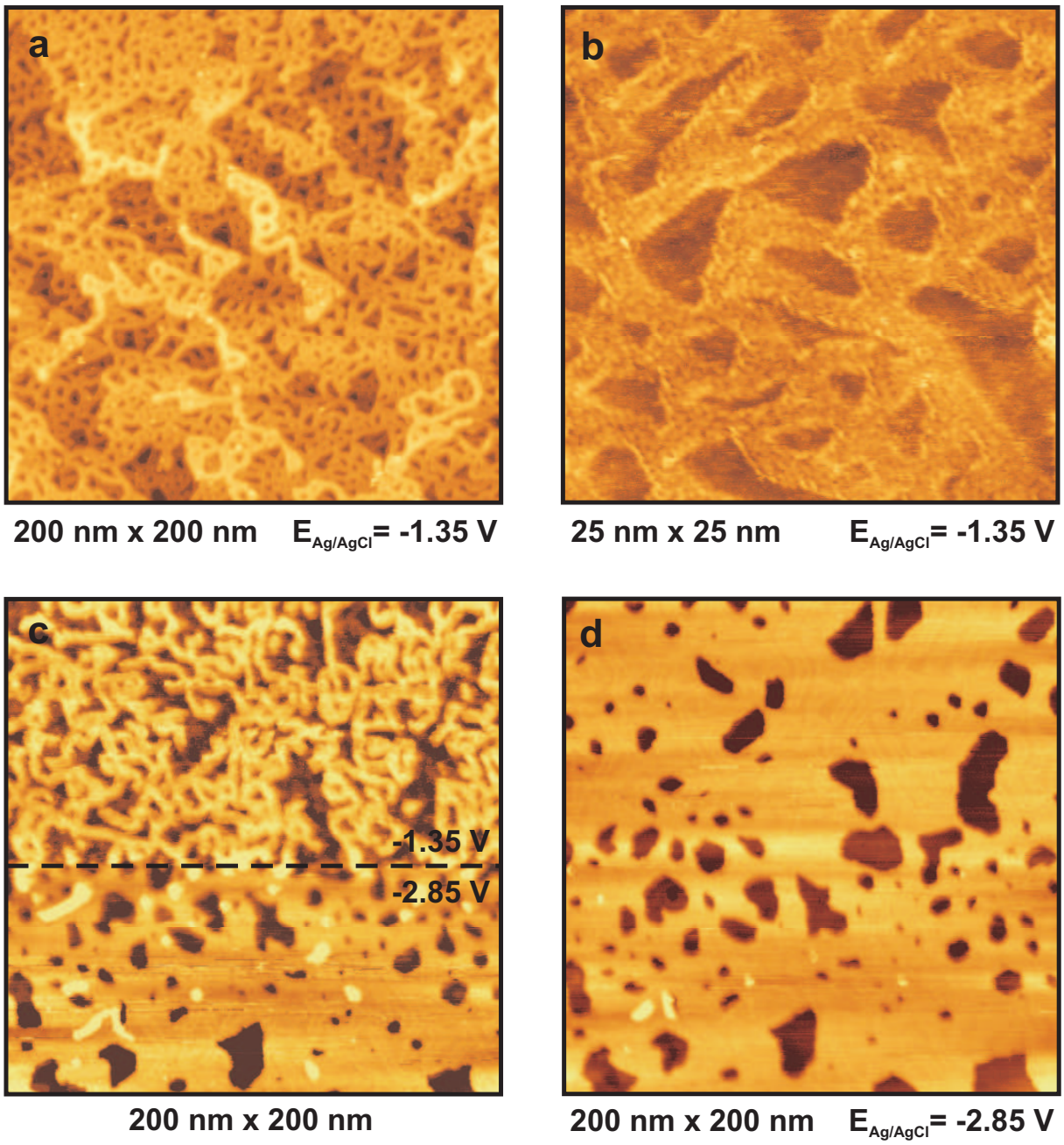

Figure 9.6: STM images of Au(111) in $BMIPF_6$ at negative electrode potentials [142].

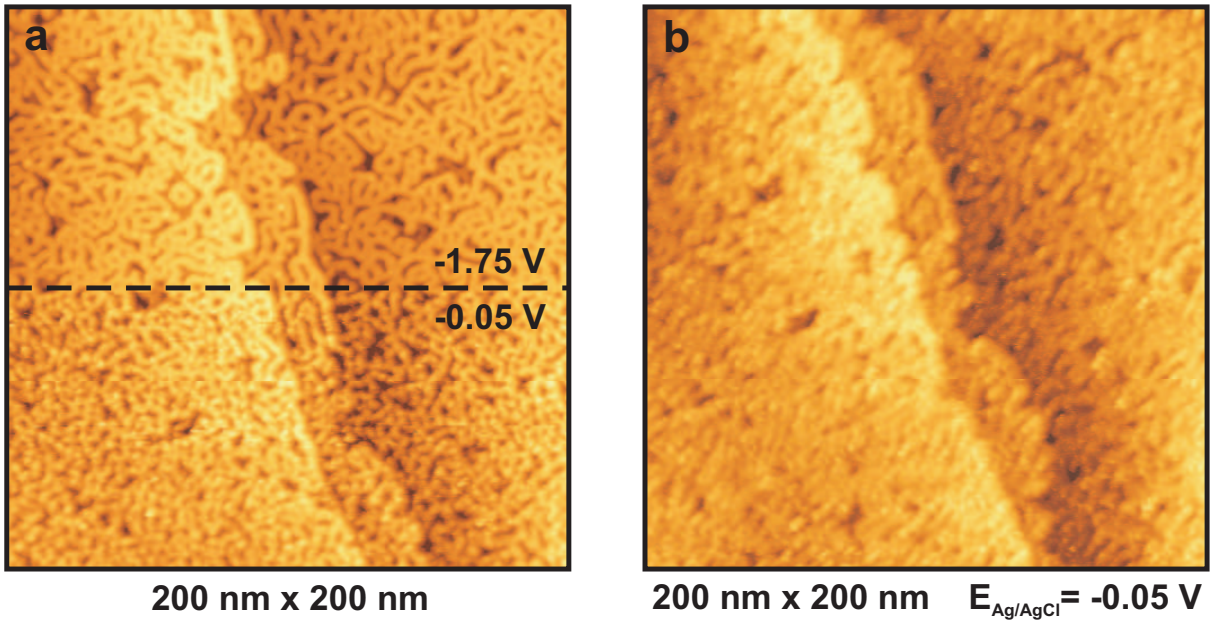

Figure 9.7: Au(111) in $BMIPF_6$: (a) The potential was stepped from -1.75 V to -0.05 V, (b) was recorded 30 minutes later [142].

10 Purification of Ionic Liquids

[1]Ionic liquids (ILs) or room temperature molten salts are increasingly used in electrochemistry, mainly because of their wide stability window of typically 3–4 V [2, 45, 139, 150–152]. This makes them very attractive for electrodeposition studies, particularly with unnoble and reactive metals. Although modern ILs like 1-butyl-3-methylimidazolium hexafluorophosphate ($BMIPF_6$) are essentially air- and water-stable and hence, relatively easy to handle, purification of commercial products is still required for fundamental investigations. ILs, for example, can absorb a considerable amount of water which results in a change of the physical properties of the liquid such as diffusion coefficients therein [153]. Furthermore there is evidence of the formation of HF, a corrosive and toxic gas, if $[PF_6]^-$-based ionic liquids get in contact with water [31]. One can also find inorganic impurities, mainly Li^+ and K^+, from synthesis. Some of the commercially available ILs which should be colourless like $BMIPF_6$, show a light yellowish discoloration. Since distillation of ILs is difficult due to their low vapour pressure [40] , established purification methods comprise charcoal and alumina/silica columns [154, 155]. Sweeny and Peters reported on the use of molecular sieves for IL purification, obviously with great success [156]. A dominant feature in their voltammogram, which they ascribed to water, was completely removed. In this chapter a treatment is described, which helps to substantially reduce the level of impurities, the most dominant one being water. It is demonstrated that the use of a molecular sieve with the right pore size can remove undesirable species.

In many studies of ionic liquids, cyclic voltammograms pretend a double layer region over a range of 4 V and more. However, these curves were usually shown in a rather insensitive current scale, whereas high resolution CVs with a current scale in the μA range clearly reveal the presence of faradaic reactions (chapter 9). Fig. 10.1 shows two cyclic voltammograms for Au(111) in contact with $BMIPF_6$, which demonstrate the effect of cleaning with the proper molecular sieve: The dashed curve represents a CV for $BMIPF_6$ as purchased from Merck KGaA in high-purity quality, the liquid being vacuum-dried over night at 80 °C to remove residual water. A marked increase in the negative current

[1] Reprinted from „The purification of an ionic liquid“, Markus Gnahm, Dieter M. Kolb, *J. Electroanal. Chem.* **651** 250-252, Copyright (2011), with permission from Elsevier.

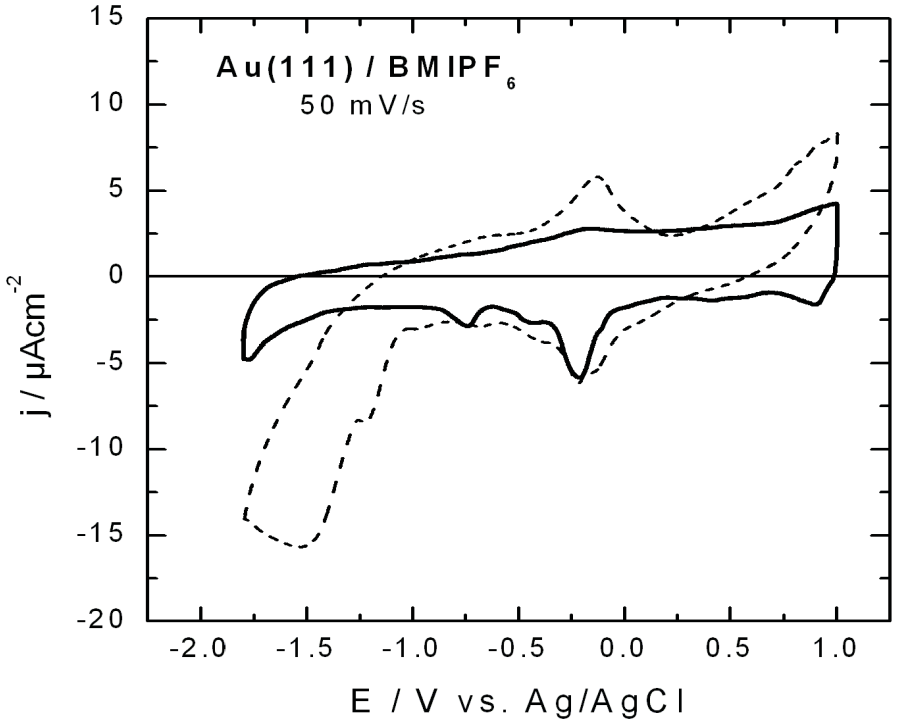

Figure 10.1: Cyclic voltammograms recorded at 50 mV/s for Au(111) in contact with $BMIPF_6$. Dashed curve: With vacuum-dried ionic liquid from Merck. Bold curve: After having added molecular sieve with 0.3 nm pore size during preparation of the IL. All potentials with respect to the Ag/AgCl pseudo-reference electrode.

density at around -1.0 V is observed, which is attributed to the reduction of impurities in the ionic liquid, and it is assumed that it's either residual water or lithium originating from the synthesis of the IL. Imidazolium-based ionic liquids of this type are normally synthesised by a methathesis reaction: The alkylation of the methylimidazolium base with 1-chlorobutane is followed by an anion exchange with lithium-hexafluorophosphate to form lithium chloride [7, 45, 157]. Endres *et al.* also reported lithium impurities and the difficulties of removing them [158]. Residual water cannot be excluded in the liquid as source, although the $BMIPF_6$ was dried under vacuum over night at elevated temperatures. The anodic current at the positive limit of the potential scan could be due to halide impurities, presumably chloride. It was found that after adding molecular sieves of a certain pore size the faradaic currents on both sides of the potential window had disappeared almost completely. It should be mentioned that in this case the gold crystal was annealed by means of an induction coil under nitrogen atmosphere rather than by flame annealing. This preparation technique in addition helps to obtain reproducible CVs,

e.g. by removing small cathodic currents negative of -0.75 V which are assigned to trace amounts of water adsorbed on the gold surface. Interestingly the cathodic peak at -0.25 V is not markedly affected by such treatments, like a molecular sieve. This is further evidence that this peak is related to a specific interaction between the gold substrate and the ionic liquid rather than caused by impurities. The observation of this peak is reported in chapter 9 and attributed to a rearrangement of the IL side of the double layer, as it occurs close to the potential of zero charge.

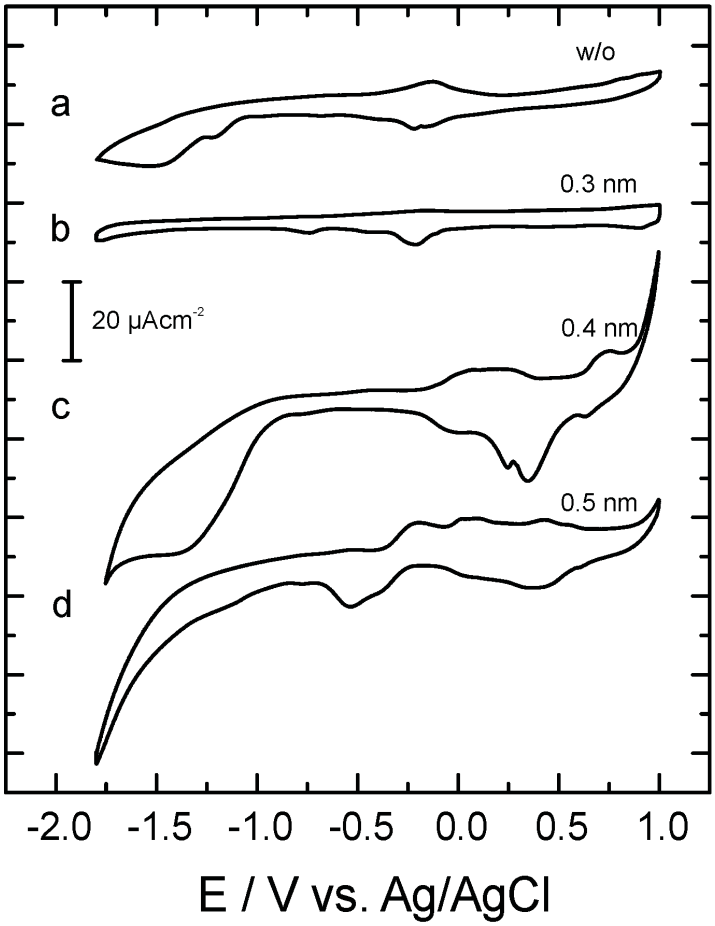

Figure 10.2: Cyclic voltammograms for Au(111) in $BMIPF_6$, showing the effect of molecular sieves of different pore sizes. Scan rate: 50 mV/s. Potentials are given with respect to a Ag/AgCl pseudo-reference electrode. (a) Ionic liquid as purchased from Merck KGaA in highest available quality (high purity), and dried over night under vacuum at 80 °C. No molecular sieves. (b) Adding molecular sieve with 0.3 nm pore size. Curves (c) and (d) are with molecular sieve of 0.4 nm and 0.5 nm pore size, respectively.

In the search for optimum purification conditions, molecular sieves of different pore sizes were tested (Fig. 10.2). Curve (a) represents the CV for $BMIPF_6$ without molecular sieve. The IL was only vacuum-dried over night at 80 °C to remove residual water. Features

at -0.2 V and the onset of a reduction process at -1.1 V are observed. After adding a molecular sieve with 0.3 nm pore size most of these features have disappeared (curve b), with the cathodic peak at -0.2 V still existing (see also Fig. 10.1). The corresponding anodic peak has flattened out. A small cathodic peak at -0.75 V is now much better visible as compared to curve (a). Curve (b) displays a rather flat double layer region, especially at the negative part, with a capacitance of about 30 μFcm^{-2} calculated from the CV. Addition of molecular sieve with 0.4 nm pore size (c) causes dramatic effects. Large faradaic currents are seen, which point towards a severe contamination by the molecular sieve. Furthermore a strong yellow discoloration of the $BMIPF_6$ is observed after adding 0.4 nm molecular sieve, which does not occur with the 0.3 nm sieve. Curve (d) demonstrates the impact of adding a molecular sieve of 0.5 nm pore size. In contrast to the 0.4 nm molecular sieve, the liquid has not changed colour. Nevertheless it is obvious from inspection of curve (d), that the 0.5 nm molecular sieve also introduces impurities and hence, is not recommended for use.

Finally, the time dependence of a CV for the 0.3 nm sieve was studied in order to have some ideas about purification rates (Fig. 10.3). Curve (a) represents the $BMIPF_6$ without molecular sieve. The liquid was only dried over night by means of a vacuum pump at 80 °C (see Fig. 10.1). Adding a molecular sieve with 0.3 nm pore size leads within 2 h to a clear variation of the CV. Most conspicuous the prominent reduction current at -1.5 V decreases in size (curve b). After 4 h most of the reduction current has disappeared while the peak at -0.25 V still looks dubious (curve c). After 72 h with molecular sieve the reduction at -1.5 V has completely gone, and only the IL-characteristic peaks are left.

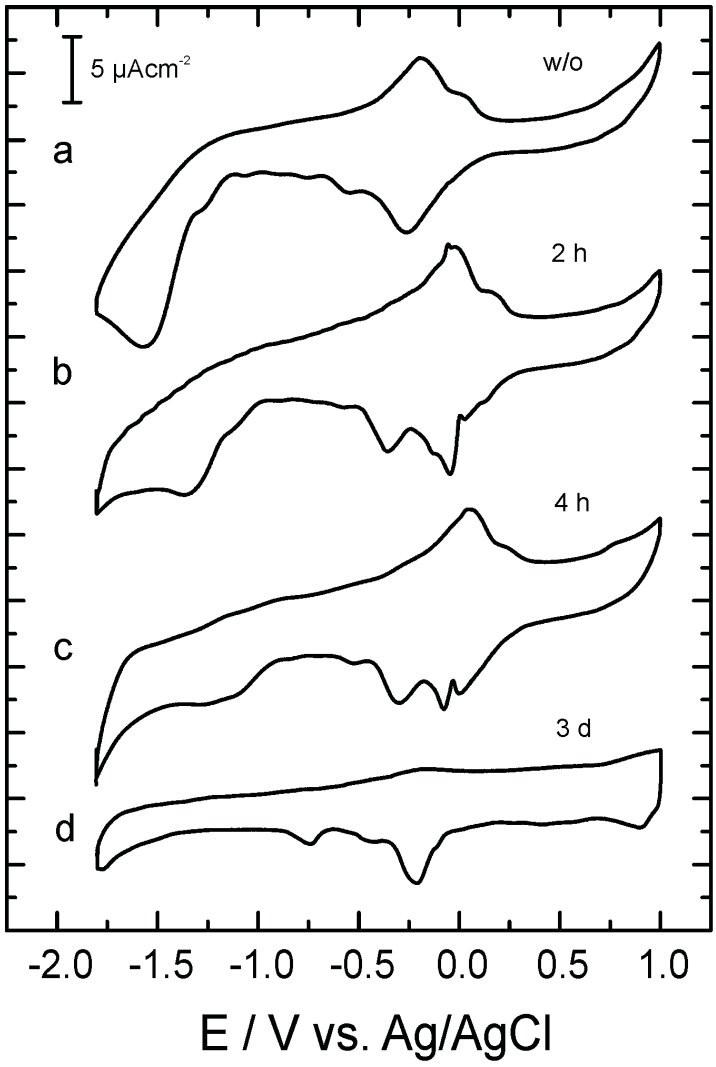

Figure 10.3: Cyclic voltammograms recorded at 50 mV/s for Au(111) in $BMIPF_6$ containing molecular sieve of 0.3 nm pore size showing the time-evolution of the purification process. Curve (a) was obtained without adding molecular sieve to the ionic liquid. It was only dried over night under vacuum (2×10^{-4} mbar) at 80 °C. (b) recorded 2 h and (c) 4 h after adding molecular sieve. Curve (d) was recorded after 3 days. Potentials are given with respect to a Ag/AgCl pseudo-reference electrode.

11 Au(100) in $BMIPF_6$

11.1 Cyclic Voltammetry

[1]Fig. 11.1 shows the CV of a Au(100) electrode in contact with $BMIPF_6$. Significant cathodic and anodic faradic currents occur beyond -1.5 V and +0.8 V, respectively, so unless otherwise noted (see the section on STM studies) these potentials were chosen as limits in order to avoid the faradaic process that occurs out of this potential range; within these limits continuous cycling yields reproducible CVs even after 24 h (thin curve). The high resolution CV reveals a fine structure with noticeable cathodic peaks, the most prominent one, P_1, appearing at -250 mV with a flat shoulder at around -500 mV. A second cathodic peak, P_2, is seen at -800 mV, a third one – P_3, often hardly discernible – at +0.6 V. All peaks have flat anodic counterparts at about the same potential. It was found that the surface quality of the gold crystal has a marked influence on the visibility of the anodic peaks. In this case the (newly acquired) gold crystal was annealed in an oven at 960 °C for several months prior to the measurement. Furthermore, the purification of the IL by the molecular sieve adds also significantly to the visibility of the peak structure by background suppression of the CV. A smooth double layer charging region is seen negative of the peak at -800 mV until around -1.8 V decomposition of the ionic liquid starts.

The CV for Au(100) is very similar to that for Au(111) with the two most pronounced cathodic peaks at -0.25 and -0.8 V for Au(100) occurring at almost identical values for Au(111) (see Fig. 10.1). However, the average double layer charging current appears to be significantly lower, by a factor of two, in the case of Au(100) as compared to Au(111). The characteristic peaks in the CV obviously are determined by the IL properties rather than by the substrate's crystallographic surface orientation. As will be demonstrated below by *in-situ* STM, the peak potentials indeed coincide with structure changes of the IL near the electrode surface.

Passing the -1.8 V negative potential limit causes irreversible changes: The large catho-

[1]Reproduced by permission of the PCCP Owner Societies, www.rsc.org/pccp.

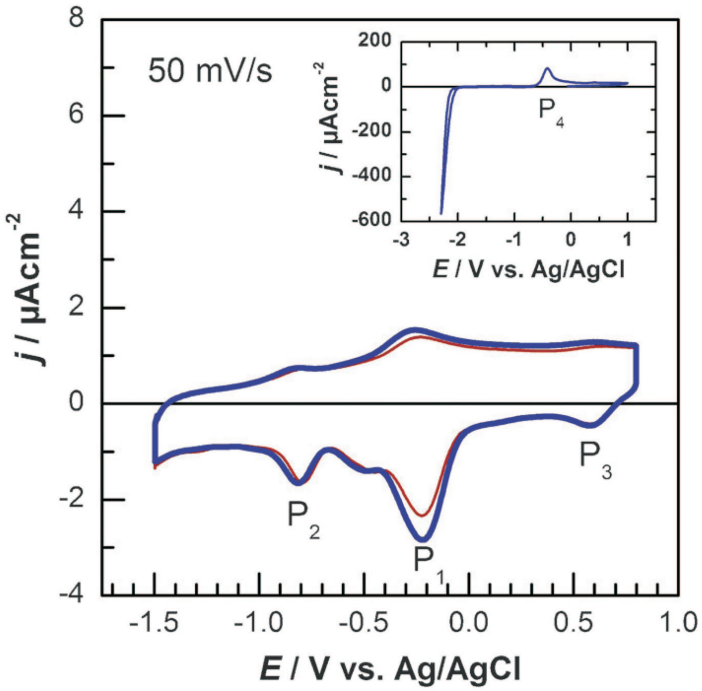

Figure 11.1: CVs of $\nu = 50$ mVs^{-1} scanrate for the Au(100)/BMIPF$_6$ system. Thick and thin curves are the CVs just after filling the cell and 24 hours afterwards, respectively. The inset shows the onset of the cation's reduction („cation breakdown") at around -2 V. The DC-capacitance, calculated as j/ν, is in the order of magnitude of 20–30 μFcm^{-2}; at peak P$_1$ $\sim$ 50 μFcm^{-2}. Pronounced cathodic humps occur at -250 mV and -750 mV, respectively.

dic current signals the reduction of the [BMI]$^+$ cation (see inset of Fig. 11.1). A plausible mechanism suggests the generation of radicals that react with each other to form dimers [159]. In a subsequent positive potential scan a large anodic current peak, P$_4$, at -0.4 V indicates the reoxidation of the reduced species. In addition, the peak structure due to double layer charging has been destroyed.

Attention to two regions is focused: One is the region at and around the peak P$_1$ (-0.6 to +0.5 V), since – as it is shown in the next section – the potential of zero total charge, pztc is close to P$_1$. The second region is negative to P$_2$, where the *in-situ* STM measurements reveal ordered adsorption of the cations.

11.2 Determination of the pztc

Currently only a few studies deal with the potential of zero charge (pzc) in ionic liquids [143–146, 160, 161]. Very often polycrystalline metal surfaces are used instead of single crystal surfaces which makes comparison difficult. Since the classical Gouy–Chapman

theory is not applicable in the case of ionic liquids, where Gouy–Chapman-minima are used to identify pzc's, the immersion technique was chosen to determine the potential of zero total charge (pztc) for Au(100) in $BMIPF_6$. By this method a freshly prepared, bare electrode is immersed into the ionic liquid at a pre-set potential and the current-density necessary for charging of the electric double layer is recorded [137]. These current transients are integrated yielding a charge density which is plotted versus the applied (immersion) potential. In this case, the flame annealed Au(100) crystal was mounted on the Kel-F cell and a certain potential was applied. Subsequently the IL was injected by means of an Eppendorf pipette to quickly cover the whole electrode surface, assuring that the electrolyte first established contact with reference and counter electrodes before hitting the working electrode. Although the wetting procedure required only approximately 5 s, settling of the current is much slower, thus the transients were recorded over several minutes. The integrated current transients are shown in Fig. 11.2a. Unlike for measurements in aqueous solutions the charge-density curves do not converge which means that the current transients are power-law like rather than exponential. Consequently the charge depends on the duration of the experiment.

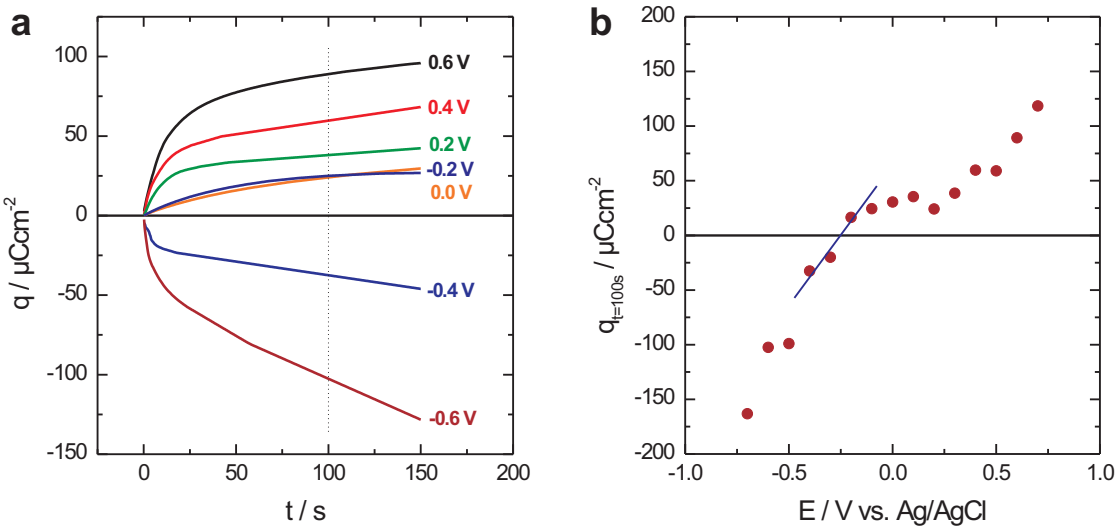

Figure 11.2: (a) Integrated immersion transients at potentials indicated for Au(100) in $BMIPF_6$ and (b) the charge calculated for 100 s as a function of potential. The zero crossing is around -250 mV.

In Fig. 11.2b charges for 100 s integration time are plotted versus the immersion potential. The straight line marks the zero-crossing, which is around -250 mV vs. Ag/AgCl, its slope corresponds to a value in the order of 100 μFcm^{-2}. The potential of the zero-crossing

coincides with the cathodic peak in the CV of Fig. 11.1. It is presumed that this potential marks the rearrangement of the ionic liquid, when anions change with cations as the potential is decreased. Compared to Au(111) in $BMIPF_6$ the zero-crossing is shifted by about 150 mV towards more negative potentials (see Fig. 9.4). This is in good agreement with the pzc's of the different surface orientations of gold in aqueous electrolytes [162]. Obviously the values for the pztc for Au(111) and Au(100) in $BMIPF_6$ show the same behaviour as the work functions of the different metal surfaces in UHV. Hence it is concluded that the pztc equals the pzc which would suggest that there is either no specific adsorption of the ions on the surface, or their adsorption affects the pztc for Au(100) similarly to that for Au(111).

11.3 Impedance Studies

As peak P_1 is in the vicinity of the pztc, its origin is most probably the anion/cation replacement at the surface. The reverse (anodic) process is much more slow, since the anodic counterpart of P_1 is a wave rather than a peak. Impedance spectroscopy provides a method for separating the „how much“ and „how fast“ aspects of charge accumulation.

The -0.6 V to +0.5 V potential range (bordered by peaks P_2 and P_3) represents a potential window within which the current seems to be non-faradaic in nature, hence might be considered as a double layer charging/adsorption region. This part of the voltammogram is reproducible for many hours provided the potential was kept within this range. Accordingly, the impedance studies were done within the above limits.

Impedance spectra, $Z(\omega)$, have been measured as a function of potential, and according to their capacitive nature, it is expedient to plot them in capacitance representation (Fig. 11.3), i.e., as $C(\omega) = 1/i\omega(Z(\omega) - R_s)$ where R_s is the series resistance determined by fitting. For each potential the capacitance spectra are of two-arc structure.

As it has been demonstrated recently [163], these two-arc spectra can be very well fitted (typically $\chi^2 \leq 10^{-5}$) by the impedance function of the equivalent circuit shown in Fig. 11.4. The fitted capacitance values, as a function of potential, are shown in Fig. 11.5. The high-frequency capacitance shows little if any potential dependence in the 1 V range of the measurement. In contrast, the C_1 and C_2 capacitances show a step and a peak at around 0 V, respectively. The peak of the C_2 capacitance is of the same origin as the P_1 peak of the CV of Fig. 11.1 at -250 mV — the location difference can be understood if one takes into account that the impedance spectrum series have been measured with an apparent scanrate of 0.02 mVs^{-1}, i.e., 3.5 orders of magnitude slower than the 50 mVs^{-1}

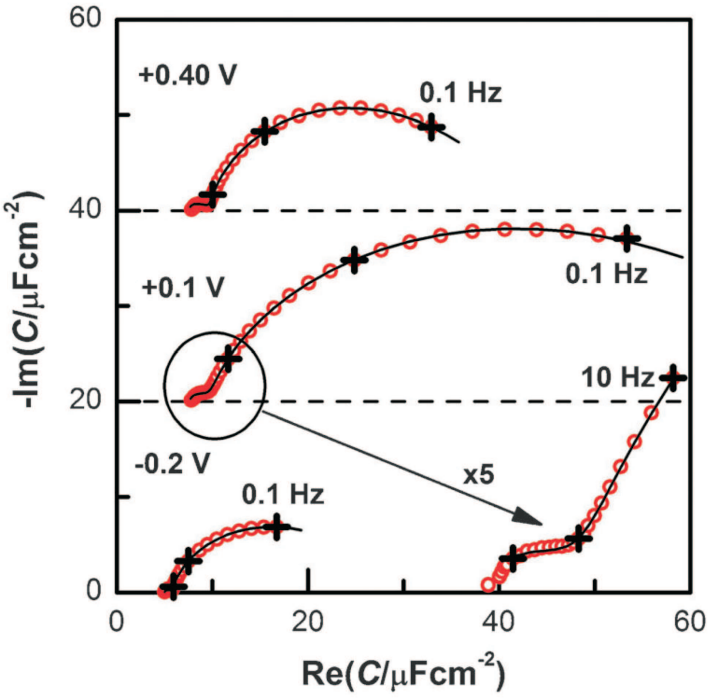

Figure 11.3: Complex plane plot of the capacitance spectra at potentials indicated. The 10 Hz, 1 Hz, and 0.1 Hz points are marked by crosses; solid lines are the fitted curves according to the equivalent circuit in Fig. 11.4. The spectra are shifted along the ordinate for visibility reasons; the spectrum of +0.1 V is plotted also in a magnified form.

CVs of Fig. 11.1. As for the similar system, the Au(111) in $BMIPF_6$, one found that this peak shifts approx. -0.06 V decade^{-1} with the scanrate (see inset of Fig. 9.1b). With this correction, the location in the CV and the C_2 peak potential can be safely regarded as identical.

To identify the origin of the equivalent circuit elements the impedance measurements – as a function of potential – have been repeated at various T temperatures, from room temperature up to 120 °C. Typical spectra are shown in Fig. 11.6. In general, spectra of two-arc shape can be measured up till 50–60 °C (lowest curve); the equivalent circuit in Fig. 11.4 is fully applicable. With further increasing the temperature, the capacitance spectra bend up, as if there was an additional parallel resistance. At high temperatures (e.g. 110 °C, uppermost curve in Fig. 11.6) the two arcs merge, and after cooling down the system the original room-temperature spectrum is no longer recovered; that is, some irreversible changes have happened. For the spectra of $T > 60$ °C the equivalent circuit in Fig. 11.4 is not applicable at all; however, R_s and – with a lower accuracy – C_{hf} can still be determined by fitting the high frequency part of the spectra. As seen in Fig. 11.7, capacitances show little temperature dependence, allowing the interpretation

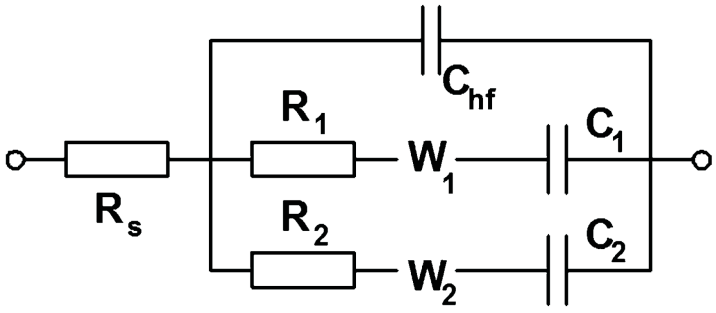

Figure 11.4: Equivalent circuit used for fitting the spectra. The W elements are defined via their impedance as $Z_W(\omega) = \sigma/\sqrt{i\omega}$.

that the capacitances characterize the double layer width, which is roughly temperature independent. In contrast, R_s, R_2 and W_2 depend strongly on temperature indicating that these are kinetics-related elements. The slope of the $\log(R_s)$ vs. $1/T$ curve is related to the activation energy – in the order of 30 kJmol^{-1} – for ion transport in the bulk; the somewhat steeper $\log(R_2)$ vs. $1/T$ line implies a 1.5× larger activation energy for the corresponding interfacial process.

11.4 Synopsis of the CV, pztc and Impedance Measurements

The CV peak P_1 and the peak of C_2 are of identical origin of charging. Since the pztc is in the vicinity of P_1, the charging can be attributed to the anion–cation replacement. In this case the R–W–C branches of the empirical equivalent circuit in Fig. 11.4 can be identified as adsorption impedances — one for the cation and the other for the anion adsorption. The situation is rather similar to the case of Rh(111)/0.1 M HCl [164] where the H^+/Cl^- adsorbate replacement peak can be characterized also by the equivalent circuit in Fig. 11.4. As it was demonstrated, the two branches could be assigned to the two ions by analyzing the concentration dependence of the spectra. In the present case, the concentrations of the IL constituents cannot be altered; however, an assignment of the branches to ions can be done by the following line of thoughts:

The overall capacitance (C_{hf} + C_1 + C_2) is much larger at +0.5 V (where $[PF_6]^-$ anions are adsorbed) than at -0.6 V (where the $[BMI]^+$ cations are adsorbed). Since C_2 is the dominant term of the (C_{hf} + C_1 + C_2) sum (cf. Fig. 11.5), the R_2–W_2–C_2 branch apparently belongs to the adsorption of the $[PF_6]^-$ anions. This branch is responsible for the low frequency loop of the capacitance spectra, thus adsorption/desorption of $[PF_6]^-$

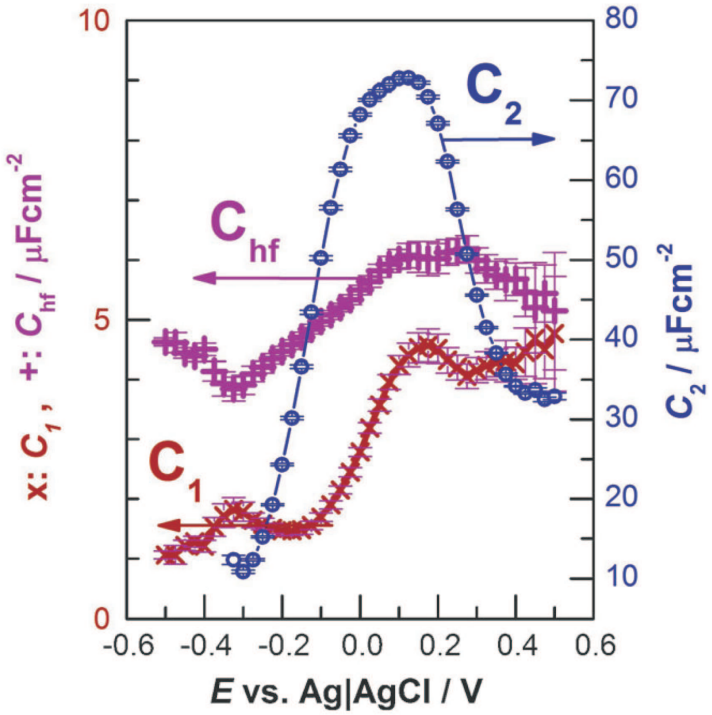

Figure 11.5: The fitted equivalent circuit parameters, as a function of potential. C_{hf} (+), C_1 (×), and C_2 (○) data obtained from fitting of the spectra.

is much slower than that of $[BMI]^+$.

The interpretation of the W elements — along with the finding that their temperature-dependence is similar to that of the bulk conductivity of the IL (cf. Fig. 11.7), remains at present unsettled.

The C_{hf} capacitance – which corresponds to fast charging, because of its electrostatic nature – shows little if any potential dependence, at least in the potential range close to the pztc. Thus the related theories [12,13] – predicting peaks in the range of 10–20 μFcm^{-2} at the pzc – are at variance with the present results.

11.5 *In-situ* STM Studies

In-situ STM measurements were performed in order to characterize the surface morphology of Au(100) in $BMIPF_6$ at various potentials. After flame annealing the freshly prepared Au(100) crystal was immersed at +0.1 V vs. Ag/AgCl, i.e., positive of the pztc. Fig. 11.8a shows a flat, completely unstructured gold surface with one monoatomic high gold island. At +0.1 V $[PF_6]^-$ anions should be accumulated at the metal surface. However, in our STM experiments we could not observe any ordered layer of anions. This finding is contrasted by experiments with the $[BF_4]^-$ anion where an ordered adlayer at positive potentials was

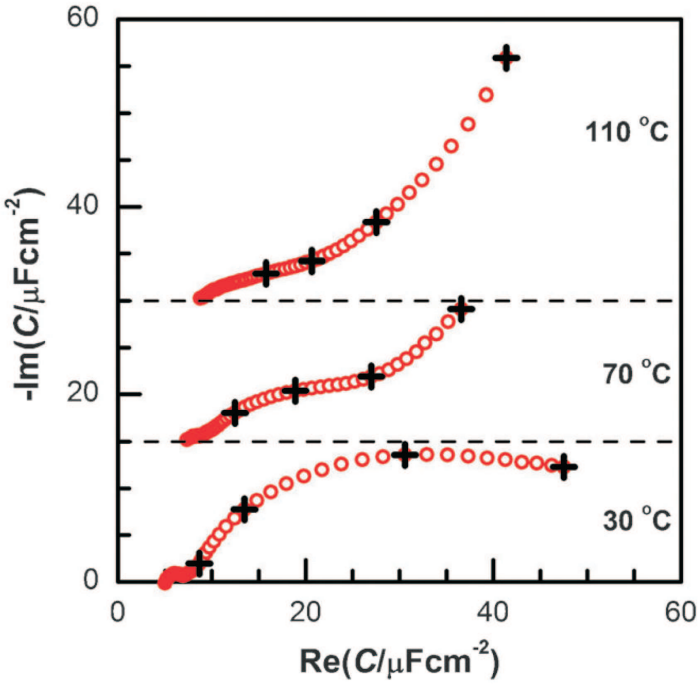

Figure 11.6: Complex plane plot of the capacitance spectra for -0.2 V at temperatures indicated. The 10 Hz, 1 Hz, 0.1 Hz and 0.01 Hz points are marked by crosses. The spectra are shifted along the ordinate for visibility reasons.

reported [165]. In other cases though, STM images of a Au(111) surface in contact with $BMIPF_6$ suggest a Moiré-like pattern of the $[PF_6]^-$ anion with a 2D phase transition to an ordered ad-structure upon cathodic excursion [152]. Decreasing the potential to values negative of the potential of zero charge causes a clear change of the surface structure. At -800 mV small holes appear in the surface which have an average depth of 0.65 nm ± 0.05 nm (Fig. 11.8b). These holes could be the result of a reorganization of molecules within the IL layer in front of the electrode surface, as a consequence of the enhanced electrostatic interaction between the gold and the $[BMI]^+$ cations. Another explanation is the onset of a cation-induced etching process and a concomitant dissolution of gold atoms which would lead to holes. On Au(100) as well as on Au(111) in $BMIBF_4$ the observation of holes on the surface was reported at negative potentials and interpreted by such an etching process of the substrate [139,165]. At potentials negative of the small cathodic peak at -800 mV (see Fig. 11.1) an ordered adlayer became visible in STM. This is shown in Fig. 11.8c. Stripes are clearly seen, which are arranged in a rectangular pattern, reflecting the fourfold symmetry of the Au(100) substrate. One can still see holes on the surface and furthermore a layered structure. This layering corroborates the AFM observations by Atkin *et al.* of several ionic-liquid layers in front of the electrode [140, 166]. A closer look

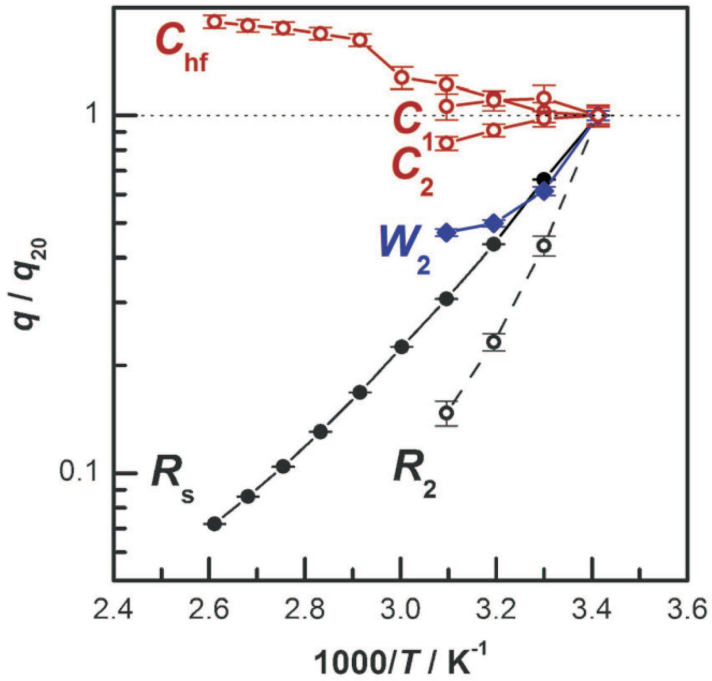

Figure 11.7: The fitted quantities q (R_s, capacitances, W_2, and R_2) normalized to their value of 20°C, q_{20}, as a function of temperature (in Arrhenius representation). The R_1 and W_1 parameters are not plotted due to their large errors.

on the stripes reveals their double-row structure (Fig. 11.9) which confirms the results of the Mao group in every detail [165]. According to Ref. [165] the outer bright spots are composed of the imidazolium ring system whereas the less intense inner spots display the butyl chains. We could observe a face-to-face configuration of the butyl chains (Fig. 11.9 inset). The width of each strip is 2.1 nm ± 0.2 nm. It is assumed that the $[BMI]^+$ cations are laying flat on the surface, stabilized by π–π interactions between the aromatic ring systems. The latter favours the layered assembly. On polycrystalline platinum in contact with imidazolium-based ILs sum-frequency-generation spectroscopy (SFG) demonstrates that at negative potentials the imidazolium ring tends to lie flat on the surface [151, 167]. Van der Waals forces between the butyl chains cause additional stabilization of the rows.

Decreasing the potential to -2.1 V generates a complete disappearance of the cation row-structure (Fig. 11.8d). At this potential the ionic liquid decomposes (cation breakdown) indicated by strong cathodic currents in the CV. On the STM image one can observe the Au(100) (hex)-reconstruction rows which are a well-known phenomenon in aqueous electrolytes [138, 168]. The image in Fig. 11.8d looks slightly distorted which could have its origin in the on-going reduction process, the products perturbing the imaging process of the STM. Still a debatable issue is whether the unreconstructed (1 × 1) surface or

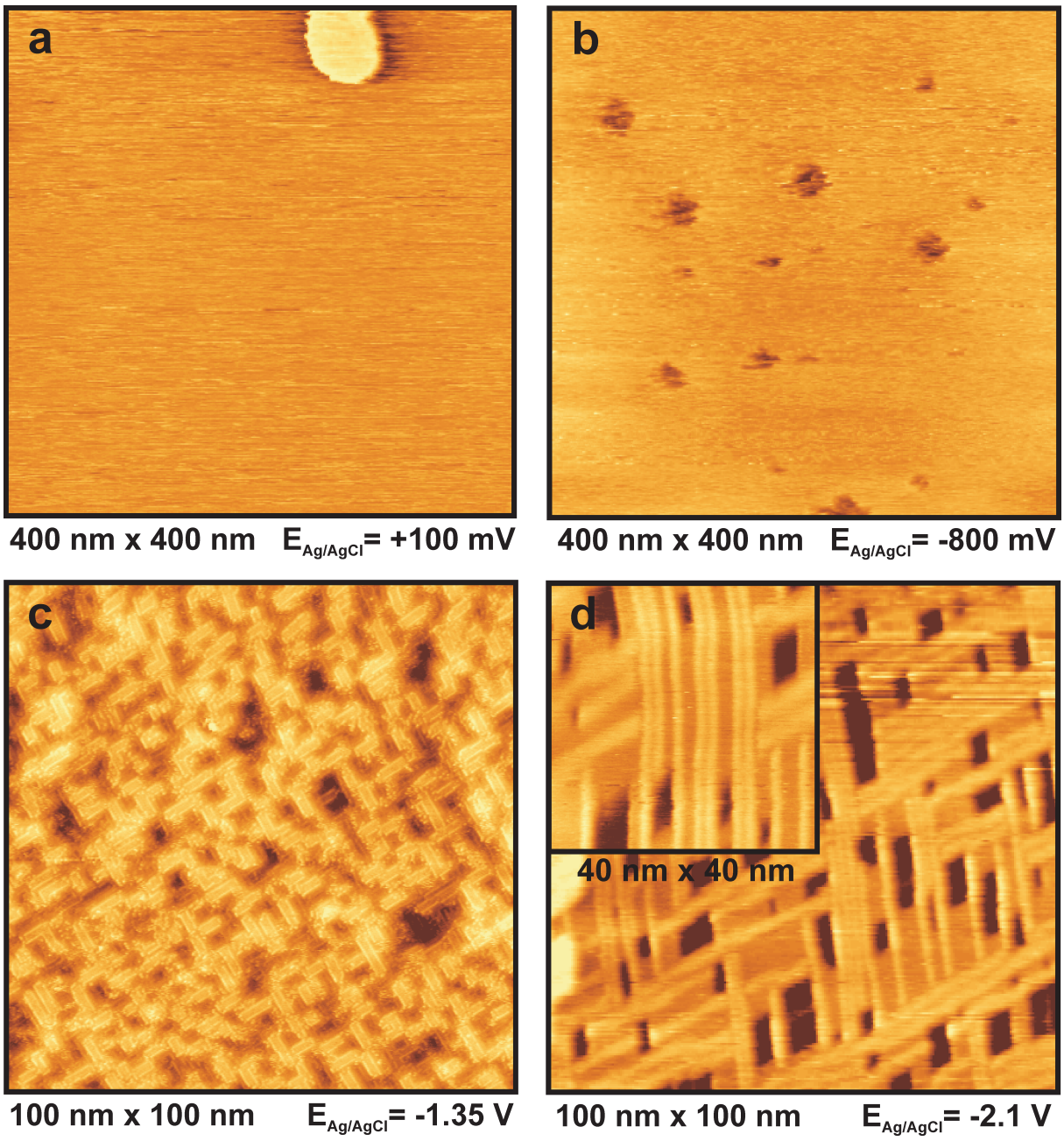

Figure 11.8: STM images of Au(100) in $BMIPF_6$ at four different electrode potentials.

the (hex)-reconstruction is below the adsorbed cations for $E >$ -2.0 V. X-Ray diffraction measurements could help answering that question.

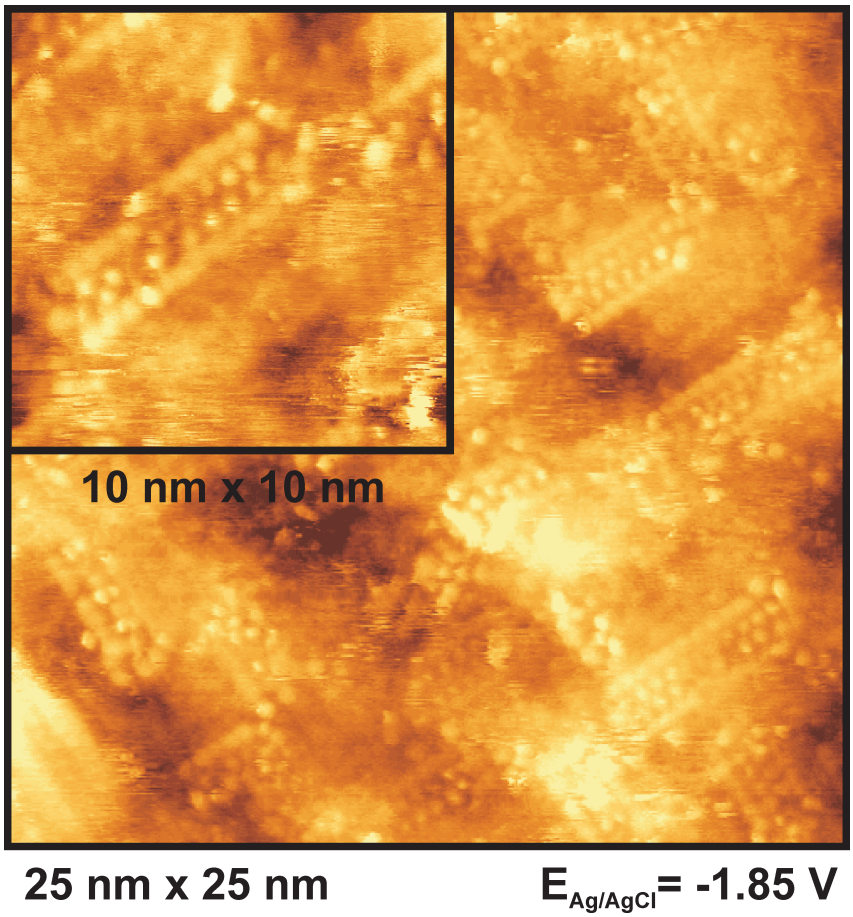

Figure 11.9: Cation row-structure, high resolution STM image is shown in the inset.

12 The Gold Surface in $BMITf_2N$

12.1 Cyclic Voltammetry and Impedance Spectroscopy

In order to clarify whether or not the anion affects the interfacial properties, the properties of $BMITf_2N$ have been tested and compared with those of $BMIPF_6$. This is the subject of the present section.

The CV of Au(100) is shown in Fig. 12.1a. It demonstrates the effect of cleaning with the procedure described above using molecular sieve of 0.3 nm pore size. The black curve represents a CV for $BMITf_2N$ as purchased from Merck KGaA in high-purity quality (water $\leq$ 100 ppm, halides $\leq$ 100 ppm). The liquid was vacuum dried over night at 80 °C in order to remove residual water. At about -1 V a huge increase in the negative current density is observed which is attributed to the reduction of impurities in the ionic liquid. The high current density of the big cathodic peak at around -1.4 V ($\sim$ 200 μAcm^{-2}) indicates a stronger contamination of the IL compared to $BMIPF_6$. After adding molecular sieve of 0.3 nm pore size the faradaic currents on both sides of the potential window disappear almost completely (Fig. 12.1a red curve). A small hump at -1.4 V can still be noticed which might be due to small amounts of impurities left in the liquid. A rather smooth double layer charging region, especially in the positive part can be seen. The DC-capacitance, calculated as j/ν from the CV amounts to 50 μFcm^{-2}. Additionally a cathodic hump (P) at -0.6 V appears. The hump has a flat anodic counterpart which can be seen more clearly in a more sensitive current scale (Fig. 12.1b). The characteristics of the CV resemble that for Au(100) in $BMIPF_6$ where cathodic peaks are always more pronounced than the anodic counterparts. One assumes that the cathodic hump at -0.6 V in Fig. 12.1b is related to a specific interaction between the gold substrate and the ionic liquid. As in previous chapters already described it is attributed to a rearrangement of the IL side of the double layer. Determination of the pztc could corroborate this assumption, unfortunately reliable experimental data are still missing. P is shifted about 400 mV towards more negative potentials compared to studies in $BMIPF_6$. This might be explained

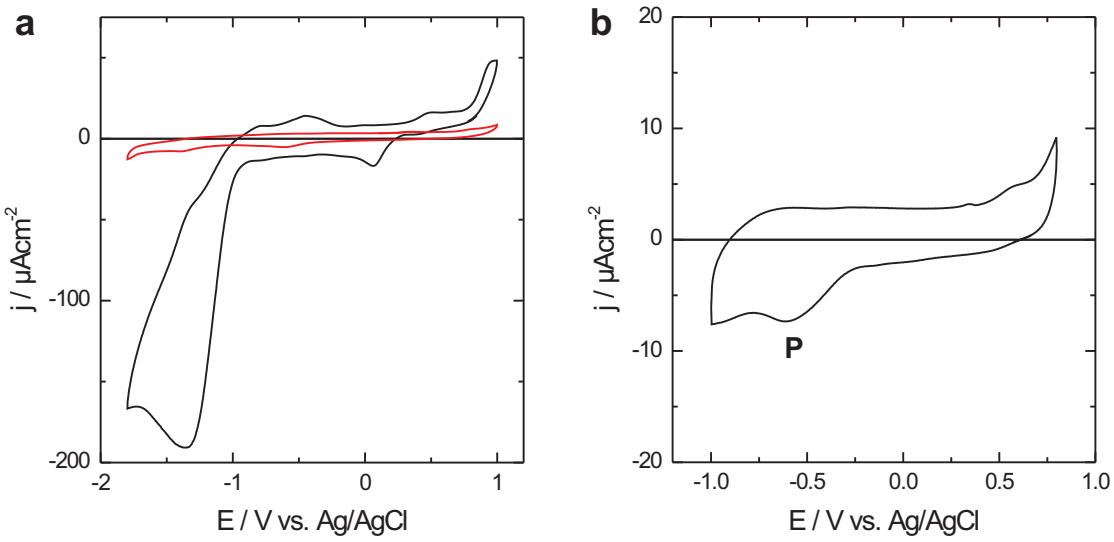

Figure 12.1: Cyclic voltammogramms recorded at 50 mV/s for Au(100) in $BMITf_2N$. (a) Black curve: Vacuum-dried ionic liquid from Merck. Red curve: After adding molecular sieve with 0.3 nm pore size. (b) High resolution CV within the -1 V to +0.8 V scan range. All potentials with respect to the Ag/AgCl pseudo-reference electrode.

with the size of the $[Tf_2N]^-$ anion: Due to the size and the sterical hindrance of the anion a more negative potential is needed to rearrange the ions in front of the electrode surface. The -0.4 V to +0.6 V potential range represents a potential window within which the current seems to be non-faradaic in nature. It might be considered as a double layer charging/adsorption region. Impedance studies were done within the above limits. The spectra ($Z(\omega)$) have been measured as a function of potential and plotted in capacitance representation (Fig. 12.2a). The spectra can be fitted using the equivalent circuit shown in Fig. 12.2b containing constant-phase-elements (CPEs). A two-arc structure of the spectra can be well observed in the potential range between 0.0 V and -0.3 V. However, the double-arc structure of the spectra is not that obvious compared to Au(100) in $BMIPF_6$. For the entire potential range the high-frequency capacitance shows little if any potential dependence. A value of about 4 μFcm^{-2} could be determined from the spectra. This is in good accordance with high-frequency values obtained for Au(100) in $BMIPF_6$ (chapter 11). Apparently changing the anion has only little influence on the double layer capacitance.

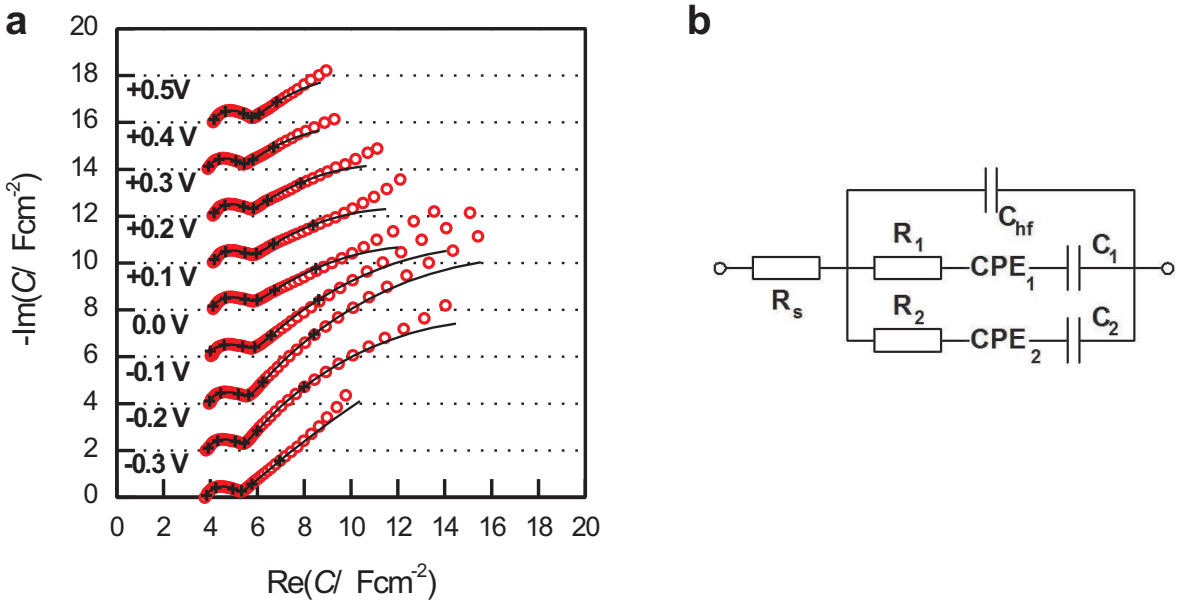

Figure 12.2: (a) Complex plane plot of the capacitance spectra at potentials indicated. Solid lines are the fitted curves according to the equivalent circuit in (b). The spectra are shifted along the ordinate for visibility reasons.

12.2 *In-situ* STM Studies

In order to characterize the surface morphology of Au(100) in $BMITf_2N$ *in-situ* STM measurements were performed. Similar to Au(100) in $BMIPF_6$ no ordered adlayer could be observed at positive potentials. Thus it is concluded that neither $[PF_6]^-$ nor $[Tf_2N]^-$ forms an ordered structure on gold which can be imaged with the STM. At negative potentials (negative of P in Fig. 12.1b), however, an ordered adlayer becomes visible (Fig. 12.3a). Stripes can be seen which are arranged in a rectangular pattern. The stripes have the same dimension as in case of Au(100) in $BMIPF_6$ and $BMIBF_4$ [165]. Since only the anion was changed in these experiments it can be concluded that the observed row-structure is caused by the $[BMI]^+$ cations. Again π–π interactions between the aromatic ring systems are assumed which might explain the observed layering. At sufficiently negative potentials the ionic liquid decomposes ($\sim$ -2 V vs. Ag/AgCl) resulting in a complete disappearance of the ad-structure. The cation gets reduced and the Au(100) (hex)-reconstruction appears (Fig. 12.3b). From this finding one might presume that a reconstructed Au(100) surface lies underneath at negative potentials. Another possibility is that the (hex)-reconstruction

is formed simultaneously with the dissolution of the row-structure. The height of some islands coincide with the value obtained for gold islands in aqueous electrolytes, which might support this [168]. Probably the synergetic effect of an unfavourable surface for adsorption and the stability limit of the electrolyte at negative potentials leads to a disappearance of the ad-structure. X-ray diffraction experiments could help answering that question.

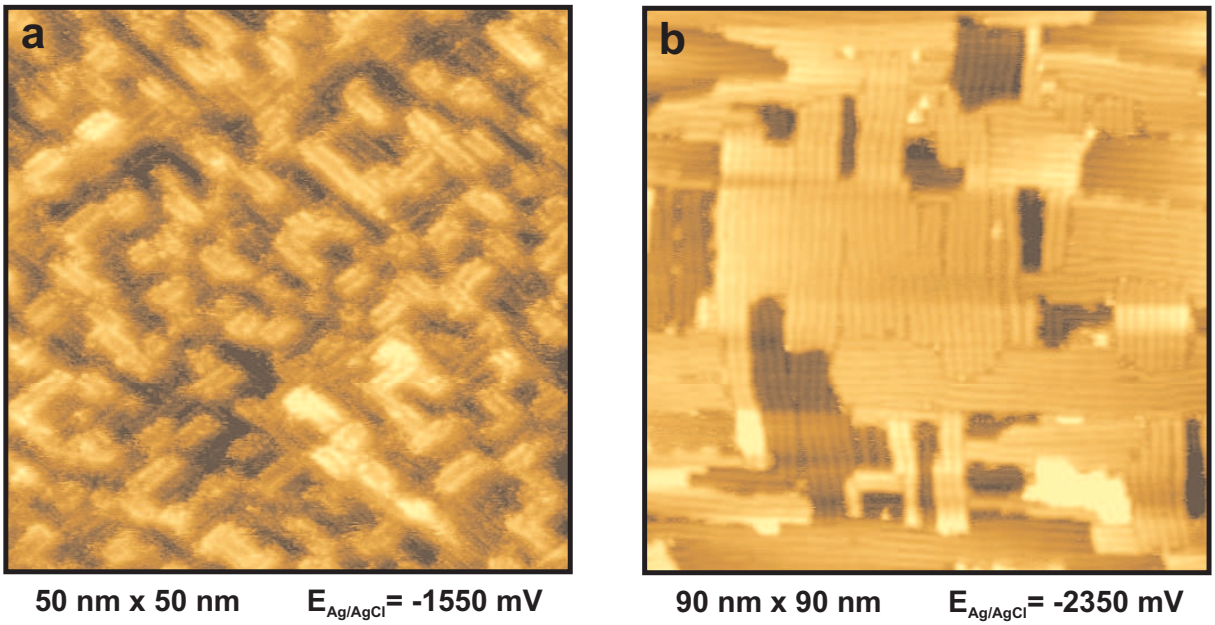

Figure 12.3: STM images of Au(100) in $BMITf_2N$. Potentials as indicated in the figures (courtesy C. Müller).

For Au(111) in $BMITf_2N$ the worm-like structure appears upon cathodic potential excursion (Fig. 12.4). Like for Au(111) in $BMIPF_6$ no ad-structure could be imaged at positive potentials. Therefore again one concludes that $[Tf_2N]^-$ does not adsorb on the Au(111) surface. The worm-like structure in Fig. 12.4 has the same appearance as for Au(111) in $BMIPF_6$ and $BMIBF_4$ [139]. Since only the anion was changed in these experiments it can be again concluded that the observed ad-structure is caused by the $[BMI]^+$ cations. Obviously the Au(111) substrate is inappropriate for the $[BMI]^+$ cations to form a regular pattern. Again π–π interactions between the aromatic imidazolium ring systems might be responsible for the layering. Therefore experiments with non-aromatic ionic liquids could help to understand the observed ad-structures. Still unclear is the question whether a reconstructed $(\sqrt{3} \times 22)$ or a unreconstructed (1×1) surface is beneath the worm-like structure.

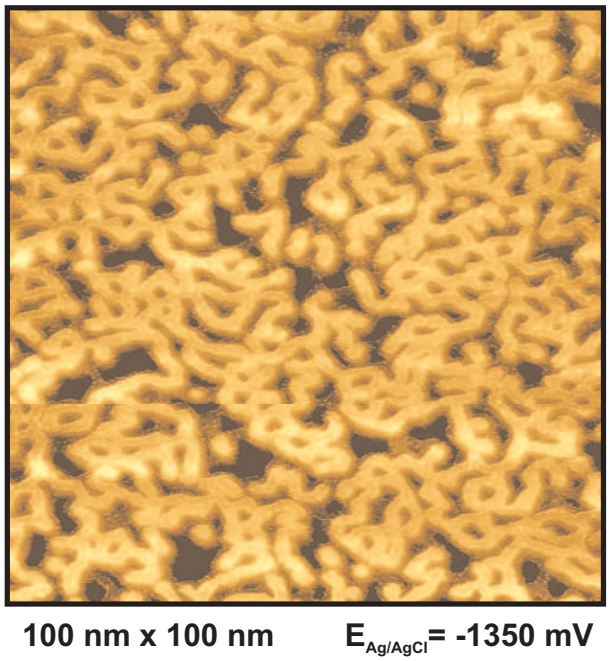

Figure 12.4: STM image of Au(111) in $BMITf_2N$ at negative potential (courtesy C. Müller).

13 The Gold Surface in $Bu_2Et_2Me_2GuanTf_2N$

In order to investigate the influence of the cation on interfacial properties, a guanidinium-based ionic liquid was synthesised (M. Arkhipova, G. Maas, Institute of Organic Chemistry I, University of Ulm) containing a non-aromatic guanidinium cation instead of an aromatic imidazolium cation (see Figs. 3.1 and 3.3). The results have been discussed and compared with those of $BMIPF_6$. This is the subject of the present chapter.

New types of ionic liquids based on hexaalkyl-substituted guanidinium cations have been synthesised which exhibit a good thermal stability up to 400 °C [35,169–171]. They are unreactive towards bases and most nucleophilic reagents due to an excellent stabilisation of charge in the peralkylated cation. Variations in the alkyl chains affect physicochemical properties such as melting point, viscosity, hydrophobicity, and polarity [35, 170–173]. Guanidinium-based ILs can serve as reaction media for transition metal catalysed reactions, e.g. the Heck [174] and the Sharpless AD [175] reactions, as well as for the selective oxidation of benzyl alcohols [176]. Guanidinium ILs have also been synthesised for applications in lithium batteries [177, 178] and solar cells [179, 180]. Electrochemical studies involving these new types of ILs, however, are quite rare and the metal/guanidinium IL interface is far from being well understood [181].

N,N-dibutyl-N',N'-diethyl-N",N"-dimethylguanidinium-bis(trifluoromethylsulfonyl) imide ($Bu_2Et_2Me_2GuanTf_2N$) was selected from a set of five hexaalkylguanidinium salts (Table 13.1) because its cyclic voltammogram displayed the most favourable features. Au(111) and Au(100) single crystal electrodes were employed throughout the experiments; however, unless otherwise noted in connection with CV and impedance measurements, only the experiments with Au(100) are shown, because the two crystal faces of Au yielded very similar results.

Ionic liquid	Neg. limit [V]	Pos. limit [V]	PW	Reproducible CV
$Bu_2Et_2Me_2GuanTfO$	-0.6	+0.6	1.2	yes
$Bu_2Et_2Me_2GuanTf_2N$	-1.8	+1.0	2.8	yes
$Bu_2Et_2Hex_2GuanTf_2N$	-1.8	+0.8	2.6	yes
$Bu_2Et_2Me_2Guan(CN)_2N$	-1.5	+0.6	2.1	no
$Bu_2Hex_2Me_2Guan(CN)_2N$	-1.5	+0.6	2.1	no

Table 13.1: Cyclic voltammetry behaviour of different guanidinium-based ionic liquids in contact with a Au(111) surface. The potential limits refer to the Ag/AgCl pseudo-reference electrode (PW: Potential window).

13.1 Cyclic Voltammetry and Impedance Spectroscopy

A cyclic voltammogram at 50 mV/s scanrate recorded on Au(100) in $Bu_2Et_2Me_2GuanTf_2N$ is presented in Fig. 13.1. It appears to be a completely featureless, almost capacitive CV. The average double layer charging current appears to be considerably lower compared to Au(111) and Au(100) in $BMIPF_6$ [163] (the DC capacitance, calculated as charging current divided by scan rate, is about 12 $\mu F/cm^2$, in contrast to the latter systems for which this figure is about twice as large). At room temperature faradaic currents occur below -1.8 V and above +1 V, respectively. The „potential window“ of the ionic liquid decreases with increasing temperature (Fig. 13.1 inset). Cycling within these limits yields reproducible CVs. We found no distinctive peaks on the CV which would indicate the pzc as in $BMIPF_6$. The impedance measurements have been performed as a function of potential and of temperature in the potential range of ideal polarizability on both Au single crystal electrodes. Capacitance spectra of the interface calculated as described in section 4.2 are plotted in Figs. 13.2b and 13.3a to demonstrate the following points:

1. The $C(\omega)$ functions at room temperature are arc-shaped (Fig. 13.2b); the second, low frequency arc becomes pronounced at increased temperatures only (Fig. 13.3a, upper curve). The low frequency arc does not show any inclination towards the real axis even at 0.01 Hz, thus an estimation of the low frequency limit value of capacitance from the spectra is practically impossible.

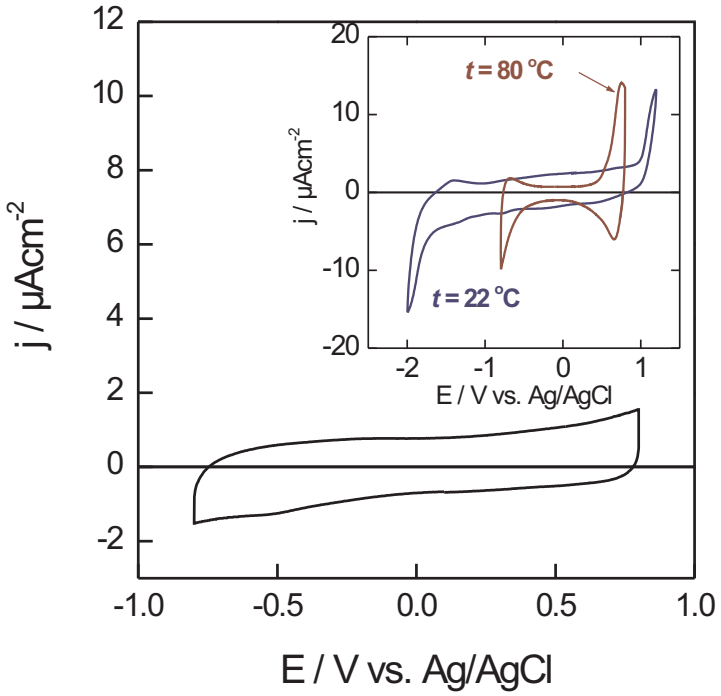

Figure 13.1: Cyclic voltammograms of Au(100) in $Bu_2Et_2Me_2GuanTf_2N$ at a scan rate of 50 mV s^{-1} just after filling the cell. Inset: CVs at two temperatures, to illustrate the electrochemical window.

2. The spectra show little if any potential dependence (Fig. 13.2b). The values of C_{hf} and the span of the high frequency arc ($= C_1$), 1-2 μF/cm^2, are much smaller than those in the ionic liquid $BMIPF_6$ (section 11.3) (3-6 μF/cm^2 [163]), most probably because the ions constituting the electrolyte are much larger than in $BMIPF_6$, thus the double layer is assumed to be thicker.

3. The characteristic capacitance values of the spectra, C_{hf}, and the span of the high frequency arc ($= C_1$) are somewhat temperature dependent (Fig. 13.3a); the spectrum points are shifted clockwise along the arcs with increasing temperature. Quantitatively, this can be characterized by fitting the parameters of the equivalent circuit shown in the inset of Fig. 13.3a to the spectra (note that this circuit is a special case of the one of Fig. 13.2a, with omission of the serial L_s and R_s, and the $C_2 \to \infty$ elements). Whereas the CPE exponents and the capacitances exhibit no or little temperature dependence, R_s and the CPE coefficients are markedly temperature dependent quantities as it is shown in Fig. 13.3b. Disregarding the hysteresis of the

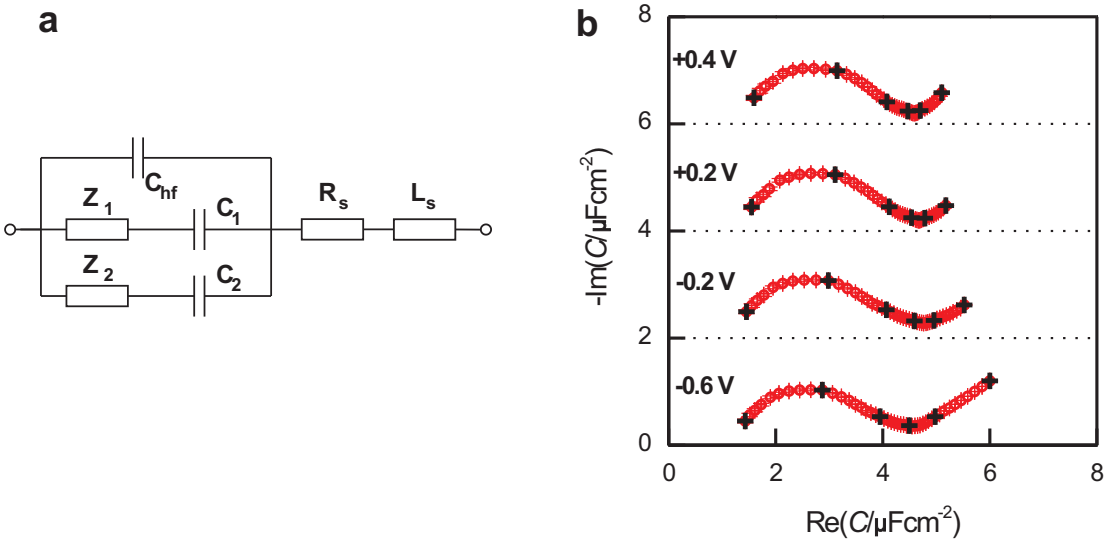

Figure 13.2: (a) Equivalent circuit used for fitting the spectra. The L_s element (with $Z(\omega) = i\omega L_s$) is a term having the only role for correcting the minor phase shifts at high frequency due to stray capacitances and to instrumental imperfections; the R_s is the bulk resistance of the electrolyte; the three-branched network models the interface. (b) Complex plane plot of the capacitance spectra, in the 0.1 Hz-10 kHz range, at potentials indicated, measured at 22 °C. The points measured at, or close to, 10^k Hz (where $4 \geq k \geq$ -1 is integer) are marked by crosses. The spectra are shifted along the ordinate for visibility reasons.

curve – which is a consequence of that the capacitance spectrum points are much above the real axis even at very low frequencies – the slopes of the CPE exponents vs. $1/T$ lines are close to that of the R_s vs. $1/T$, implying that the processes responsible for the CPEs have the same (or similar) activation energy as the ion transport in the bulk. An explanation or theory for the rather unusual equivalent circuit of the double layer, however, cannot be offered at present.

13.2 *In-situ* STM Studies

The Au(100) surface in $Bu_2Et_2Me_2GuanTf_2N$ was characterized at various potentials with the *in-situ* STM. The freshly prepared Au(100) crystal was immersed at -250 mV vs. Ag/AgCl after the flame annealing; an island-covered surface (Fig. 13.4a) can be imaged at that potential. The islands are monoatomic in height and appear round rather than rectangular in shape, which points towards an increased surface mobility of the gold atoms.

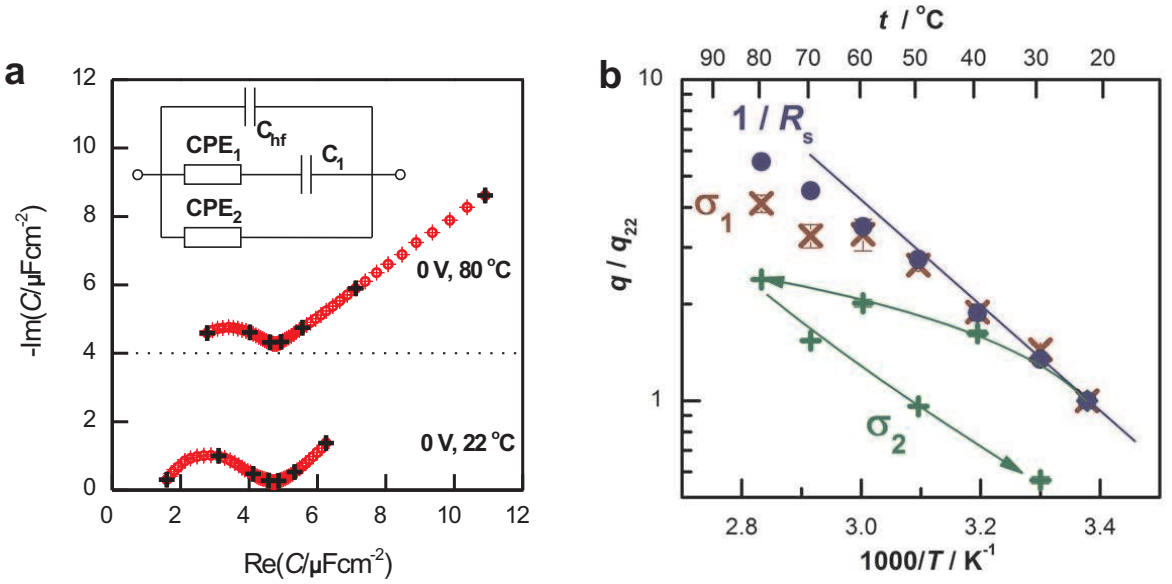

Figure 13.3: (a) Complex plane plot of the capacitance spectra, in the 10 mHz-10 kHz range for 0.0 V at the two temperatures indicated. The points measured at, or close to, 10^k Hz (where $4 \geq k \geq -2$ is integer) are marked by crosses. The spectra are shifted along the ordinate for visibility reasons. Inset: The equivalent circuit of the interface (see text). (b) The fitted quantities q ($1/R_s$ (•), σ_1 (×) and σ_2 (+)) normalized to their value at 22 °C, q_{22}, as a function of temperature (in Arrhenius representation). Arrows illustrate the order of measurements (see also text).

No ordered ad-layer of the $[Tf_2N]^-$ anions could be observed at positive potentials. The surface coverage of the islands was calculated to be 23%, in good agreement with observations in aqueous electrolytes [168,182]. Therefore we suppose that the islands originate from the lifting of the thermally induced (hex)-reconstruction at positive potentials [22,128]. Due to the hexagonal arrangement of the reconstructed phase, 25% more atoms can be packed into the surface compared to the unreconstructed (1×1) phase. The islands disappear by lowering the potential to more negative values (Fig. 13.4b). Simultaneously a striped pattern emerges, which indicates the formation of the potential-induced (hex)-reconstruction rows. This behaviour resembles to the growth of the (hex)-reconstruction rows in aqueous electrolytes [183]. In Fig. 13.4b the surface coverage of the islands decreases to 10%. A higher resolution of the STM image reveals stripes as well as holes (Fig. 13.4c). The holes are rectangular in shape displaying the fourfold symmetry of the unreconstructed (100) substrate. In contrast to the cases with imidazolium-based ionic liquids no ad-structure of the cation could be observed at negative potentials. Previous studies in $BMIPF_6$ and $BMIBF_4$ demonstrate layering of ordered stripes in a rectangular pattern [165]. In the-

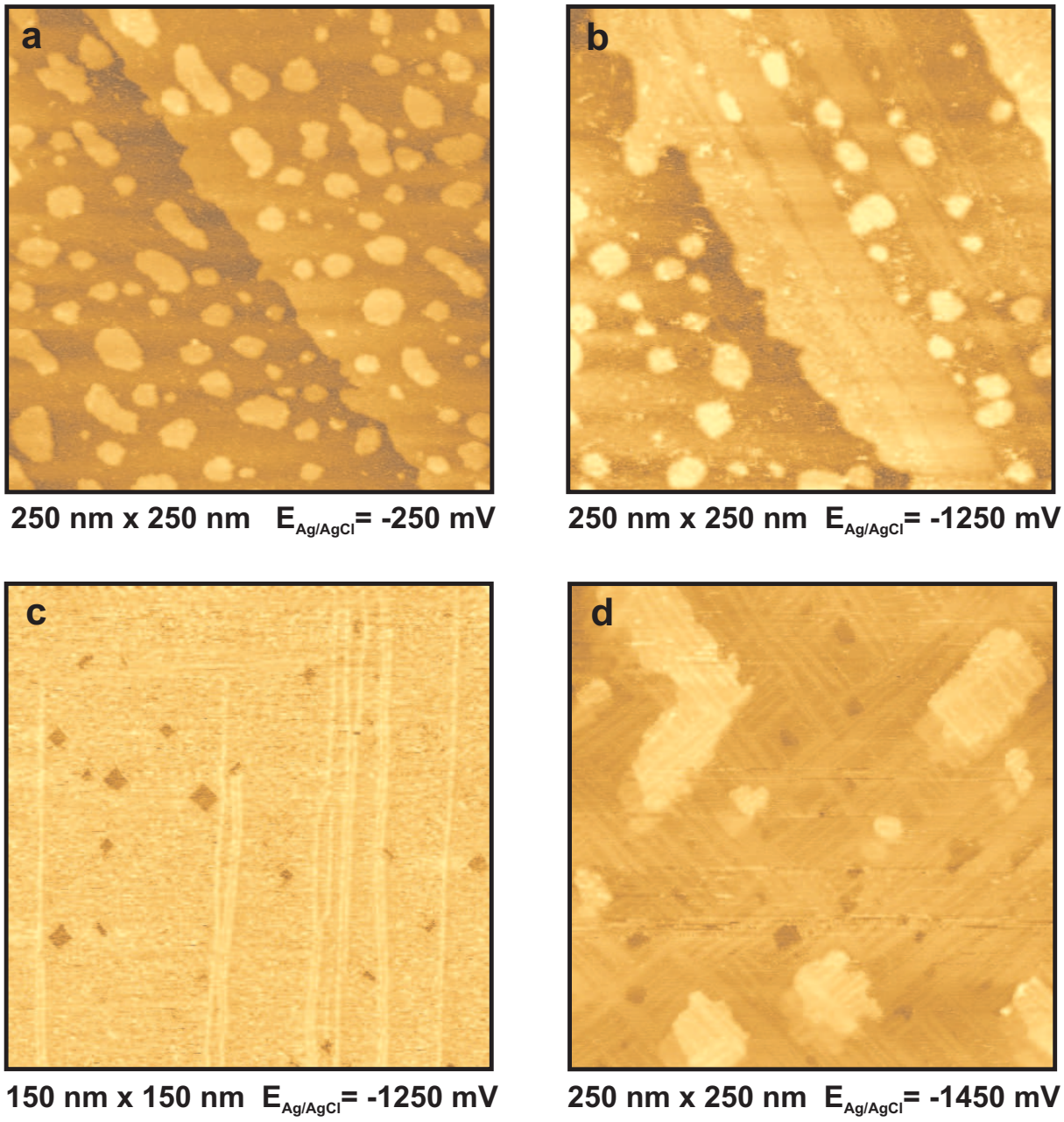

Figure 13.4: *In-situ* STM images of Au(100) in $Bu_2Et_2Me_2GuanTf_2N$ at different electrode potentials [184].

se cases π–π interactions between the aromatic imidazolium ring systems are assumed causing the observed arrangement in layers. The lack of an ad-structure of the guanidinium cation at negative potentials could have two reasons: Firstly, the absence of an aromatic π-system which is expected to interact with other cations as well as the Au(100) surface and secondly a sterical hindrance of the guanidinium-cation due to the six alkyl chains which do not allow the charged core of the ion as close to the surface as the imidazolium-cation. This can be corroborated by comparing the impedance spectra with those obtained for the imidazolium-based $BMIPF_6$ (section 11.3). There a value of about 5 μFcm^{-2} was determined, whereas a much smaller double layer capacitance of 1-2 $\mu F/cm^2$ was found in the case of $Bu_2Et_2Me_2GuanTf_2N$. At -1450 mV the (hex)-reconstruction rows as well as remaining gold islands are visible (Fig. 13.4d). For Au(100) in $BMIPF_6$ the reconstruction rows appear only at very negative potentials where the decomposition of the ionic liquid (reduction of the cation) occurs. In the case of $Bu_2Et_2Me_2GuanTf_2N$ the reconstruction rows can be observed at much more positive potentials (-1.45 V) well before reduction of the IL (cf. Fig. 13.1 inset). Taking this into consideration one might presume that a reconstructed Au(100) surface is present underneath the observed stripe pattern caused by the imidazolium cation.

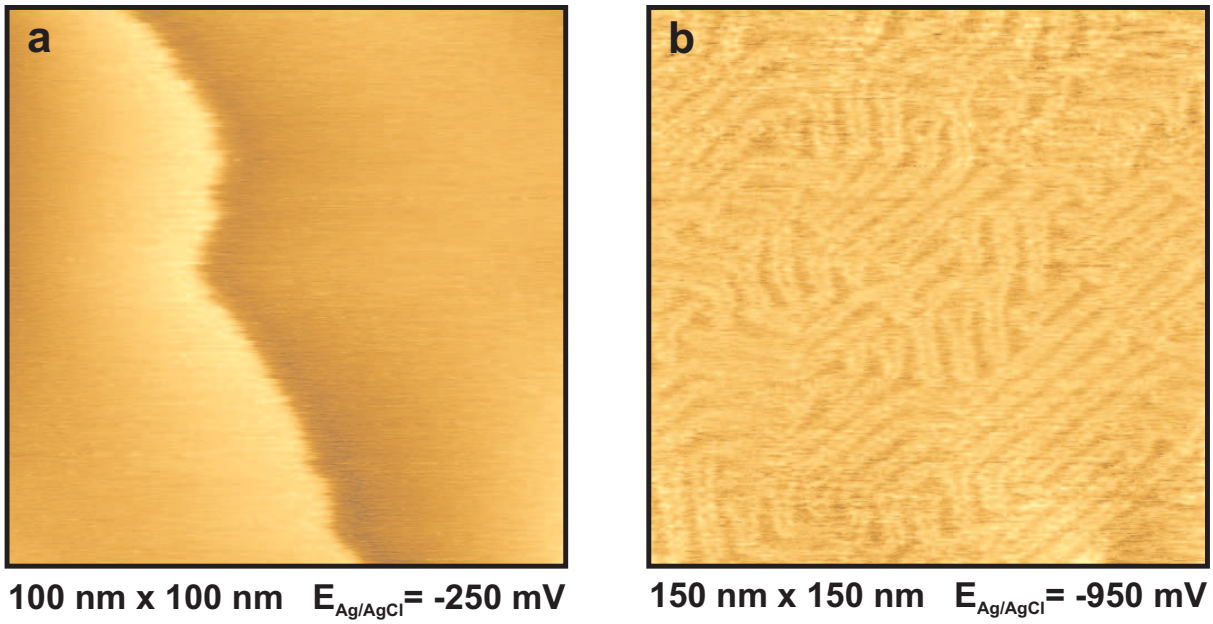

Figure 13.5: (a) Au(111) in $Bu_2Et_2Me_2GuanTf_2N$ at -250 mV, (b) herringbone reconstruction at -950 mV [184].

The surface of Au(111) immersed in $Bu_2Et_2Me_2GuanTf_2N$ as a function of potential is presented in Fig. 13.5. A flat gold surface with a monoatomic high step can be seen at -250 mV (Fig. 13.5a). The step edge displays a frizzy structure which is indicative

for a high surface mobility of gold atoms in this ionic liquid. Contrarily to Au(100) in $Bu_2Et_2Me_2GuanTf_2N$ no gold islands could be noticed at -250 mV. The absence of gold islands can be explained with a fast diffusion of gold atoms on the surface to energetically more favourable sites such as step edges. Due to a possible potential-induced lifting of a reconstructed surface an excess of gold islands of only 4% can be expected [21]. Therefore the islands probably disappear within a very short time before starting the STM measurements. A reconstructed Au(111) surface becomes visible after decreasing the potential to -950 mV (Fig. 13.5b). This potential induced $(\sqrt{3} \times 22)$ reconstruction is a well known phenomenon in aqueous electrolytes and was also thoroughly studied with the STM in vacuum [23, 162, 185–188]. The $(\sqrt{3} \times 22)$ reconstruction, also known as the herringbone structure, is formed by a reduction of surface energy of the uppermost layer in which the atoms occupy fcc and hcp sites. One can clearly identify elbows caused by a rotation of the herringbone ridges. The bending resembles the „chevron“ structure observed in UHV [188]. The „chevron“ structure could also be studied in aqueous electrolytes using a gold crystal previously annealed at higher temperatures [22]. The bending of the reconstruction rows illustrates a surface rich in defects playing an important roll as nucleation sites during metal deposition [189]. Unlike observations in imidazolium-based ionic liquids, the surface does not exhibit a worm-like structure upon cathodic excursion [88, 139]. The aromatic ring system (π–π interactions) of the cation, which is missing in case of guanidinium-based ILs, is probably responsible for the generation of the worm-like structure. Using a non-aromatic pyrrolidinium-based ionic liquid, the herringbone reconstruction could also be observed [190].

14 Metal Deposition from Ionic Liquids

The initial stages of Pd deposition on gold surfaces from a solution of $PdCl_2$ in $BMIPF_6$ is discussed in this chapter.

Palladium was chosen because of its special interest for industrial applications, its excellent wear resistance and good solderability. Moreover high catalytic activities for many chemical reactions make Pd interesting for electrocatalysis. Pd films on various noble metal surfaces like Au or Pt have been studied in aqueous electrolytes towards their catalytic activities e.g. the oxidation of carbon monoxide or formic acid [191–195]. The initial stages of Pd deposition on various single crystal surfaces like Au(111), Au(100) as well as Au(110) have been thoroughly investigated in aqueous electrolytes [80, 81, 196]. Only few studies exist on the electrodeposition of Pd from ionic liquids. Binary IL-mixtures based on $AlCl_3$ were used as electrolytes in early experiments [197, 198]. Recent studies are more focused on the deposition of Pd-alloys like Pd-Au, Pd-Ag and Pd-In [82, 83, 199]. Endres *et al.* reported the deposition of nanocrystalline Pd at elevated temperatures on a copper sheet from binary ionic liquid mixtures [200].

14.1 Deposition of Pd onto Au(111) from $BMIPF_6$

On Au(111) the pure $BMIPF_6$ has an electrochemical window of around 3 V (see chapter 10). The anodic limit of the potential window is determined by the oxidation of the gold substrate and/or anion oxidation whereas the cathodic limit marks the reduction of the $[BMI]^+$ cation. The ionic liquid was saturated with $PdCl_2$ and CVs were recorded with a low scan rate of 1 mV/s (Fig. 14.1). These conditions make it possible to study the Pd deposition in detail with all peaks in the CV well resolved. Noticeable reduction peaks can be seen, the most prominent one P_2 appearing at -250 mV. This cathodic peak is correlated with the formation of a first layer of Pd on the gold surface which could be observed with *in-situ* STM (see below). Two anodic peaks can be related to peak P_2. A big stripping peak (P_5) appears at around -100 mV, carrying a hardly discernible shoulder, a smaller stripping

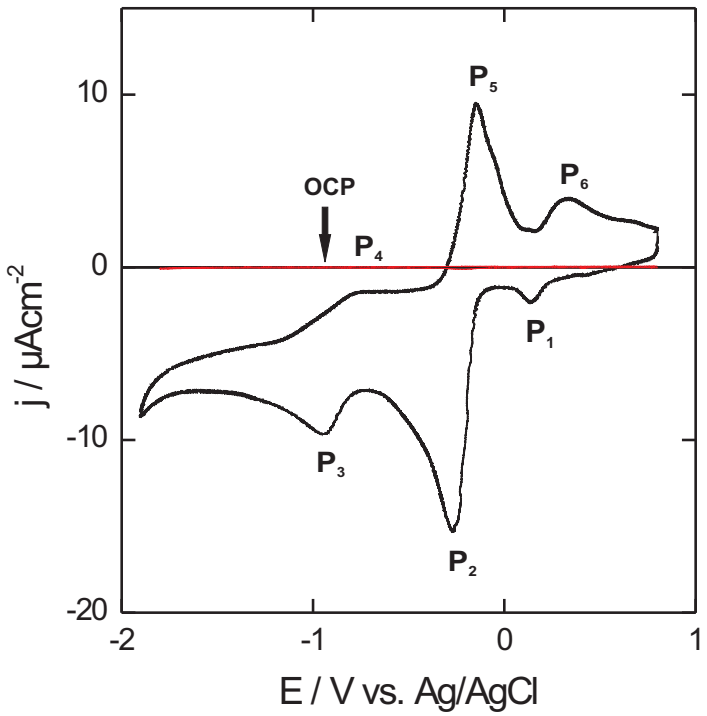

Figure 14.1: CV at 1 mV/s of $PdCl_2$ in $BMIPF_6$ on Au(111). Red line: Without $PdCl_2$ (the OCP is at -900 mV).

peak is located at around +400 mV (P_6). At -900 mV a second reduction process appears (P_3) which can be attributed to the formation of another Pd layer. The corresponding anodic peak P_4 is less pronounced and appears at -750 mV. Rising currents at around -1.8 V are related to the irreversible reduction of the organic cation. The determination of the equilibrium potential of Pd/Pd^{2+} in $BMIPF_6$ turned out to be at -900 mV which coincides with the potential of the second redox process (P_3, P_4). Therefore the cathodic peak at -250 mV can be identified as an under-potential deposition (UPD) of Pd on gold. A small cathodic peak P_1 at +200 mV, which is not this obvious in all experiments, might be due to an energetically heterogeneous surface. CV experiments in aqueous electrolytes show that Pd nucleation starts on steps at more positive potentials than the nucleation on flat terraces [80]. Comparing the CVs of the Pd deposition in $BMIPF_6$ with the Pd deposition in sulphuric acid solutions one can detect a big potential difference between the different reduction processes: In $BMIPF_6$ the difference in the peak potentials between the deposition of the first (UPD) and the second Pd layer is about 700 mV, approximately ten times larger than in aqueous electrolytes. Obviously Pd interacts much better with the gold substrate in $BMIPF_6$ than in aqueous electrolytes which can be understood taking into account that ions such as $[PF_6]^-$ and $[BF_4]^-$ are known to coordinate very weakly with metal ions [201]. Thus Pd^{2+} is not expected to have a solvation shell in $BMIPF_6$ and can be regarded as „naked“. The charge necessary for the deposition of a monolayer Pd is ca. 450 μCcm^{-2}. Integrating peak P_2 yields a charge which exceeds the value for a monolayer by far. Also the charges for the anodic processes (P_5, P_6) are much more than one would expect for the stripping of a Pd monolayer. Consequently another redox process is superimposed to the Pd deposition. A partial reduction of the cation during deposition of Pd is supposed, however, a safe explanation for the huge charge density cannot be offered at present.

The STM sequence in Fig. 14.2 illustrates initial stages of the Pd deposition onto Au(111) from a saturated solution of $PdCl_2$ in $BMIPF_6$. Fig. 14.2a shows a flat gold surface at -150 mV with no islands. Instead nucleation of small clusters can be seen as well as holes with a depth of 0.25 nm ± 0.05 nm. Although we suppose an unreconstructed gold surface at this potential, the absence of gold islands can be explained with an enhanced surface mobility of gold atoms caused by chloride. Experiments in aqueous electrolytes demonstrate a very efficient electrochemical annealing of the gold surface in the presence of chloride where islands disappear within a matter of seconds [202]. However in the presence of the strongly adsorbing $[PdCl_4]^{2-}$ complex a stabilization of the gold islands can be observed due to a suppressed surface diffusion [80]. In the case of $PdCl_2$ in $BMIPF_6$ no evidence of an $[PdCl_4]^{2-}$ ad-structure on the surface could be found. The holes point

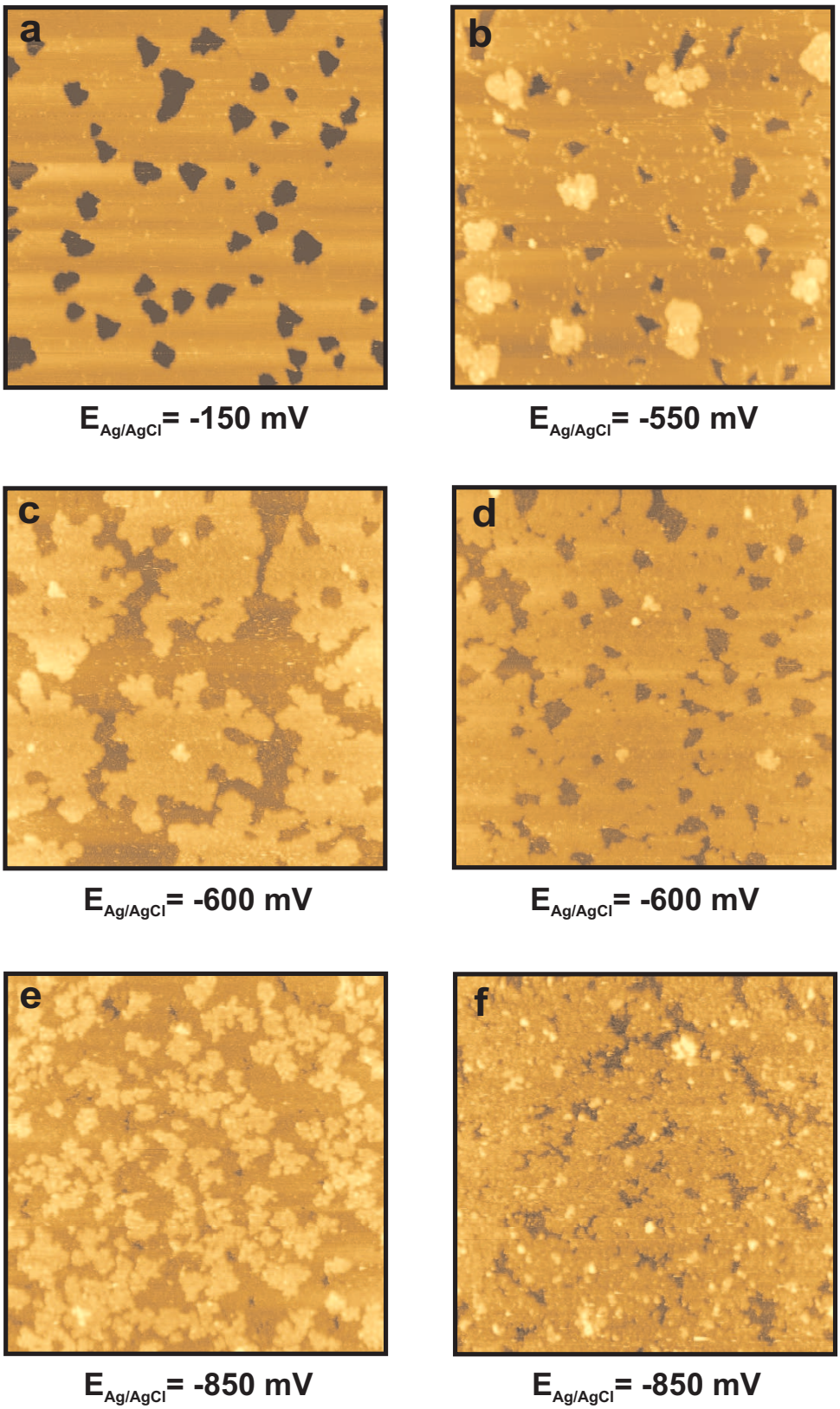

Figure 14.2: Sequence of 6 STM images (300 nm x 300 nm) showing the initial stages of Pd deposition onto Au(111) from a saturated solution of $PdCl_2$ in $BMIPF_6$; time between each STM image is about 5 minutes. Deposition potentials as indicated in the figures.

towards a much bigger surface mobility of gold atoms compared to aqueous electrolytes leading to a more open surface with an higher susceptibility for the Pd deposition. Holes on the surface probably due to surface etching could also be observed in case of Co deposition on Au(111) using $CoCl_2$ dissolved in $BMIBF_4$ [86]. Decreasing the potential to -550 mV Pd islands monoatomic in height appear (Fig. 14.2b). In addition growth of Pd clusters takes place preferentially at the edges of the holes which eventually disappear (Fig. 14.2c). Due to the high viscosity of the ionic liquid, associated with slow diffusion of metal ions to the surface, Pd islands develop in a fractal shape, finally growing together to form a monolayer (Fig. 14.2d). Thereby the Pd layer reproduces exactly the topography of the underlying Au(111) substrate. Little islands appear on top of the Pd islands just before completion of the first layer. No Moiré pattern was observed, suggesting a pseuomorphic growth. Decreasing the potential to -850 mV a second Pd layer commences to grow on the flat surface (Fig. 14.2e). Contrary to the first layer, the second layer starts with the formation of numerous small islands monoatomic in height. Ultimately the islands grow together completing the second layer, whilst an unordered cluster growth indicates deposition of further Pd (Fig. 14.2f). Throughout the Pd deposition no worm-like structure could be observed at negative potentials [139].

Results of stripping experiments of Pd are displayed in Fig. 14.3. Dissolution of the second Pd layer starts at the potential marked by peak P_4 in Fig. 14.1. At -350 mV stripping continues (Fig. 14.3a), followed by dissolution of the first layer at -150 mV (Fig. 14.3b, peak P_5 in Fig. 14.1). At +50 mV only small Pd clusters are left over from the first layer, scattered across the surface. Increasing the potential to +250 mV dissolution proceeds with the formation of holes on the gold surface (Fig. 14.3d, peak P_6 in Fig. 14.1). We ascribe this process to the dissolution of Pd previously deposited into the holes (see Fig. 14.2b). Thereby it is worth mentioning that the oxidation of the Au(111) substrate in pure $BMIPF_6$ is well known to occur beyond 1 V [203].

14.2 Deposition of Pd onto Au(100) from $BMIPF_6$

Fig. 14.4 shows a current-potential curve for $PdCl_2$ in $BMIPF_6$ on Au(100). The voltammetric features are very similar to those for Pd deposition on Au(111) (P_1-P_6). Metal deposition starts at -500 mV indicated by a large reduction peak (P_2). Compared to Au(111) a much bigger current density can be observed for this process which is related to a much faster monolayer deposition (see below). The potential of the redox process marked by peak P_3 and P_4 is again located at the equilibrium potential for Pd/Pd^{2+} on Au(100) in $BMIPF_6$ (approx. -1 V) and can be attributed to the deposition/dissolution of

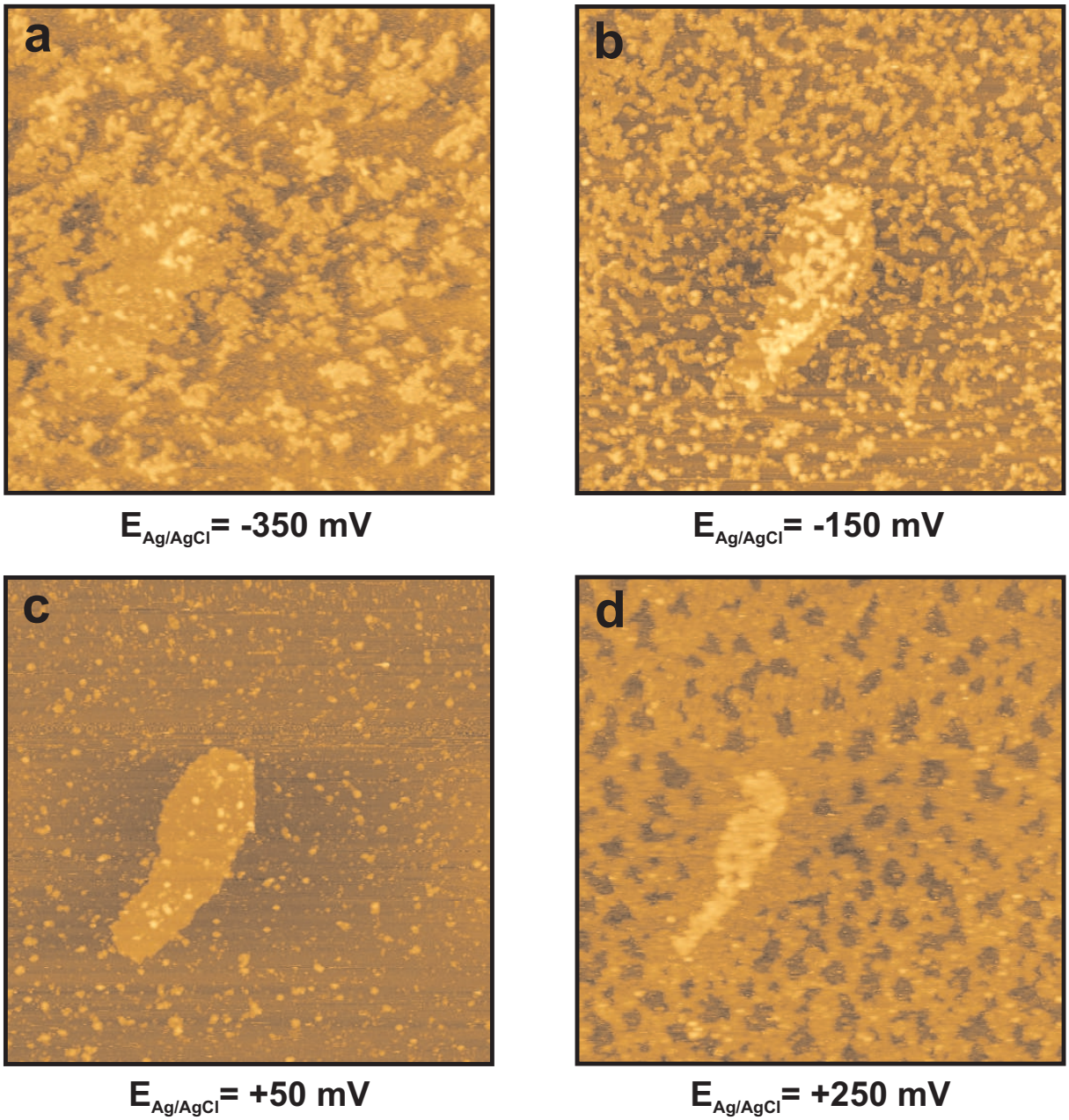

Figure 14.3: Sequence of STM images (250 nm x 250 nm) demonstrating dissolution of Pd on Au(111) in $BMIPF_6$.

Pd on top of the first layer. Therefore process P_2 can be regarded as an under-potential deposition (UPD) of palladium. The discrepancy between cathodic and anodic charge density is even more obvious for Au(100). The charge density for deposition of a pseudomorphic monolayer of Pd (370 μCcm^{-2}) is exceeded severalfold. Thus we suppose as in case for Au(111) another redox process superimposed to the metal deposition. Small shoulders on the positive side of the stripping peaks P_5 and P_6, located at -200 mV and +500 mV, respectively, can also be noticed. Peak P_1 is smeared out and not so distinctive as for Au(111). P_1 is probably related to the nucleation of Pd at defects such as steps.

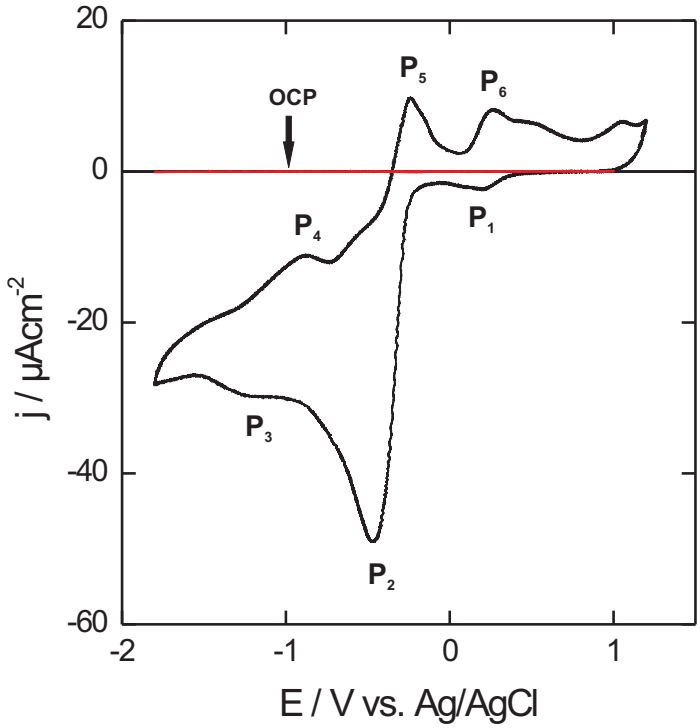

Figure 14.4: CV at 1 mV/s of $PdCl_2$ in $BMIPF_6$ on Au(100). Red line: Without $PdCl_2$. The OCP is at around -1 V.

Fig. 14.5 illustrates a series of 6 STM images of the Pd deposition on Au(100) from $BMIPF_6$. A gold surface rich in defects presumably caused by chloride can be seen in Fig. 14.5a prior metal deposition. Obviously the high mobility of the surface atoms yields an etched surface which is more pronounced as in case of Au(111). Due to the more open Au(100) surface an elevated diffusion of gold atoms on the surface can be expected. Few small gold islands might be relicts of the lifting of the Au(100) (hex)-reconstruction. No hints for an adsorbed $[PdCl_4]^{2-}$ complex could be found. Decreasing the potential

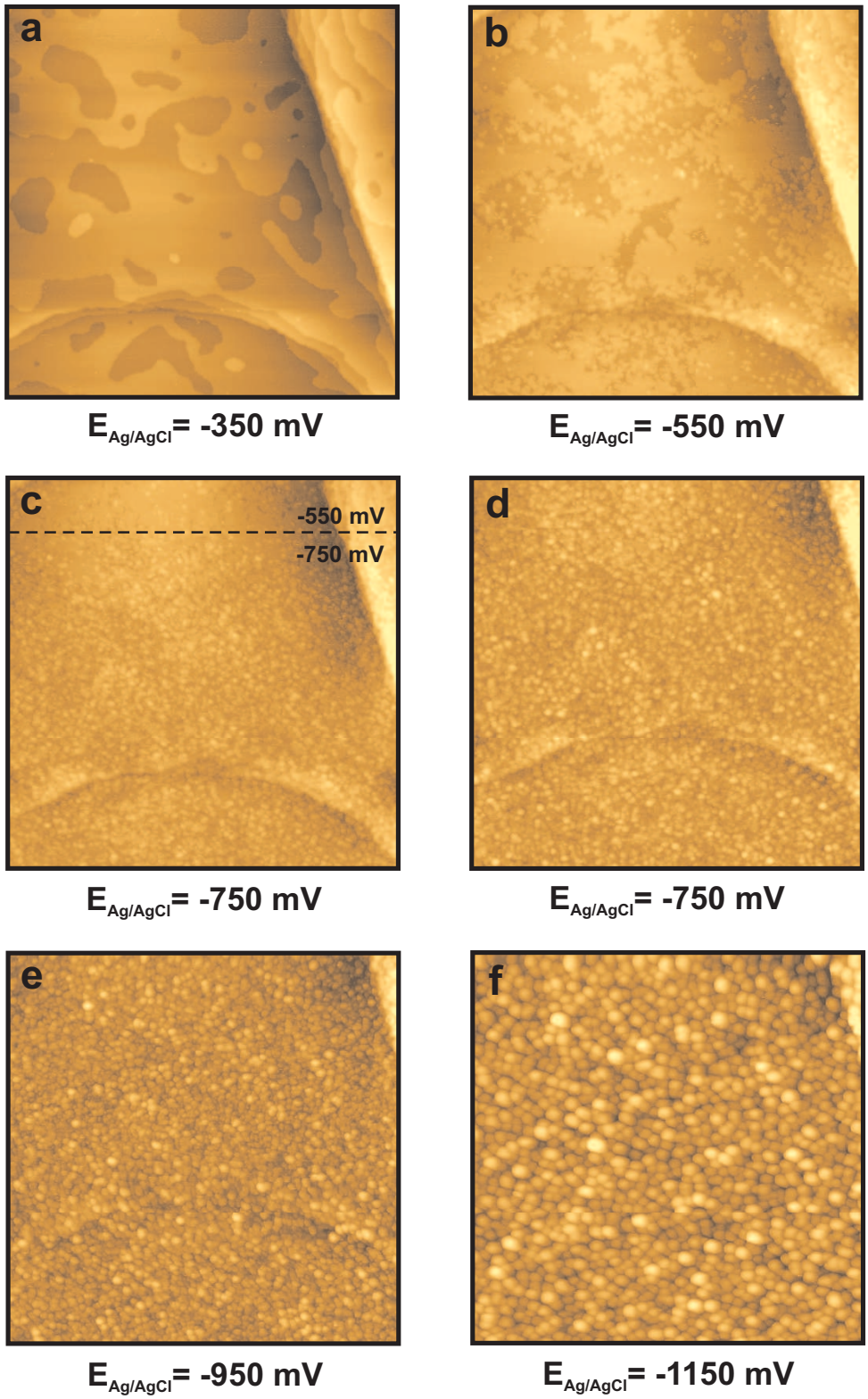

Figure 14.5: Sequence of 6 STM images (250 nm x 250 nm) showing the initial stages of Pd deposition onto Au(100) from a saturated solution of $PdCl_2$ in $BMIPF_6$; time between (a) and (b) as well as (c) and (d) is about 30 s. Time between (e) and (f) is about 3 minutes. Potentials as indicated in the figures.

to -550 mV the surface is rapidly covered with a Pd layer (Fig. 14.5b). It appears that Pd nucleates on step edges as well as on terraces forming small islands monoatomic in height which finally grow together. In contradiction to Au(111), where formation of the Pd monolayer takes minutes (typically 5 min. between each STM image in Fig. 14.2), here Pd deposition occurs within a few seconds. The growth mechanism resembles the deposition of the second Pd layer on island-covered Au(100) in sulphuric acid solution [81]. In Fig. 14.5c the potential was lowered to -750 mV. A rather quick growth of Pd clusters on the surface can be observed. The deposit has a disordered appearance, eventually covering the complete surface (Fig. 14.5d). Size growth of the clusters occurs at more negative potentials (Fig. 14.5e) which finally leads to a spherical cluster shape (Fig. 14.5f). A different morphology of the deposited Pd compared to aqueous electrolytes is stressed here. Pd grows more 3-dimensional in $BMIPF_6$ rather than growing layer-by-layer as observed in sulphuric acid solution. No hints were found for a cation row structure at negative potentials as recently observed for the pure $BMIPF_6$ on Au(100) [165].

The dissolution of Pd is shown in Fig. 14.6. At -950 mV spherical clusters can be seen on the surface (Fig. 14.6a). The clusters diminish in size during an increase of the potential to -50 mV (Fig. 14.6b). At +50 mV lots of small islands, remainders of the first Pd layer, as well as holes on the surface with a depth of 0.26 nm $\pm$ 0.05 nm can be noticed (Fig. 14.6c). The stripping peaks P_5 and P_6 in the CV (Fig. 14.4) are related to dissolution of the Pd clusters as well as the first Pd layer. Enhancing the potential to +250 mV the small islands disappear and the bare Au(100) surface emerges. Smoothed Au(100) terraces appear due to an electrochemical annealing at positive potentials, caused by chloride (Fig. 14.6d).

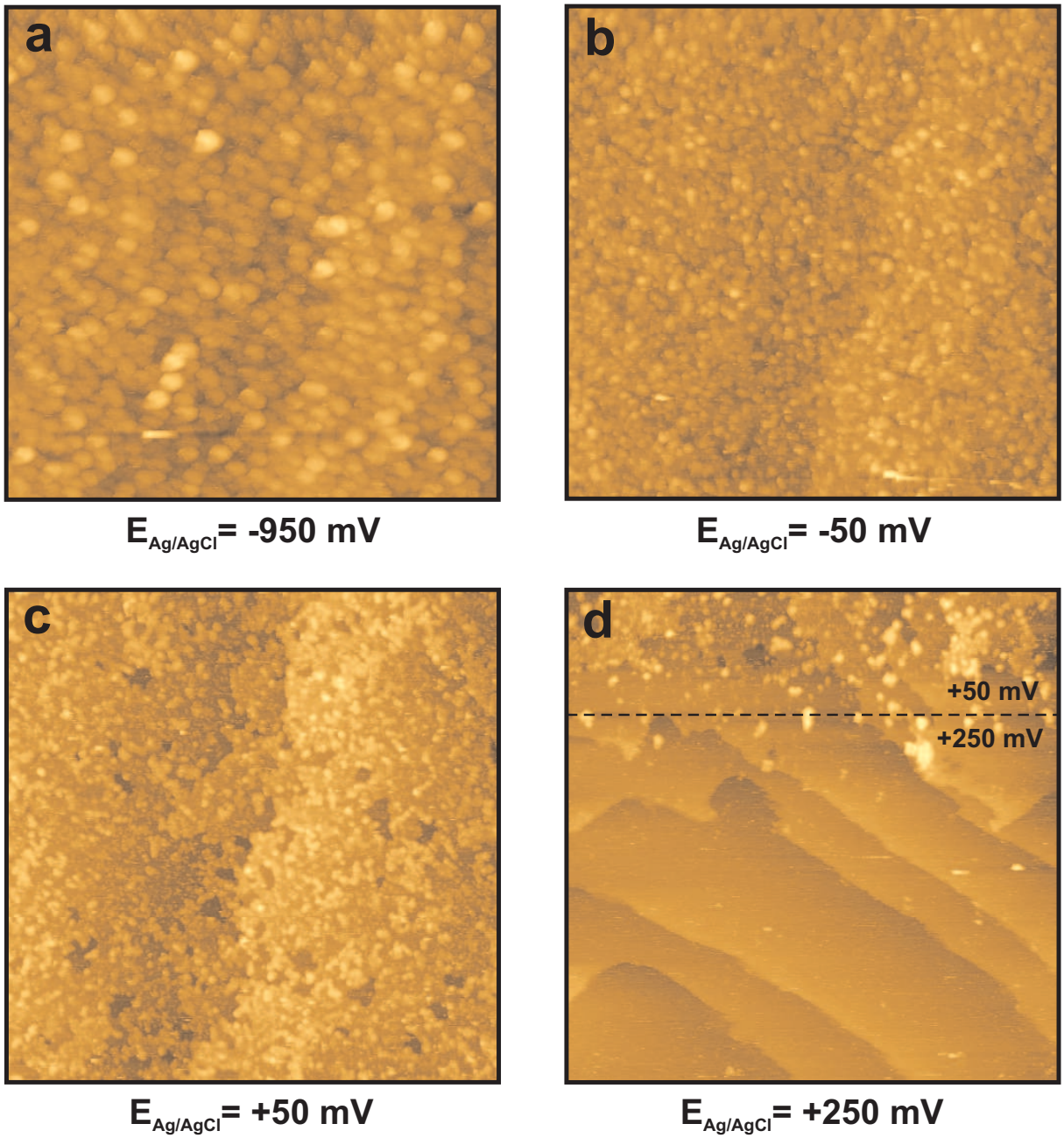

Figure 14.6: Sequence of STM images (250 nm x 250 nm) demonstrating dissolution of Pd on Au(100) in $BMIPF_6$ (scanrate: 10 mV/s).

15 Summary

The aim of this work was a better understanding of the interface between ionic liquids and well-defined gold surfaces on a molecular level. For this reason, methods such as cyclic voltammetry, impedance spectroscopy as well as *in-situ* scanning tunneling microscopy have been employed. In addition, *in-situ* STM studies were devoted to palladium deposition from ionic liquids.

- The CV of a Au(111) surface in contact with $BMIPF_6$ features a characteristic sharp cathodic peak and an associated broad, anodic hump. This feature is attributed to a slow rearrangement of the IL side of the double layer. The cathodic peak coincides with the *pztc*, as determined by immersion experiments, that is, the potential where the innermost layer changes from a cationic to an anionic layer with increasing potential. Structural changes can be seen positive and negative of the *pztc* in the STM images. A worm-like structure appears in the cathodic potential regime. Impedance spectra of Au(111) in $BMIPF_6$ can be fitted using an equivalent circuit given by a capacity in parallel to a constant phase element (CPE). The high-frequency value of the capacity – that is, the double layer capacitance – is about 6–7 μFcm^{-2}. The CPE coefficient peaks at a potential, which coincides with the pztc. The slow rearrangement processes manifest themselves as CPE playing the role of the double layer capacitance. The CPE expresses the kinetics of the re-structuring of the interfacial region.

- Purification of ionic liquids is an important step before using them for electrochemical measurements. Since ILs are liquids with very low vapour pressures, cleaning e.g. by distillation is difficult, if not impossible, considering their thermal stability range. In search for an alternative cleaning method the influence of molecular sieves of different pore sizes on the cyclovoltammetric behaviour of Au(111) in $BMIPF_6$ was tested. In order to obtain reproducible CVs with double layer behaviour, the use of molecular sieves with a pore size of 0.3 nm is recommended. Molecular sieves with larger pore sizes do not purify the ionic liquid adequately; on the contrary they seem to contaminate it. Because of the high viscosity of the ionic liquid the

purification process is slow. Therefore it is suggested to keep the molecular sieve in contact with the liquid for at least 72 h. The distinctive cathodic peak seems unaffected by the purification, indicating a $BMIPF_6$-characteristic interaction with the gold substrate. This feature may serve as a landmark for calibrating reference electrodes.

- The electrochemical interface of Au(100) in $BMIPF_6$ has been characterized by cyclic voltammograms, electrochemical impedance spectroscopy and *in-situ* STM. Cyclic voltammetry on a sensitive current scale clearly shows that the double layer region of Au(100) in $BMIPF_6$ is by no means flat but exhibits characteristic cathodic peaks with broad anodic counterparts. By means of immersion experiments the *pztc* was determined. It is located within the dominant cathodic peak in the CV. Here the rearrangement of the double layer occurs whereupon the anions change with the cations during cathodic excursion. The capacitance spectra in this potential region are of two-arc shape, which can be interpreted in such a way that the two ions constituting the IL are adsorbed on the metal surface; the adsorption/desorption processes are slow; their activation energy is similar to that of the bulk conductivity. The high frequency capacitance shows a much smaller dependence on electrode potential than predicted by current theories. An ordered row-structure of the $[BMI]^+$ cation is observed at negative potentials. The Au(100) (hex)-reconstruction appears in the cathodic region of the cation breakdown.

- In order to investigate the influence of the anion on electrochemical properties the $[PF_6]^-$ was changed against the larger, more sterically hindered $[Tf_2N]^-$ ion. Reproducible CVs with a double layer region and a pronounced cathodic hump were obtained. The impedance spectra can be fitted using an equivalent circuit containing CPEs. The high-frequency value of the capacity (double layer capacitance) is comparable with values obtained for Au(100) in $BMIPF_6$ and again independend of the potential. With the *in-situ* STM the same surface structures in the cathodic potential range can be seen as for Au(100) and Au(111) in $BMIPF_6$ (worm-like structure and row-structure). These ad-structures are caused by the $[BMI]^+$ cations.

- In the non-aromatic, guanidinium-based IL $Bu_2Et_2Me_2GuanTf_2N$ a broad (at room temperature 3 V wide) potential range of ideal polarizability can be observed. In this range the double layer charging is very slow; the equivalent circuit of the interface consists of three branches. The very low value of the high frequency capacitance is in accord with the large size of ions of the electrolyte. *In-situ* STM experiments at

negative potentials show the formation of the (hex)-reconstruction and herringbone reconstruction on Au(100) and Au(111), respectively. Since no organized cation interfacial layer (row-structure on Au(100) and worm-like structure on Au(111)) could be observed, it is concluded that the guanidinium cation is not able to form a stable ad-structure on gold. The possible reason of the weakness of the guanidinium-gold interactions might be the lack of an aromatic π-system as well as sterical hindrance.

- Pd deposition on Au(111) and Au(100) from $BMIPF_6$ starts with the formation of a monolayer Pd (i.e. it is a UPD process). Nucleation of Pd islands on the terraces could be observed for both substrates. In case of Au(111) holes cover the surface whereas Pd islands grow in a fractal shape, for Au(100) even bigger defects are observable prior metal deposition probably due to a chloride induced elevation of the surface mobility of Au atoms. Neither on Au(111) nor on Au(100) hints for an adsorbed $[PdCl_4]^{2-}$ complex could be found. Also no worm-like structure on Au(111) and no cation row-stucture on Au(100) has been noticed with the *in-situ* STM at negative potentials. For Au(111) metal deposition proceeds with the formation of a second Pd layer. On Au(100), however, formation of the first Pd layer is followed by an unordered cluster growth which differentiate in morphology from Pd deposition in sulphuric acid solutions. Pd exhibits a more 3-dimensional growth behaviour on Au(100) compared to Pd on Au(111).

Finally, it can be concluded that unique properties such as broad electrochemical windows, vanishing low vapor pressures, and the air- and water-stability make ILs promising electrolytes for the future. Still challenging issues are the deposition of less noble metals like lithium or magnesium which are important metals for battery research and energy storage. Ion adsorption at the electrode/ionic liquid interface make the interfacial structure much more complicated than in aqueous solutions. The employment of scanning probe and spectroscopic techniques in order to get structural information with high spatial resolution on the molecular level is essential for a detailed understanding of the electrode/ionic liquid interfaces. An appropriate theory which describes issues such as differential capacitance curves and their correlation with the potential of zero charge is still missing. Thus, in the future the combination of theoretical modeling with experimental results will lead to adequate applications of ionic liquids in electrochemistry.

Bibliography

[1] D. R. MacFarlane, K. R. Seddon, *Aust. J. Chem.* **60** (2007) 3.

[2] P. Wasserscheid, T. Welton, *Ionic Liquids in Synthesis*, Wiley-VCH, Weinheim (2003).

[3] T. Welton, *Chem. Rev.* **99** (1999) 2071.

[4] N. V. Plechkova, K. R. Seddon, *Chem. Soc. Rev.* **37** (2008) 123.

[5] P. Walden, *Bull. Acad. Imper. Sci.* (1914) 405.

[6] F. H. Hurley, T. P. Wier, Jr., *J. Electrochem. Soc.* **98** (1951) 207.

[7] J. S. Wilkes, M. J. Zaworotko, *J. Chem. Soc. Chem. Comm.* (1992) 965.

[8] A. Wieckowski (ed.), M. Dekker (Eds.), *Interfacial Electrochemistry: Theory, Experiment and Applications*, *Part II: Electrochemical Surface Science*, New York (1999).

[9] H. Helmholtz, *Ann. d. Phys. u. Chem. N. F. VII* **7** (1879) 337.

[10] J. O'M. Bockris, M. A. Devanathan, K. Müller, *Proc. R. Soc. London A* **274** (1963) 55.

[11] D. M. Kolb, *Angew. Chem. Int. Ed.* **40** (2001) 1162.

[12] A. A. Kornyshev, *J. Phys. Chem. B* **111** (2007) 5545.

[13] K. B. Oldham, *J. Electroanal. Chem.* **613** (2008) 131.

[14] A. N. Frumkin, O. A. Petrii, B. B. Damaskin in J. O'M Bockris, B. E. Conway, E. Yeager, *Comprehensive Treatise of Electrochemistry*, Vol. 1, Plenum Press, New York (1980).

[15] V. Jendrašić, *J. Electroanal. Chem.* **22** (1969) 157.

[16] W. Schmickler, *Interfacial Electrochemistry*, Oxford University Press, New York, Oxford (1996).

[17] S. Trasatti in: H. Gerischer, C. W. Tobias, *Advances in Electrochemistry and Electrochemical Engeneering*, Vol. 10, John Wiley & Sons (1977) 213.

[18] S. Trasatti in: A. F. Silva, *Trends in Interfacial Electrochemistry*, D. Reidel Publishing Company, Dordrecht, Boston (1986) 25.

[19] G. A. Somorjai, M. A. Van Hove, *Prog. Surf. Sci.* **30** (1989) 201.

[20] A. S. Dakkouri, Dissertation, Universität Ulm (1996).

[21] M. Kleinert, Dissertation, Universität Ulm (2001).

[22] J. Schneider, D. M. Kolb, *Surf. Sci.* **193** (1988) 579.

[23] D. M. Kolb, *Prog. Surf. Sci.* **51** (1996) 109.

[24] K. R. Seddon, *J. Chem. Tech. Biotechnol.* **68** (1997) 351.

[25] K. R. Seddon, *Kinet. Catal. Engl. Transl.* **37** (1996) 693.

[26] J. S. Wilkes, J. A. Levisky, R. A. Wilson, C. L. Hussey, *Inorg. Chem.* **21** (1982) 1263.

[27] J. Robinson, R. A. Osteryoung, *J. Am. Chem. Soc.* **101** (1979) 323.

[28] P. Bonhôte, A.-P. Dias, N. Papageorgiou, K. Kalyanasundaram, M. Grätzel, *Inorg. Chem.* **35** (1996) 1168.

[29] P. A. Z. Suarez, J. E. L. Dullius, S. Einloft, R. F. de Souza, J. Dupont, *Polyhedron* **15** (1996) 1217.

[30] J. L. Anthony, E. J. Maginn, J. F. Brennecke, *J. Phys. Chem. B* **105** (2001) 10942.

[31] C. Villagrán, M. Deetlefs, W. R. Pitner, C. Hardacre, *Anal. Chem.* **76** (2004) 2118.

[32] P. Wasserscheid, W. Keim, *Angew. Chem. Int. Ed.* **39** (2000) 3772.

[33] K. R. Seddon, *Nature Mater.* **2** (2003) 363.

[34] H. Kunkel, Dissertation, Universität Ulm (2008).

[35] H. Kunkel, G. Maas, *Eur. J. Org. Chem.* (2007) 3746.

[36] J. D. Holbrey, K. R. Seddon, *J. Chem. Soc., Dalton Trans.* (1999) 2133.

[37] H. L. Ngo, K. LeCompte, L. Hargens, A. B. McEwen, *Thermochim. Acta* **357-348** (2000) 97.

[38] S. Arimoto, D. Oyamatsu, T. Torimoto, S. Kuwabata, *Chem. Phys. Chem* **9** (2008) 763.

[39] S. Arimoto, M. Sugimura, H. Kageyama, T. Torimoto, S. Kuwabata, *Electrochim. Acta* **53** (2008) 6228.

[40] M. J. Earle, J. M. S. S. Esperança, M. A. Gilea, J. N. C. Lopes, L. P. N. Rebelo, J. W. Magee, K. R. Seddon, J. A. Widegren, *Nature* **439** (2006) 831.

[41] D. Strasser, F. Goulay, M. S. Kelkar, E. J. Maginn, S. R. Leone, *J. Phys. Chem. A* **111** (2007) 3191.

[42] C. Wakai, A. Oleinikova, M. Ott, H. Weingärtner, *J. Phys. Chem. B* **109** (2005) 17028.

[43] L. C. Branco, J. N. Rosa, J. J. Moura Ramos, C. A. M. Alfonso, *Chem. Eur. J.* **8** (2002) 3671.

[44] A. E. Visser, R. P. Swatolski, W. M. Reichert, S. T. Griffin, R. D. Rogers, *Ind. Eng. Chem. Res.* **39** (2000) 3596.

[45] F. Endres, D. MacFarlane, A. Abbott, *Electrodeposition from Ionic Liquids*, Wiley-VCH, Weinheim, (2008), p. 67.

[46] M. Galiński, A. Lewandowski, I. Stępniak, *Electrochim. Acta* **51** (2006) 5567.

[47] Y. Katayama, *Electrochemical Aspects of Ionic Liquids*, John Wiley and Sons, Inc., New York (2005), chapter 3.

[48] D'Ans-Lax, *Taschenbuch für Chemiker und Physiker, Physikalisch-chemische Daten, Band 1*, Springer Verlag, Berlin-Göttingen-Heidelberg (1992), p. 476.

[49] R. Mills, *J. Phys. Chem.* **77** (1973) 685.

[50] H. A. Every, A. G. Bishop, D. R. MacFarlane, G. Orädd, M. Forsyth, *Phys. Chem. Chem. Phys.* **6** (2004) 1758.

[51] S. Carda-Broch, A. Berthod, A. W. Armstrong, *Anal. Bioanal. Chem.* **375** (2003) 191.

[52] H. Tokuda, S. Tsuzuki, M. A. B. H. Susan, K. Hayamizu, M. Watanabe, *J. Phys. Chem. B* **110** (2006) 19593.

[53] J. N. Barisci, G. G. Walace, D. R. MacFarlane, R. H. Baughman, *Electrochem. Comm.* **6** (2004) 22.

[54] T. Nishida, Y. Tashiro, M. Yamamoto, *J. Fluorine Chem.* **120** (2003) 135.

[55] P. A. Z. Suarez, S. Einloft, J. E. L. Dullius, R. F. de Souza, J. Dupont, *J. Chim. Phys. Chim. Biol.* **95** (1998) 1626.

[56] A. Lewandowski, I. Stępniak, *Phys. Chem. Chem. Phys.* **5** (2003) 4215.

[57] D. R. MacFarlane, P. Meakin, J. Sun, N. Amini, M. Forsyth, *J. Phys. Chem. B* **103** (1999) 4164.

[58] T. Yim, H. Y. Lee, H.-J. Kim, J. Mun, S. Kim, S. M. Oh, Y. G. Kim, *Bull. Korean Chem. Soc.* **28** (2007) 1567.

[59] H. Sakaebe, H. Matsumoto, *Electrochem. Comm.* **5** (2003) 594.

[60] G. S. Owens, M. M. Abu-Omar, *J. Mol. Cat. A: Chem.* **187** (2002) 215.

[61] A. Noda, M. Watanabe, *Electrochim. Acta* **45** (2000) 1265.

[62] J. Fuller, R. T. Carlin, H. C. De Long, D. Haworth, *J. Chem. Soc. Chem. Commun.* (1994) 299.

[63] A. Noda, K. Hayamizu, M. Watanabe, *J. Phys. Chem. B* **105** (2001) 4603.

[64] D. R. MacFarlane, J. Sun, J. Golding, P. Meakin, M. Forsyth, *Electrochim. Acta.* **45** (2000) 1271.

[65] A. R. Choudhury, N. Winterton, A. Steiner, A. I. Cooper, K. A. Johnson, *J. Am. Chem. Soc.* **127** (2005) 16792.

[66] F. Castiglione, M. Moreno, G. Raos, A. Famulari, A. Mele, G. Battista Appetecchi, S. Passerini, *J. Phys. Chem. B* **113** (2009) 10750.

[67] K. Fujii, T. Nonaka, Y. Akimoto, Y. Umebayashi, S.-I. Ishiguro, *Anal. Sci.* **24** (2008) 1377.

[68] F. Endres, A. Schweizer, *Phys. Chem. Chem. Phys.* **2** (2000) 5455.

[69] R. T. Carlin, H. C. De Long, J. Fuller, P. C. Trulove, *J. Electrochem. Soc.* **145** (1998) 1598.

[70] D. Auerbach, Z. Lu, A. Schechter, Y. Gofer, H. Gizbar, R. Turgeman, Y. Cohen, M. Moshkovich, E. Levi, *Nature* **407** (2000) 724.

[71] O. Chusid, Y. Gofer, H. Gizbar, Y. Vestfried, E. Levi, D. Auerbach, *Adv. Mat.* **15** (2003) 627.

[72] G. T. Cheek, W. E. O'Grady, S. Zein El Abedin, E. M. Moustafa, F. Endres, *J. Electrochem. Soc.* **155** (2008) D91.

[73] S. Zein El Abedin, U. Welz-Biermann, F. Endres, *Electrochem. Comm.* **7** (2005) 941.

[74] S. Zein El Abedin, H. K. Farag, E. M. Moustafa, U. Welz-Biermann, F. Endres, *Phys. Chem. Chem. Phys.* **7** (2005) 2333.

[75] F. Endres, S. Zein El Abedin, A. Y. Saad, E. M. Moustafa, N. Borissenko, W. E. Price, G. G. Wallace, D. R. MacFarlane, P. J. Newmanc, A. Bund, *Phys. Chem. Chem. Phys.* **10** (2008) 2189.

[76] A.F. Holleman, N. Wiberg, *Lehrbuch der anorganischen Chemie*, 91.-100. Auflage, Walter de Gruyter, Berlin, New York (1985)

[77] R. J. Randler, D. M. Kolb, B. M. Ocko, I. K. Robinson, *Surf. Sci.* **447** (2000) 187.

[78] M. Dietterle, T. Will, D. M. Kolb, *Surf. Sci.* **396** (1998) 189.

[79] S. Zein El Abedin, A. Y. Saad, H. K. Farag, N. Borissenko, Q. X. Liu, F. Endres, *Electrochim. Acta* **52** (2007) 2746.

[80] L. A. Kibler, M. Kleinert, R. Randler, D. M. Kolb, *Surf. Sci.* **443** (1999) 19.

[81] L. A. Kibler, M. Kleinert, D. M. Kolb, *Surf. Sci.* **461** (2000) 155.

[82] C.-C. Tai, F.-Y. Su, I.-W. Sun, *Electrochim. Acta* **50** (2005) 5504.

[83] F.-Y. Su, J.-F. Huang, I.-W. Sun, *J. Electrochem. Soc.* **151** (2004) C811.

[84] Y.-M. Wei, Y.-C. Fu, J.-W. Yan, C.-F. Sun, Z. Shi, Z.-X. Xie, D.-Y. Wu, B.-W. Mao, *J. Am. Chem. Soc.* **132** (2010) 8152.

[85] Y.-M. Wei, X.-S. Zhou, J.-G. Wang, J. Tang, B.-W. Mao, D. M. Kolb, *Small* **4** (2008) 1355.

[86] L.-G. Lin, J.-W. Yan, Y. Wang, Y.-C. Fu, B.-W. Mao, *J. Exp. Nanosci.* **1** (2006) 269.

[87] F. Endres, S. Z. El Abedin, *Phys. Chem. Chem. Phys.* **4** (2002) 1649.

[88] N. Borisenko, S. Zein El Abedin, F. Endres, *J. Phys. Chem. B* **110** (2006) 6250.

[89] S. Z. El Abedin, N. Borissenko, F. Endres, *Electrochem. Comm.* **6** (2004) 510.

[90] R. Al-Salman, J. Mallet, M. Molinari, P. Fricoteaux, F. Martineau, M. Troyon, S. Z. El Abedin, F. Endres, *Phys. Chem. Chem. Phys.* **10** (2008) 6233.

[91] M. Armand, F. Endres, D. R. MacFarlane, H. Ohno, B. Scrosati, *Nat. Mater.* **8** (2009) 621.

[92] J. Heinze, *Angew. Chem.* **96** (1984) 823.

[93] B. Speiser, *Chemie in unserer Zeit* **15** (1981) 62.

[94] A. J. Bard, L. R. Faulkner, *Electrochemical Methods: Fundamentals and Applications*, John Wiley & Sons, New York (1980).

[95] E. Barsoukov, J. R. Macdonald (ed), *Impedance Spectroscopy. Theory, Experiment and Applications*, Wiley (2005).

[96] T. Pajkossy, *J. Electroanal. Chem.* **364** (1994) 111.

[97] W. H. Mulder, J. H. Sluyters, T. Pajkossy, I. Nyikos, *J. Electroanal. Chem.* **285** (1990) 103.

[98] C.-H. Kim, S.-I. Pyun, J.-H. Kim, *Electrochim. Acta* **48** (2001) 3455.

[99] C. A. Schiller, W. Strunz, *Electrochim. Acta* **46** (2001) 3619.

[100] J.-B. Jorcin, M. E. Orazem, N. Pébère, B. Tribollet, *Electrochim. Acta* **51** (2006) 1473.

[101] B. Hirschorn, M. E. Orazem, B. Tribollet, V. Vivier, I. Frateur, M. Musiani, *Electrochim. Acta* **55** (2010) 6218.

[102] R. Ershler, *Disc. Farad. Soc.* **1** (1947) 269.

[103] A. N. Frumkin, V. I. Melik-Gaykasyan, *Dokl. Akad. Nauk.* **5** (1951) 855.

[104] W. Lorenz, *Z. Elektrochem.* **62** (1958) 192.

[105] B. A. Boukamp, *Solid State Ionics* **31** (1986) 20.

[106] M. Urquidi-Macdonald, S. Real, D. D. Macdonald, *Electrochim. Acta* **35** (1990) 1559.

[107] G. Binnig, H. Rohrer, *Helv. Phys. Acta* **55** (1982) 726.

[108] G. Binning, H. Rohrer, Ch. Gerber, E. Weibel, *Phys. Rev. Lett.* **49** (1982) 57.

[109] G. Binnig, H. Rohrer, *Rev. Mod. Phys.* **71** (1999) S324.

[110] R. Wiesendanger, *Scanning Probe Microscopy and Spectroscopy*, Cambridge University Press, Cambridge (1994).

[111] G. Binnig, H. Rohrer, *Angew. Chem.* **99** (1987) 622.

[112] D. M. Kolb in: *Advances in Electrochemical Science and Engineering*, Volume 7, R. C. Alkire, D. M. Kolb (eds.), Wiley-VCH, Weinheim (2002).

[113] T. Fließbach, *Quantenmechanik*, 3. Aufl., Spektrum Akademischer Verlag, Heidelberg (2000).

[114] J. Bardeen, *Phys. Rev. Lett.* **6** (1961) 57.

[115] J. G. Simmons, *J. Appl. Phys.* **34** (1963) 1793.

[116] R. J. Behm in: *Scanning Tunneling Microscopy and Related Methods*, R. J. Behm, M. García, H. Rohrer (eds.), NATO ASI, E184, Kluwer, Dordrecht (1990).

[117] J. Tersoff, D. R. Hamann, *Phys. Rev. B* **31** (1985) 805.

[118] P. K. Hansma, J. Tersoff, *J. Appl. Phys.* **61** (1987) R1.

[119] G. E. Engelmann, J. C. Ziegler, D. M. Kolb, *Surf. Sci. Lett.* **401** (1998) L420.

[120] G. Binnig, N. García, H. Rohrer, J. M. Soler, F. Flores, *Phys. Rev. B* **30** (1984) 4816.

[121] A. Bryant, D. P. E. Smith, C. F. Quate, *Appl. Phys. Lett.* **48** (1986) 832.

[122] R. Sonnenfeld, P. K. Hansma, *Science* **232** (1986) 211.

[123] B. Drake, R. Sonnenfeld, J. Schneir, P. K. Hansma, *Surf. Sci.* **181** (1987) 92.

[124] R. Christoph, H. Siegenthaler, H. Rohrer, H. Wiese, *Electrochim. Acta* **34** (1989) 1011.

[125] T. Will, M. Dietterle, D. M. Kolb, in: *Nanoscale Probes of the Solid/Liquid Interface*, NATO-ASI, Vol. E288, A. A. Gewirth and H. Siegenthaler (eds.), Kluwer, Dordrecht (1995) 137.

[126] T. Pajkossy, D. M. Kolb, *Electrochim. Acta* **53** (2008) 7403.

[127] D. W. Pohl, *IBM J. Res. Develop.* **30** (1986) 417.

[128] D. M. Kolb, M. Dietterle, T. Will, GDCh-Monographie, Bd. 3, GDCh, Frankfurt (1996) 19.

[129] M. A. Schneeweiß, Dissertation, Universität Ulm (1997).

[130] J. Winterlin, Dissertation, Freie Universität Berlin (1988).

[131] R. Nyffenegger, Diplomarbeit, Universität Bern (1990).

[132] L. A. Kibler, *Int. Soc. Electrochem.* (2003). Available from: <www.uni-ulm.de/echem/index.html?id=1023001>.

[133] A. Hamelin, *J. Electroanal. Chem.* **407** (1996), 1.

[134] A. Cuesta, L. A. Kibler, D. M. Kolb, *J. Electroanal. Chem.* **466** (1999) 165.

[135] A. M. El-Aziz, L. A. Kibler, *Electrochem. Commun.* **4** (2002) 866.

[136] J. Howarth, K. Hanlon, D. Fayne, P. McComac, *Tetrahedron Lett.* **38** (1997) 3097.

[137] U. W. Hamm, D. Kramer, R. S. Zhai, D. M. Kolb, *J. Electroanal. Chem.* **414** (1996) 85.

[138] A. S. Dakkouri, D. M. Kolb, in: A. Wieckowski, M. Dekker (Eds.), *Interfacial Electrochemistry: Theory, Experiment and Applications*, New York (1999) p. 151.

[139] L. G. Lin, Y. Wang, J. W. Yan, Y. Z. Yuan, J. Xiang, B. W. Mao, *Electrochem. Commun.* **5** (2003) 995.

[140] R. Atkin, S. Z. El Abedin, R. Hayes, L. H. S. Gasparotto, N. Borisenko, F. Endres, *J. Phys. Chem. C* **113** (2009) 13266.

[141] R. Atkin, G. G. Warr, *J. Phys. Chem. C* **111** (2007) 5162.

[142] C. Müller, Diplomarbeit, Universität Ulm (2010).

[143] R. Pauliukaite, A. P. Doherty, K. D. Murnaghan, C. M. A. Brett, *J. Electroanal. Chem.* **616** (2008) 14.

[144] M. T. Alam, Md. M. Islam, T. Okajima, T. Ohsaka, *Electrochem. Commun.* **9** (2007) 2370.

[145] Md. M. Islam, M. T. Alam, T. Okajiama, T. Ohsaka, *J. Phys. Chem. C* **113** (2009) 3386.

[146] V. Lockett, R. Sedev, J. Ralston, M. Horne, T. Rodopoulos, *J. Phys. Chem. C* **112** (2008) 7486.

[147] F. Silva, C. Gomes, M. Figueiredo, R. Costa, A. Martins, C. M. Pereira, *J. Electroanal. Chem.* **622** (2008) 153.

[148] N. Ibl, in: E. Yeager, J. O'M. Bockris, B. E. Conway, S. Sarangapani (Eds.), *Comprehensive Treatise of Electrochemistry*, Vol. 6, Plenum Press, New York (1983) p. 239.

[149] S. H. Glarum, J. H. Marshall, *J. Electrochem. Soc* **126** (1979) 424.

[150] F. Endres, S. Zein El Abedin, *Phys. Chem. Chem. Phys.* **8** (2006) 2101.

[151] S. Rivera-Rubero, S. Baldelli, *J. Phys. Chem. B* **108** (2004) 15133.

[152] G.-B. Pan, W. Freyland, *Chem. Phys. Lett.* **427** (2006) 96.

[153] U. Schröder, J. D. Wadhawan, R. G. Compton, F. Marken, P. A. Z. Suarez, C. S. Consorti, R. F. de Souza, J. Dupont, *New J. Chem.* **24** (2000) 1009.

[154] P. Nockemann, K. Binnemans, K. Driesen, *Chem. Phys. Lett.* **415** (2005) 131.

[155] M. J. Earle, C. M. Gordon, N. V. Plechkova, K. R. Seddon, T. Welton, *Anal. Chem.* **79** (2007) 758.

[156] B. K. Sweeny, D. G. Peters, *Electrochem. Commun.* **3** (2001) 712.

[157] Y. Chauvin, L. Mussmann, H. Olivier, *Angew. Chem. Int. Ed. Engl.* **34** (1995) 2698.

[158] F. Endres, S. Zein El Abedin, N. Borissenko, *Z. Phys. Chem.* **220** (2006) 1377.

[159] M. C. Kroon, W. Buijs, C. J. Peters and G.-J. Witkamp, *Green Chem.* **8** (2006) 241.

[160] M. T. Alam, Md. M. Islam, T. Okajima and T. Ohsaka, *J. Phys. Chem. C* **112** (2008) 16600.

[161] C. Aliaga, S. Baldelli, *J. Phys. Chem. B* **110** (2006) 18481.

[162] D. M. Kolb, J. Schneider, *Electrochim. Acta* **31** (1986) 929.

[163] T. Pajkossy and D. M. Kolb, *Electrochem. Commun.* **13** (2011) 284.

[164] T. Pajkossy and D. M. Kolb, *Electrochim. Acta* **54** (2009) 3594.

[165] Y.-Z. Su, Y.-C. Fu, J.-W. Yan, Z.-B. Chen, B.-W. Mao, *Angew. Chem.* **121** (2009) 5250.

[166] F. Endres, O. Höfft, N. Borisenko, L. H. Gasparotto, A. Prowald, R. Al-Salman, T. Carstens, R. Atkin, A. Bund, S. Zein El Abedin, *Phys. Chem. Chem. Phys.* **12** (2010) 1724.

[167] S. Baldelli, *Acc. Chem. Res.* **41** (2008) 421.

[168] D. M. Kolb, *Angew. Chem.* **113** (2001) 1198.

[169] W. Kantlehner, E. Haug, W. W. Mergen, P. Speh, T. Maier, J. J. Kapassakalidis, H.-J. Bräuner, H. Hagen, *Liebigs Ann. Chem.* (1984) 108.

[170] a) N. M. M. Mateus, L. C. Branco, N. M. T. Lourenço, C. A. M. Afonso, *Green Chem.* **5** (2003) 347. b) P. S. Kulkarni, L. C. Branco, J. G. Crespo, M. C. Nunes, A. Raymundo, C. A. M. Afonso, *Chem. Eur. J.* **13** (2007) 8478. c) A. A. Rosatella, L. C. Branco, C. A. M. Afonso, *Green Chem.* **11** (2009) 1406.

[171] M. G. Bogdanov, D. Petkova, S. Hristeva, I. Svinyarov, W. Kantlehner, *Z. Naturforsch.* **65b** (2010) 37.

[172] G. V. S. M. Carrera, L. C. Branco, J. Aires-de-Sousa, C. A. M. Afonso, *Tetrahedron* **64** (2008) 2216.

[173] M. G. Bogdanov, I. Svinyarov, H. Kunkel, C. Steinle, M. Arkhipova, W. Kantlehner, G. Maas, *Z. Naturforsch.* **65b** (2010) 791.

[174] S. Li, Y. Lin, H. Xie, S. Zhang, J. Xu, *Org. Lett.* **8** (2006) 391.

[175] L. C. Branco, C. A. M. Afonso, *J. Org. Chem.* **69** (2004) 4381.

[176] H. Xie, S. Zhang, H. Duan, *Tetrahedron Lett.* **45** (2004) 2013.

[177] S. Fang, L. Yang, J. Wang, H. Zhang, K. Tachibana, K. Kamijima, *J. Power Sources* **191** (2009) 619.

[178] S. Fang, L. Yang, C. Wie, C. Jiang, K. Tachibana, K. Kamijima, *Electrochim. Acta* **54** (2009) 1752.

[179] P. Wang, S. M. Zakeeruddin, M. Grätzel, W. Kantlehner, J. Mezger, E. V. Stoyanov, O. Scherr, *Appl. Phys. A* **79** (2004) 73.

[180] D. Li, M. Wang, J. Wu, Q. Zhang, Y. Luo, Z. Yu, Q. Meng, Z. Wu, *Langmuir* **25** (2009) 4808.

[181] S. Fang, L. Yang, J. Wang, M. Li, K. Tachibana, K. Kamijima, *Electrochim. Acta* **54** (2009) 4269.

[182] M. Kleinert, A. Cuesta, L. A. Kibler, D. M. Kolb, *Surf. Sci.* **430** (1999), L521.

[183] A. S. Dakkouri, *Solid State Ionics* **94** (1997) 99.

[184] C. Berger, Diplomarbeit, Universität Ulm (2011).

[185] C. Wöll, S. Chiang, R. J. Wilson, P. H. Lippel, *Phys. Rev. B* **39** (1989) 7988.

[186] Y. Hasegawa, P. Avouris, *Science* **258** (1992) 1763.

[187] V. Repain, J. M. Berroir, S. Rousset, J. Lecoeur, *Appl. Surf. Sci.* **162** (2000) 30.

[188] J. V. Barth, H. Brune, G. Ertl, R. J. Behm, *Phys. Rev. B* **42** (1990) 9307.

[189] D. D. Chambliss, R. J. Wilson, S. Chiang, *Phys. Rev. Lett.* **66** (1991) 1721.

[190] R. Atkin, N. Borisenko, M. Drüschler, S. Zein El Abedin, F. Endres, R. Hayes, B. Huber, B. Roling, *Phys. Chem. Chem. Phys.* **13** (2011) 6849.

[191] R. Gómez, A. Rodes, J. M. Pérez, J. M. Feliu, A. Aldaz, *Surf. Sci.* **327** (1995) 202.

[192] R. Gómez, A. Rodes, J. M. Pérez, J. M. Feliu, A. Aldaz, *Surf. Sci.* **344** (1995) 85.

[193] L. A. Kibler, M. Kleinert, A. Cuesta, D. M. Kolb in: *Elektrochemische Reaktionstechnik und Synthese*, GDCh-Monographie, Bd. 14, J. Russow, G. Sandstede, R. Staab (Ed.), Frankfurt am Main (1999) p. 48.

[194] L. A. Kibler, A. M. El-Aziz, R. Hoyer, D. M. Kolb, *Angew. Chem. Int. Ed.* **44** (2005) 2080.

[195] M. Baldauf, D. M. Kolb, *J. Phys. Chem.* **100** (1996) 11375.

[196] L. A. Kibler, M. Kleinert, V. Lazarescu, D. M. Kolb, *Surf. Sci.* **498** (2002) 175.

[197] I.-W. Sun, C. L. Hussey, *J. Electroanal. Chem.* **274** (1989) 325.

[198] H. C. De Long, J. S. Wilkes, R. T. Carlin, *J. Electrochem. Soc.* **141** (1994) 1000.

[199] S.-I Hsiu, C.-C. Tai, I-W. Sun, *Electrochim. Acta* **51** (2006) 2607.

[200] F. Endres, M. Bukowski, R. Hempelmann, H. Natter, *Angew. Chem.* **115** (2003) 3550.

[201] Y.-Z. Su, Y.-C. Fu, Y.-M. Wei, J.-W. Yan, B.-W. Mao, *Chem. Phys. Chem.* **11** (2010) 2764.

[202] M. H. Hölzle, Th. Wandlowski, D. M. Kolb, *J. Electroanal. Chem.* **394** (1995) 271.

[203] F. Endres, *Phys. Chem. Chem. Phys.* **3** (2001) 3165.

List of Abbreviations

$BMIPF_6$	1-butyl-3-methylimidazoliumhexafluorophosphate
$BMIBF_4$	1-butyl-3-methylimidazoliumtetrafluoroborate
$BMITf_2N$	1-butyl-3-methylimidazolium-bis(trifluoromethylsulfonyl)imide
$BuMePyTf_2N$	1-butyl-1-methylpyrrolidinium-bis(trifluoromethylsulfonyl)imide
$MePrPpTf_2N$	N-methyl-N-propylpiperidinium-bis(trifluoromethylsulfonyl)imide
$BuPyrBF_4$	N-butylpyridiniumtetrafluoroborate
$BuMe_3NTf_2N$	butyl-trimethylammonium-bis(trifluoromethylsulfonyl)imide
$Bu_2Et_2Me_2GuanTf_2N$	N,N-dibutyl-N',N'-diethyl-N",N"-dimethylguanidinium-bis(trifluoromethylsulfonyl)imide
OHP	outer Helmholtz plane
IHP	inner Helmholtz plane
pzc	potential of zero charge
pztc	potential of zero total charge
pzfc	potential of zero free charge
fcc	face centered cubic
hcp	hexagonal close-packed
UHV	ultra-high vacuum
SCE	saturated calomel electrode
PW	potential window
CV	cyclic voltammetry

WE	working electrode
RE	reference electrode
CE	counter electrode
OPA	operational amplifier
EIS	electrochemical impedance spectroscopy
CPE	constant phase element
STM	scanning tunneling microscopy
LDOS	local density of states
DC	direct current
AC	alternating current
OCP	open circuit potential
UPD	under potential deposition

List of Symbols

Q	charge
q	charge density
I	current
j	current density
C_{dl}	double layer capacitance
E	electrode potential
C_0	Gouy-Chapman capacitance [12]
γ	lattice-saturation parameter [12]
φ_m	potential of the metal
φ_{el}	potential of the electrolyte
ρ	density
c	molar concentration
η	viscosity
D	diffusion coefficient
σ	conductivity
ν	sweep rate
U	voltage
ω	angular frequency
f	frequency
φ	phase difference

Z	impedance
C	complex capacitance
Z_{real}	real part of impedance
Z_{imag}	imaginary part of impedance
Y	admittance
Q	CPE coefficient
n	CPE exponent
R_{ct}	charge transfer resistance
W	Warburg element
R_s	solution resistance
C_{ad}	adsorption resistance
C_{hf}	high frequency capacitance
σ_{ad}	diffusional Warburg coefficient
R_{ad}	adsorption resistance
L	inductance
I_t	tunneling current
U_t	tunneling voltage
Φ_t	tunneling barrier
Φ	work function
E_{vac}	vacuum level
E_F	Fermi level

Publication List

(1) M. Gnahm, T. Pajkossy, D. M. Kolb: „The interface between Au(111) and an ionic liquid“ *Electrochim. Acta* **55** (2010) 6212-6217.

(2) M. Gnahm, D. M. Kolb: „The purification of an ionic liquid“ *J. Electroanal. Chem.* **651** (2011) 250-252.

(3) M. Gnahm, C. Müller, R. Répánszki, T. Pajkossy, D. M. Kolb: „The interface between Au(100) and 1-butyl-3-methyl-imidazolium-hexafluorophosphate“ *Phys. Chem. Chem. Phys.* **13** (2011) 11627–11633.

(4) M. Gnahm, C. Berger, M. Arkhipova, H. Kunkel, T. Pajkossy, G. Maas, D. M. Kolb: „The interfaces of Au(111) and Au(100) in a hexaalkyl-substituted guanidinium ionic liquid: an electrochemical and *in-situ* STM study“ *submitted to Phys. Chem. Chem. Phys.*.

(5) M. Gnahm, M. Saitner, H.-G. Boyen, D. M. Kolb: „The initial stages of Pd deposition onto Au(111) and Au(100) from 1-butyl-3-methyl-imidazolium-hexafluoro- phosphate“ *in preparation.*

Acknowledgement

This thesis is based upon studies conducted during January 2008 to May 2011 at the Institute of Electrochemistry, University of Ulm. The primary emphasis of this dissertation is laid on properties and structure of the interface between ionic liquids and gold electrodes.

To complete a project like this requires a network of support, and I am indebted to many people:

Above all I am grateful to my supervisor Prof. Dr. Dieter M. Kolb who deceased on October 4, 2011, few weeks before completing this work. I would like to say thanks for the opportunity to work in his institute, for rich discussions and his encouragement throughout the years. I also would like to thank for the participation on various conferences like the International Bunsen Discussion Meeting 2008 in Clausthal, the Research Day of the Landesstiftung Baden-Württemberg 2009 in Stuttgart, the Symposium on Metal Deposition for Emerging Nanoelectronic Applications II at the castle Reisensburg 2009 as well as the GDCh-meeting Elektrochemistry 2010 at the Ruhr-Universität Bochum with the possibility of presenting my results.

I also wish to thank Prof. Dr. T. Jacob and Prof. Dr. Werner Tillmetz for having accepted to be the referees for this thesis.

Especially I want to thank Dr. Tamás Pajkossy from the Institute of Materials and Environmental Chemistry, Chemical Research Center, Hungarian Academy of Science, Budapest. His interest in the new field of ionic liquids, innumerable days together in the laboratory as well as the visits in Budapest made the collaboration a unique experience. I also thank him for reading and commenting the draft. Special thanks to Reka Répánszki and Soma Vesztergom for their experimental support. I also thank Prof. Dr. Gerhard Maas and Maria Arkhipova from the Institite of Organic Chemistry I, University of Ulm, for their synthetic work on guanidinium-based ionic liquids.

Many thanks to all my colleagues from the institute for their cooperativeness. Special thanks to Dr. Ludwig Kibler for many inspiring discussions and to Claus Müller and Claudia Berger for their experimental support. I also would like to thank Ute Thomas and Constanze Duvigneau for their help and Reinhard Liske for taking care of the technical

equipment.

My parents I would like to thank sincerely for their encouragement and (financial) support during the years.

Finally I would like to thank the Landesgraduiertenförderung for granting the research fellowship.

Curriculum Vitae

Persönliche Daten

Name	Markus Gnahm
Adresse	Eberhardtstraße 43, 89073 Ulm
Geburtsdatum	23.04.1981
Geburtsort	Ulm

Schulbildung

1987-1991	Heinrich-Kaim-Grundschule Schelklingen
1991-1992	Gymnasium Blaubeuren
1992-1998	Karl-Spohn-Realschule Gerhausen
07/1998	Mittlere Reife
1998-2001	Technisches Gymnasium der Robert-Bosch-Schule Ulm
06/2001	Abitur

Wehrdienst

07/2001-03/2002	Grundwehrdienst, 1./Gebirgsjägerbataillon 233, Mittenwald

Hochschulbildung

10/2002-08/2007	Studium der Chemie an der Universität Ulm
09/2004	Vordiplom Chemie
03/2007-08/2007	Diplomarbeit am Institut für Elektrochemie der Universität Ulm unter der Leitung von Prof. Dr. D. M. Kolb zum Thema „In-situ rastertunnelmikroskopische Untersuchungen zur elektrochemischen Abscheidung von Silber auf Platin(111)“.

08/2007	Diplom in Chemie
seit 09/2007	Promotion am Institut für Elektrochemie der Universität Ulm unter der Leitung von Prof. Dr. D. M. Kolb zum Thema „Properties and Structure of the Electrified Gold/Ionic Liquid Interface “.
12/2007-12/2010	Gewährung eines Promotionsstipendiums der Landesgraduiertenförderung

Wissenschaftlicher Werdegang

seit 06/2011	Wissenschaftlicher Mitarbeiter, Helmholtz-Institut Ulm (HIU)

Fremdsprachenkenntnisse

Englisch, Französisch, Italienisch, Spanisch

Ulm, den 12.11.2012

(Markus Gnahm)

Selbständigkeitserklärung:

Hiermit erkläre ich, die vorliegende Dissertation selbständig und ohne unerlaubte fremde Hilfe angefertigt zu haben. Ich habe keine anderen als die angegebenen Quellen und Hilfsmittel benutzt und sämtliche Textstellen, die wörtlich oder sinngemäß aus veröffentlichten oder unveröffentlichten Schriften entnommen wurden, und alle Angaben, die auf mündlichen Auskünften beruhen, als solche kenntlich gemacht. Ebenfalls sind alle von anderen Personen erbrachten Leistungen als solche gekennzeichnet.

Ulm, den 12.11.2012

(Markus Gnahm)